University of Bristol
Department of Aerospace Engineering

# Delamination in Composite Laminates with Curvature and Discontinuous Plies

Zackarias Petrossian

February 1998

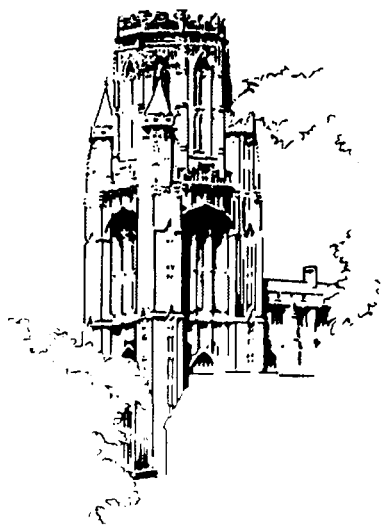

A thesis submitted to the University of Bristol in accordance with the requirements of the degree of Doctor of Philosophy in the Faculty of Engineering

# Abstract

A series of studies have been carried out to investigate delamination in composite laminates caused by interlaminar shear stresses due to out-of-plane forces, curvature induced through-thickness tensile stresses, and local interlaminar stress distributions at the ends of terminated plies. The aim was to develop methods for predicting this type of failure which were accurate and not overly complex.

Curved specimens, which had been designed and tested to measure the through-thickness strength of composites under combined tension and shear, were analysed with the aid of the finite element method. After Weibull theory had been used to take account of volumetric size effects, a simple interactive stress criterion predicted the failure loads of the specimens to within 11%.

A closed form solution was derived for predicting the strain energy release rate of delaminations spreading from a ply-drop in a laminate under combined bending and axial loading. From a parametric study, it was found that failure envelopes could be constructed based on the axial strain at the drop, irrespective of the type of loading.

A fracture mechanics based approach was developed which took account of yielding in the resin rich layer prior to crack formation. With the aid of finite element analysis, the failure loads of straight and curved specimens with discontinuous plies were predicted. There was very good correlation with experimental data for the straight specimens, and reasonable correlation for the curved specimens. Delamination growth in cyclic fatigue loading was also predicted in the straight specimens by using a modified Paris equation. The prediction was qualitatively very similar to observed test results.

Finally, a type of interface element was designed to model the yielding and failure of resin along ply interfaces. These elements were placed in the finite element models of the previous straight and curved specimens. There was good qualitative agreement with the test data in terms of the locations of the delaminations and the amount of stable crack growth before catastrophic failure, but the accuracy of the predicted failure loads depended on the post-yield behaviour assumed by the interface elements.

# Acknowledgements

Acknowledgements are due to the EPSRC and GKN Westland Helicopters for providing financial support for my PhD. I would also like to express my gratitude towards Professor Michael Wisnom for his helpful advice and fruitful discussions throughout my studies. Thanks are also due to Mr. Mike Jones for preparing and testing the specimens which I analysed.

I would like to dedicate this thesis to my loving father who sadly passed away during the final stages of my PhD.

# Author's Declaration

Guidance has been given by the author's academic advisor, and all the specimen manufacture and testing was carried out by an experimental officer at the University. Otherwise, the work contained in this thesis is wholly the author's own work, aside from where a reference or acknowledgement has been made to outside work.

Note that the views expressed in the dissertation are those of the author and not necessarily of the University.

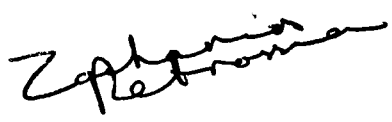

Zackarias Petrossian

# Contents

# Tables

# Figures

# Nomenclature

| | |
|---|---|
| a | crack length |
| $a_0$ | characteristic distance over which stress must be averaged for Whitney-Nuismer method |
| A | crack area |
| d | axial distance between contact point of loading roller and cut in laminates with discontinuous plies |
| $d_0$ | characteristic distance away from stress singularity for Whitney-Nuismer method |
| E | Young's modulus |
| $E_A$ | axial Young's modulus of block of plies above ply-drop |
| $E_B$ | axial Young's modulus of block of discontinuous plies |
| $E_C$ | axial Young's modulus of block of plies below ply-drop |
| g | empirical constant found from fatigue tests (see equation (7.1)) |
| G | strain energy release rate (apart from isolated cases where it has been defined as the shear modulus) |
| $G_c$ | critical strain energy release rate |
| $G_f$ | difference between strain energy release rate at peak and trough loads in fatigue test |
| $G_{norm}$ | $G_I / G_{Ic} + G_{II} / G_{IIc}$ |
| $G_T$ | total strain energy release rate |
| h | empirical constant found from fatigue tests (see equation (7.1)) |
| H | plastic modulus |
| j | ratio $E_B / E_A$ |
| k | ratio $E_C / E_A$ |
| m | Weibull modulus |
| M | bending moment per unit width |
| N | number of loading cycles in fatigue test |
| P | load per unit width |

| | |
|---|---|
| $P_f$ | probability of failure |
| $P_s$ | probability of survival |
| R | ratio of bending to axial loading, defined in (4.34) |
| $R_f$ | ratio of trough to peak load in fatigue test |
| s | deviatoric normal stress |
| S | shear strength |
| $\overline{S}$ | equivalent shear strength for Weibull analysis |
| t | thickness of laminate |
| $t_r$ | thickness of the resin rich layer |
| T | tangent modulus |
| U | strain energy |
| V | volume |
| w | width of laminate |
| W | work done by loading |
| $W_S$ | work required to create new crack surface |
| $Y_c$ | absolute value of through-width compressive strength |
| $Y_t$ | through-width tensile strength |
| $\overline{Z}$ | equivalent through-thickness failure stress for Weibull analysis |
| $Z_c$ | absolute value of through-thickness compressive strength |
| $Z_t$ | through-thickness tensile strength |

| | |
|---|---|
| $\alpha$ | ratio of thickness of dropped plies to thickness of whole laminate |
| $\beta$ | ratio of distance of dropped plies from bottom surface of laminate to thickness of whole laminate |
| $\varepsilon$ | normal strain |
| $\varepsilon_d$ | axial strain at mid-thickness of block of dropped plies |
| $\gamma$ | shear strain |
| $\gamma^u$ | ultimate shear strain |
| $\nu$ | Poisson's ratio |
| $\Pi$ | potential energy of system |

| | |
|---|---|
| $\sigma$ | normal stress |
| $\bar{\sigma}$ | equivalent constant normal stress which gives same probability of failure as actual variable normal stress distribution |
| $\sigma_0$ | characteristic strength in Weibull function |
| $\sigma_{VM}$ | equivalent von Mises stress (defined in (8.8) for plane stress) |
| $\sigma_Y^c$ | absolute value of yield stress in compression |
| $\sigma_Y^t$ | yield stress in tension |
| $\tau$ | shear stress |
| $\bar{\tau}$ | equivalent constant shear stress which gives same probability of failure as actual variable shear stress distribution |
| $\tau_{VM}$ | equivalent von Mises stress divided by $\sqrt{3}$ |
| $\tau_Y$ | shear yield stress |

Unless otherwise mentioned, subscripts 1, 2 and 3 refer to the fibre direction, the direction transverse to the fibres in the plane of the ply, and the through-thickness direction, respectively. Subscript x refers to the axial direction of the laminate from which the ply orientations are measured, and y and z are the in-plane and out-of-plane transverse directions, respectively. Subscripts I, II and III refer to the principal values when used with stress, and the mode I, mode II and mode III values when used with strain energy release rate.

The superscripts e and p refer to elastic and plastic, respectively.

# Chapter 1

# Introduction

## 1.1 Composite materials

Composite materials consist of two or more distinct compounds. One of the earliest man-made composites consisted of mud and straw. When primitive man started building houses, he learnt that mud bricks could be made stronger by reinforcing them with straw. These days, concrete reinforced with steel bars is the preferred building material. In the aerospace industry, the reinforcement usually consists of fibres of glass, carbon or aramid, and the binding material or matrix is usually some form of plastic, although metals, ceramics and even carbon can also be used. These composites are not only used in the aerospace industry but also in the marine, sports and automotive industries. Their main advantage over metal is their high specific strength and stiffness. Gram for gram the above mentioned fibres are both stiffer and stronger than steel wire.

The matrix material is generally not very stiff or strong but is nonetheless vital. Apart from holding the fibres in place, the matrix protects them from the outside environment, inhibits the fibres from buckling, and supports most of the shear and tensile loads transverse to the fibres. One of the most popular types of matrix material is epoxy resin. These are thermoset polymers which have good mechanical properties, chemical resistance and adhesion to fibres.

Since aerospace structures are usually made of sheet material and have to support major loads along one direction, the epoxy and fibres are often partially cured together in the form of thin sheets with all the fibres aligned in one direction. Each of these unidirectional "prepreg" sheets or plies is only about one eighth of a millimetre thick. Therefore, several plies or "laminae" are bonded together to form a "laminate" by curing them under pressure at between 120 and 180°C in autoclaves. Each ply is very stiff and strong in the fibre direction but relatively weak in the transverse directions. Thus, if the structure must withstand loads in more than one direction, the plies are laid up in different orientations so that the resulting laminate has the required strengths and stiffnesses in the specified directions.

## 1.2 Delamination

As mentioned above, composites are strong in the fibre direction but weak in the transverse directions. This means composite laminates can withstand large in-plane loads but easily fail when loads are applied in the thickness direction. One of the most common types of through-thickness failure is delamination. This is when cracks grow in-between adjacent plies and cause them to come apart or debond. Through-thickness tensile and interlaminar shear stresses high enough to cause delamination can arise in many different situations. Some of them can be seen schematically in figure 1.1.

In the aerospace industry it is very desirable for structural damage to be visible to the naked eye. If a foreign object, such as a bird or large hail stone, hits the surface of a metal wing hard enough, it will leave a visible dent. However, if the surface is made of composite material, it is possible for delamination to occur inside the laminate with no visible surface damage, as seen in figure 1.1a. The delamination can subsequently grow when in-plane loads are applied to the laminate.

If a ply is loaded in the fibre direction so that it extends axially, it will contract in the transverse direction due to the Poisson effect. If instead the ply is loaded in transverse

tension, it will contract in the fibre direction. However, the contraction in the latter case will be relatively less than that in the former case because the Poisson's ratios are different in the two directions. This can result in high interlaminar tension and shear arising at the free edges of multidirectional laminates, which leads to delamination, as seen in figure 1.1b. Acute interlaminar shear stresses can also arise at the free edges of laminates consisting entirely of plies oriented at angles $+\theta$ and $-\theta$ [1].

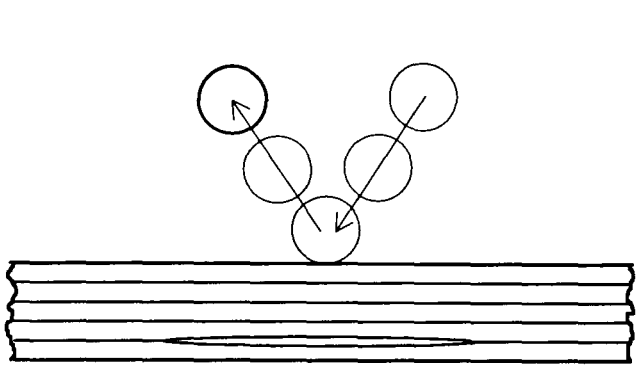

a). Foreign object impact

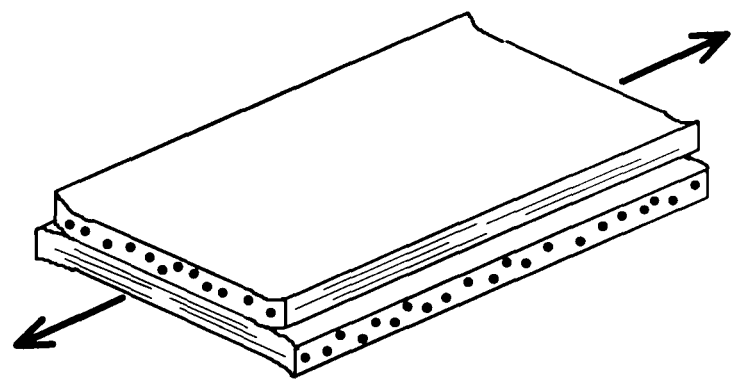

b). Free edges of multidirectional laminate

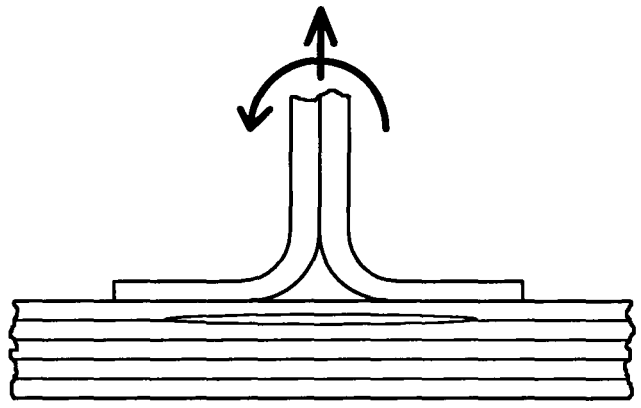

c). Spar bonded to composite skin

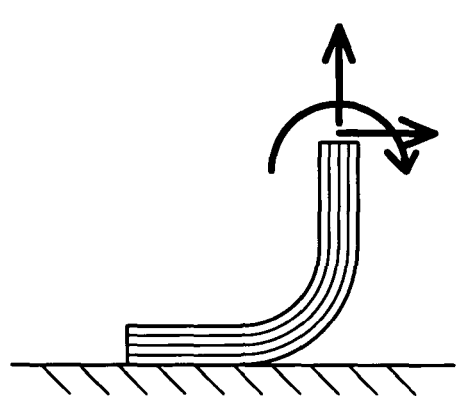

d). Curved laminates

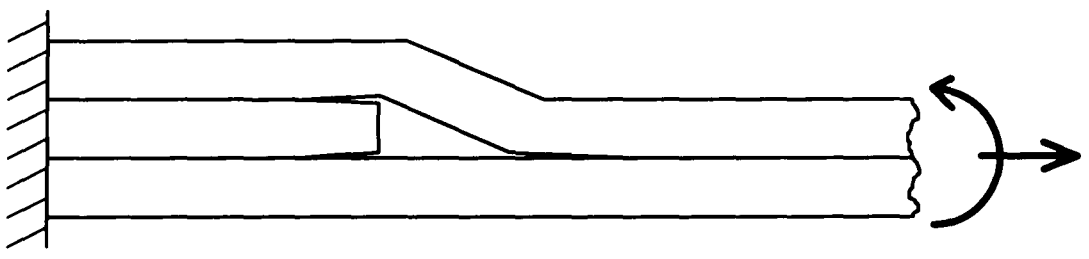

e). Discontinuous Plies

**FIG. 1.1** Situations leading to delamination

Figure 1.1c shows a spar bonded to a composite skin. Forces and bending moments applied to the spar can cause through-thickness tensile stresses in the skin high enough to result in delamination. Through-thickness tensile stresses can also arise in curved laminates subject to in-plane forces and out-of-plane bending moments, as seen in figure 1.1d. Out-of-plane forces can cause through-thickness tension in curved laminates and also interlaminar shear stresses in laminates with or without curvature.

Our final example is a laminate with a discontinuous ply, seen in figure 1.1e. Plies are often discontinued or dropped off within laminates to reduce the thickness. Laminates need to be tapered in the thickness dimension when the requirement for strength and stiffness changes along the length of the structure. For example, tapered laminates are found in helicopter rotor blades where the thickness around the joint at the hub needs to be higher than that along the aerodynamic portion of the blade. In spars of aircraft wings and tailplanes there are higher bending moments at the root than at the tip. This means a composite spar would require more plies at the root.

When such laminates undergo out-of-plane bending or in-plane loading, the axial loads taken by the discontinuous plies have to be transferred to the surrounding continuous plies. This means high interlaminar shear stresses arise near the ply drop between the continuous and discontinuous plies. If the taper angle is too sharp, significant through-thickness stresses can also occur between the continuous plies that meet ahead of the ply drop. Thus delamination can initiate at the ply drop and spread into both the thick section and the thin section.

Note that it is quite possible for laminates to be both curved and tapered, such as at the edges of some sandwich panels and parts of composite rotor blades, thus giving rise to two or more stress distributions which can interact to cause delamination.

## 1.3 Research objective

Delaminations can greatly reduce the strength and stiffness of a laminate, which in turn can lead to catastrophic failure of the whole structure. Aerospace structures are rigorously tested prior to service to make sure they will remain integral throughout their service lives. If degradation such as delamination occurs and is seen to be a danger to the integrity of the structure, the component must be re-designed and re-tested. This is a costly and timely process. It is therefore very desirable to be able to accurately predict the loading conditions at which delamination initiates and propagates so that the amount of expensive testing can be reduced.

GKN Westland Helicopters is an aerospace company which uses composite materials in its aircraft. They see the need for accurate delamination prediction methods. This thesis describes part of an on-going project at the University of Bristol, sponsored by GKN Westland Helicopters, to study through-thickness failure in composites, primarily in curved laminates with dropped plies. Some of the work described within has already been published in the form of technical papers and can be seen in [2-7]. The aim of the research was to develop prediction methods which are both accurate and relatively simple to use in terms of computing power and time.

The strategy was to study relatively simple situations and then to gradually increase the complexity, forming methods for predicting delamination in each case. These are described below.

1. Curved laminates under out-of-plane forces and bending moments but without any ply discontinuities. An approach was developed based on using Weibull theory with a simple quadratic stress criterion. It takes account of the dependence of through-thickness strength on the volume of stressed material.

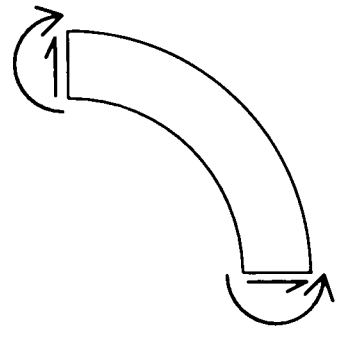

2. Laminates with discontinuous plies in bending and in-plane loading but no curvature or out-of-plane forces. In this case, it was possible to derive a closed form solution for the strain energy release rate of delamination from the ply-drop. It can be used as a simple initial design tool. A parametric study was also carried out to look at the effect of the size and location of the ply-drop, lay-up of the laminate, and the loading conditions.

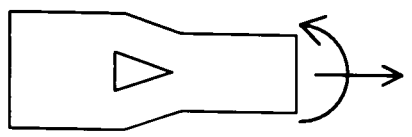

3. Straight laminates with discontinuous plies under both in-plane and out-of-plane loading. A numerical mixed-mode strain energy release rate approach was developed which takes account of matrix yielding prior to crack propagation. An additional study was also carried out to predict delamination under cyclic loading. A Paris type equation was used to relate the rate of crack propagation with the cyclic strain energy release rate.

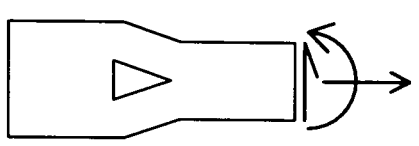

4. Curved laminates with discontinuous plies under any loading. The approach in (3) was used but since there was more opening mode delamination in the curved laminates, the mixed-mode strain energy release rate criterion was more fully verified. The use of an interactive yield criterion to predict the size of the yield zone prior to delamination was also required.

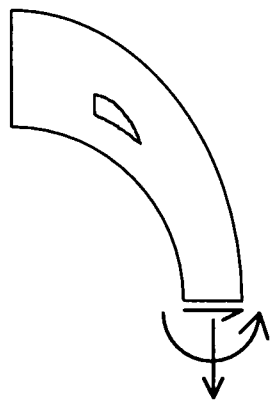

5. Both straight and curved laminates under any loading, for cases with several delamination sites. A finite element was designed which models the interface between plies. The initiation and propagation of delamination at any number of sites can be predicted when the interface element is inserted into a finite element model of the laminate. However, the approach is more computer intensive than the previous methods.

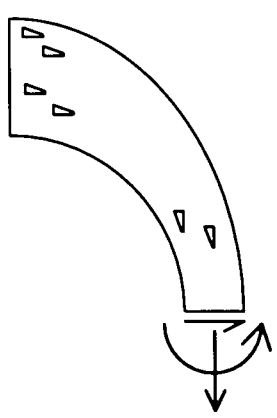

In each case, specimens were designed and tested to isolate the individual problems. Analysis was then carried out and verified with the experimental results. All of the specimens were loaded statically, although one type was also loaded cyclically to look at the issue of fatigue. The material chosen for specimen manufacture was 913 epoxy reinforced with E glass fibres. This composite is used for rotor blade construction but more importantly in terms of the research, it is relatively inexpensive and since it is translucent delaminations can be detected visually. To separate the problem of free edge delamination from delamination induced by curvature and dropped plies, unidirectional specimens were tested. This enabled us to study the latter two issues in isolation. The interaction between all three cases could then be investigated more easily in future research.

# Chapter 2

# Established Methods for Predicting Delamination

Delamination is usually predicted using either stress based failure criteria or strain energy release rate based criteria. An introduction to both these concepts will therefore be given, along with references to some of the relevant literature in each case. Note that the above two concepts are not the only ones to have been used for predicting delamination in composite laminates. There are other less popular or less well established approaches such as using stress intensity factors [8], J-integrals [9], Weibull theory or interface elements with the finite element method. The latter two will be discussed in subsequent chapters.

## 2.1 Methods based on stress

Many stress based criteria exist for predicting in-plane failure in composites. However, we are concerned with delamination here, so only out-of-plane failure criteria will be discussed. Since delamination is a matrix dependent failure mode, stress-based prediction methods should be based on the stresses in the matrix. These are related to the interlaminar shear and through-thickness normal stresses in the laminate, although there is evidence of delamination depending somewhat on the fibre direction stress [10]. Composites are not isotropic materials and geometric

attributes such as ply-drops complicate the interlaminar stress state. Therefore, the finite element method is often used to obtain the interlaminar stresses, which are then substituted into an inequality along with material strength values. Failure is predicted if, anywhere in the structure, the left hand side of the inequality is greater or equal to the right hand side.

### 2.1.1 Maximum stress criteria

This is the simplest form of failure criterion. It works well when there is one predominant stress component. According to these criteria, through-thickness failure will occur when one of the interlaminar stress components reaches or exceeds the corresponding material strength, as indicated below:

$$|\sigma_3| \geq Z_t \qquad \text{when } \sigma_3 > 0 \qquad (2.1)$$

$$|\sigma_3| \geq Z_c \qquad \text{when } \sigma_3 < 0 \qquad (2.2)$$

$$|\tau_{13}| \geq S_{13} \qquad (2.3)$$

$$|\tau_{23}| \geq S_{23} \qquad (2.4)$$

where $\sigma$ and $\tau$ are normal and shear stresses, subscript 1 refers to the fibre direction, and subscripts 2 and 3 refer to the in-plane and out-of-plane directions transverse to the fibres, respectively. Finally, S refers to the shear strength and $Z_t$ and $Z_c$ are absolute values of the through-thickness tensile and compressive strengths, respectively.

For convenience transverse isotropy is often assumed, i.e. $S_{13} = S_{12}$, $Z_t = Y_t$ and $Z_c = Y_c$ (where Y is the transverse in-plane strength), so that data from in-plane tests can be used. However, the in-plane and out-of-plane strengths are generally slightly different, so it is recommendable to use through-thickness test data wherever possible. There are many types of tests for evaluating the interlaminar strengths of

composite laminates and each has its own advantage and disadvantage. Some of the most popular are the short beam shear test, V-notched beam in shear, short block in tension and waisted block in compression. These and other test methods are described and assessed in [11].

### 2.1.2 Interactive stress criteria

When there is more than one significant stress component at the same point in the structure, it is necessary to take account of the interaction between them. There are numerous interactive stress criteria which have been used for predicting delamination in composites.

The von Mises yield criterion, which was designed for use with metals, has been used to predict failure in the resin rich layers between plies [12]. Yielding or failure occurs when the following inequality is satisfied:

$$(\sigma_I - \sigma_{II})^2 + (\sigma_{II} - \sigma_{III})^2 + (\sigma_{III} - \sigma_I)^2 \geq 2\sigma_Y^2 \qquad (2.5)$$

where $\sigma_I$, $\sigma_{II}$ and $\sigma_{III}$ are the three principal stresses in the matrix, and $\sigma_Y$ is the yield stress in simple tension.

The matrix is usually some form of polymer; and since polymers generally have different compressive and tensile yield stresses and the hydrostatic stress influences yielding, the von Mises criterion is not suitable for predicting matrix failure. Raghava proposed a yield criterion which was found to work well with both glassy amorphous polymers [13] and crystalline polymers [14]. Yielding occurs when,

$$(\sigma_I - \sigma_{II})^2 + (\sigma_{II} - \sigma_{III})^2 + (\sigma_{III} - \sigma_I)^2 + 2(\sigma_I + \sigma_{II} + \sigma_{III})(\sigma_Y^c - \sigma_Y^t) \geq 2\sigma_Y^t.\sigma_Y^c \qquad (2.6)$$

where $\sigma_Y^t$ and $\sigma_Y^c$ are the absolute values of the yield stresses in tension and compression, respectively.

The main problem in applying the above two criteria is that the stresses in the matrix have to be found. This means one cannot assume the composite to be a homogeneous material, which is often done to simplify the finite element analysis.

Hashin [15] proposed a matrix failure criterion based on the matrix stresses which can be obtained directly from the "homogeneous composite" stresses. In other words, the fibre direction stress, which is different in the fibres and the matrix, does not appear in the criterion. This is largely carried by the fibres, anyway. The criterion is further simplified by assuming transverse isotropy. The difference between the compressive and tensile strengths is taken into account as follows:

$$\frac{(\sigma_2+\sigma_3)^2}{Y_t^2}+\frac{(\tau_{23}^2-\sigma_2\sigma_3)}{S_{23}^2}+\frac{(\tau_{12}^2+\tau_{13}^2)}{S_{12}^2}\geq 1$$

when $(\sigma_2 + \sigma_3) > 0$ (2.7a)

$$\frac{\left[(Y_c/2S_{23})^2-1\right](\sigma_2+\sigma_3)}{Y_c}+\frac{(\sigma_2+\sigma_3)^2}{4S_{23}^2}+\frac{(\tau_{23}^2-\sigma_2\sigma_3)}{S_{23}^2}+\frac{(\tau_{12}^2+\tau_{13}^2)}{S_{12}^2}\geq 1$$

when $(\sigma_2 + \sigma_3) < 0$ (2.7b)

The first two terms in (2.7b) model the much larger failure stress under hydrostatic pressure compared to uniaxial compression. The tensile component of (2.7) was reduced to plane-stress and used to model test data of unidirectional specimens in off-axis tension. Reasonable agreement was observed with boron / epoxy, whilst there was very good agreement with glass / epoxy specimens. If we consider just the interlaminar stresses (i.e., $\sigma_2 = 0$ and $\tau_{12} = 0$), and use the corresponding interlaminar strengths, $Z_t$ and $Z_c$, instead of $Y_t$ and $Y_c$, equations (2.7) reduce to,

$$\left(\frac{\sigma_3}{Z_t}\right)^2+\left(\frac{\tau_{23}}{S_{23}}\right)^2+\left(\frac{\tau_{13}}{S_{13}}\right)^2\geq 1 \qquad (2.8a)$$

for through-thickness tension and,

$$\left[\left(\frac{Z_c}{2S_{23}}\right)^2 - 1\right]\left(\frac{\sigma_3}{Z_c}\right) + \left(\frac{\sigma_3}{2S_{23}}\right)^2 + \left(\frac{\tau_{23}}{S_{23}}\right)^2 + \left(\frac{\tau_{13}}{S_{13}}\right)^2 \geq 1 \qquad (2.8b)$$

for through-thickness compression. Equations (2.7) predict matrix failure in general, whereas equations (2.8) specifically predict through-thickness or delamination failure.

Shokrieh and Lessard [16] proposed a delamination criterion similar to (2.8) which took account of non-linear shear stress - strain behaviour:

$$\left(\frac{\sigma_3}{Z}\right)^2 + \frac{\int_0^{\gamma_{13}} \tau_{13} d\gamma_{13}}{\int_0^{\gamma_{13}^u} \tau_{13} d\gamma_{13}} + \left(\frac{\tau_{23}}{S_{23}}\right)^2 \geq 1 \qquad (2.9)$$

where $\gamma$ is the shear strain, $\gamma^u$ is the ultimate shear strain, and $Z = Z_t$ in tension and $Z = Z_c$ in compression. Knowledge of the shear stress - strain response of the material is required for this criterion, and a non-linear stress analysis would have to be done, which makes it rather cumbersome. Nevertheless, they found it was important for carbon / epoxy laminates.

Altus and Dorogoy [17] proposed a single delamination failure criterion for both through-thickness compression and tension. They accounted for the much lower relative tensile strength as follows:

$$\frac{\sigma_3}{2Z_t} + \sqrt{\left(\frac{\sigma_3}{2Z_t}\right)^2 + \left(\frac{\tau}{S}\right)^2} \geq 1 \qquad (2.10)$$

where in this case $\tau^2 = (\tau_{13}^2 + \tau_{23}^2)$ and $S = S_{13} = S_{23}$. Notice that under pure through-thickness compression delamination will not occur, which infers an infinite compressive strength. It is true that the through-thickness compressive strength of composites is much higher than the tensile strength, but it is certainly not infinite.

Thus, it would not be reasonable to use this criterion in situations with significant through-thickness compression.

Finally, Fish and Lee [18] modified the Tsai-Wu criterion [19] by uncoupling the out-of-plane stresses from the in-plane stresses, and assuming $S = S_{13} = S_{23}$ as in the previous criterion. Their criterion states that delamination will occur when,

$$\frac{(Z_c - Z_t)}{Z_c Z_t}\sigma_3 + \frac{\sigma_3^2}{Z_c Z_t} + \frac{(\tau_{23}^2 + \tau_{13}^2)}{S^2} \geq 1 \qquad (2.11)$$

### 2.1.3 Whitney-Nuismer methods

From an analysis assuming linear-elastic material properties, the stresses at geometric discontinuities such as ply-drops and free edges of multidirectional laminates can often be infinite, even when the structure is burdened well below its failure load. Therefore, it is pointless to predict failure based upon the stress state at these stress singularities.

Whitney and Nuismer [20] proposed two approaches to overcome this problem. In the first approach, failure occurs when the stress at some distance, $d_0$, away from the discontinuity equals or exceeds the strength of the material. The physical meaning of $d_0$, given by the authors, is the distance over which the material must be critically stressed in order for there to be a sufficiently large flaw to initiate failure. The second approach is similar. Failure is predicted when the average stress over some distance, $a_0$, away from the discontinuity reaches or exceeds the strength of the material, i.e.,

$$\frac{1}{a_0}\int_0^{a_0} \sigma dx \geq \sigma_F \qquad (2.12)$$

where $\sigma_F$ is the strength of the material and x is the distance from the discontinuity. Both $a_0$ and $d_0$ were assumed to be material properties independent of laminate geometry and stress distribution. However, we shall soon see that many researchers

have found the contrary. Any of the previous stress based failure criteria may be used in conjunction with the Whitney-Nuismer approaches.

One advantage of these approaches is that they predict a reduction in strength of the laminate with an increase in size of the geometric discontinuity. This type of size effect is quite important in composites.

## 2.2 Strain energy release rate approach

### 2.2.1 Introduction

In 1920 Griffith [21] published an article which outlined a failure criterion based on energy rather than stress. He postulated the following.

1. According to the theorem of minimum potential energy, for a system to be in a state of equilibrium, the total potential energy must be at a minimum.
2. Consider a system consisting of an elastic body with a crack under loading. If the crack propagates so that the crack area increases by dA, the system will be in a state of nonequilibrium for an instant after the crack has grown. The system will then revert back to a state of equilibrium after the loads have redistributed and hence the potential energy of the system, $\Pi$, will reduce.
3. For new crack surface to be created, energy is required to break the bonds between the molecules on either side of the crack.
4. The energy required to create the new crack surface, $W_S$, is taken from the strain energy of the surrounding material and is equal to the net reduction of the potential energy of the system.

In other words,

$$\frac{dW_S}{dA} = -\frac{d\Pi}{dA} \tag{2.13}$$

Later, Irwin [22] referred to the right hand term in (2.13) as the "energy release rate", G. Also known as the strain energy release rate or the crack extension force, G is a measure of the energy available in the system for a crack to grow. It is found by calculating the loss in potential energy per unit increase in crack area for a hypothetical crack propagation. Real crack propagation will occur when G is equal to or higher than the critical value, $G_c$, which is assumed to be a material property and is equal to the left hand term in (2.13). The potential energy of the system is,

$$\Pi = U - W \tag{2.14}$$

where U is the strain energy stored in the body and W is the work done by the loading. Thus,

$$G = \frac{d(W - U)}{dA} \tag{2.15}$$

From this we can deduce that if we double the scale of a structure, including any defects or geometric discontinuities such as delaminations or ply-drops, the strain energy release rate will also double for a constant applied stress. Hence, similarly to the Whitney-Nuismer stress based methods, a reduction in strength with an increase in defect size is predicted with the strain energy release rate approach. However, in this case there is a more sound theoretical foundation.

For some situations it is possible to derive a closed form solution for the strain energy release rate (see chapter 4), but often it is evaluated using the finite element method.

### 2.2.2 Calculating G using the finite element method

The first step in applying the strain energy release rate approach is to identify where the crack is likely to grow. Thus, it is usually necessary to study the stress distributions in the structure beforehand. In composite laminates the crack path

frequently follows the resin rich layer between plies. A finite element model is then created with pairs of coincident nodes along the likely crack paths. The nodes belong to the elements on either side of the virtual crack and are initially held together using, for example, very stiff spring elements. Step by step, the nodes are then released to simulate crack propagation. At each increment of crack length the strain energy in the model is recorded, along with the displacements of the nodes at the applied loads. It is then possible to calculate the strain energy release rate as a function of the crack length using (2.15). Assuming linear-elasticity, once the G against crack length curve has been found, the strain energy release rate at any load can be obtained since it is proportional to the square of the load.

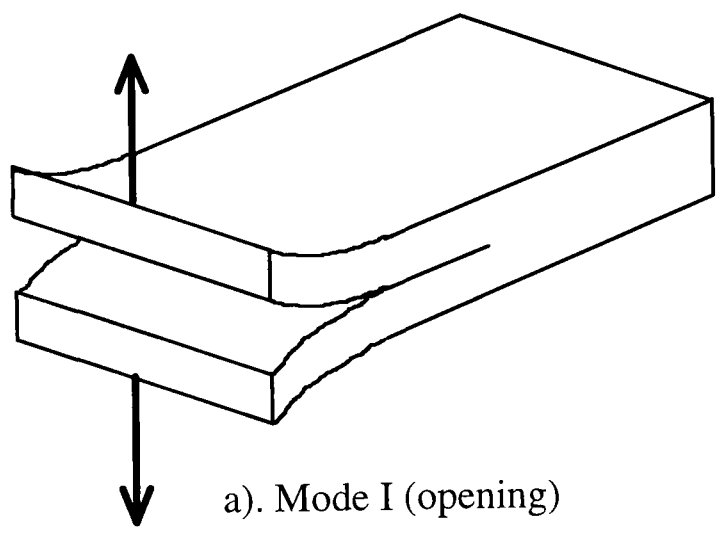

a). Mode I (opening)

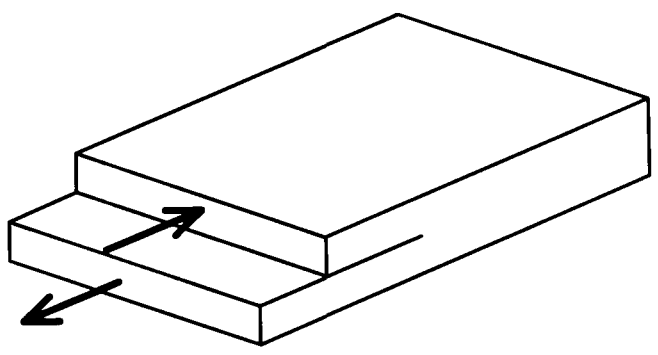

b). Mode II (shearing)

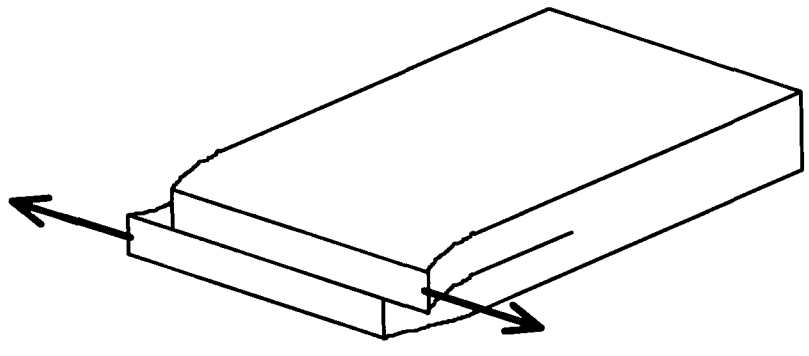

c). Mode III (tearing)

**FIG. 2.1** The three modes of crack formation

Crack propagation can be separated into three modes, as seen in figure 2.1. To calculate the individual components of G corresponding to each mode, i.e., $G_I$, $G_{II}$, and $G_{III}$, there has to be more than one spring at each node. If there is a combination of mode I and mode II crack propagation, one of the springs should act in the direction normal to the crack plane, and the other should act parallel to the crack plane. The springs are then released one by one and the energy change is recorded for each release. The energy change caused by releasing the normal spring gives the value of $G_I$, and the energy change due to releasing the parallel spring gives the value of $G_{II}$ [23].

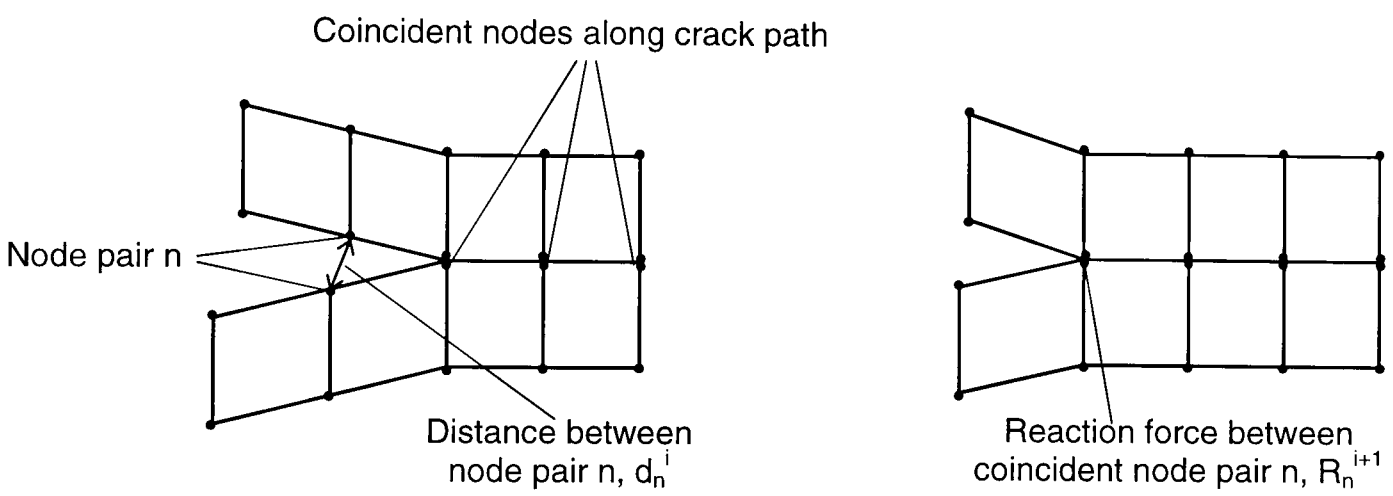


**FIG. 2.2** Virtual crack closure technique applied to finite element method

An alternative method for calculating the strain energy release rate is the virtual crack closure technique. This is based on Irwin's notion that the energy released due to an infinitesimal crack extension is equal to the work required to close the crack to its original length [24]. Hence, the strain energy release rate can be derived from the relative displacements of the node pair just ahead of the crack tip and the reaction forces between them just after they have been bound together. So for a linear-elastic material and small deformations,

$$G = \tfrac{1}{2}.d_n^i.R_n^{i+1} \qquad (2.16)$$

where d is the relative displacement between the pair of nodes, R is the component of the reaction force between them parallel to the relative displacement, and n refers to the node pair just ahead of the crack tip in step i of the finite element analysis, as seen in figure 2.2. Note that one may just as easily start with the coincident nodes held together and calculate G from R in the first step and d in the next step, after the nodes have been released.

If there are many steps in the analysis, one can obtain a curve of G against crack length as in the previous energy method. It is also possible to obtain each mode of G separately by resolving d into components parallel and perpendicular to the crack plane and multiplying each by the corresponding components of the reaction force.

Since the work done in closing the crack is calculated directly from the finite element nodal forces and displacements, the strain energy release rate will be less sensitive to mesh density than the stresses, which are based on the derivatives of the nodal displacements. Furthermore, by refining the mesh it is possible to reach a converged solution for G even when there are stress singularities. This is one of the main reasons the strain energy release rate approach is favoured over stress based criteria for situations where there are stress singularities.

### 2.2.3 Evaluation of the critical strain energy release rate

The pure mode I critical strain energy release rate, $G_{Ic}$, can be obtained from the double cantilever beam or DCB test. This is basically a beam with an already existing delamination at one end, loaded in through-thickness tension, as seen in figure 2.3. There are several pure mode II tests for obtaining $G_{IIc}$. The most widely used [11] is the end notched flexure or ENF test, seen in figure 2.4. This is similar to the DCB test except the specimen is loaded in three point bending. There are very few satisfactory pure mode III tests. Robinson and Song [25] describe a modified split cantilever beam or SCB test which can provide an accurate value of the pure mode III critical strain energy release rate, $G_{IIIc}$.

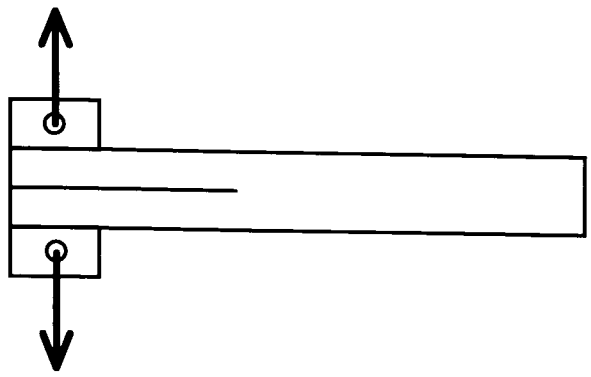

**FIG. 2.3** DCB test for $G_{Ic}$

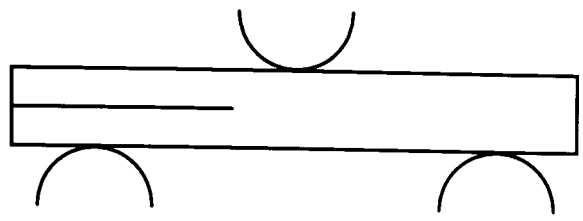

**FIG. 2.4** ENF test for $G_{IIc}$

The critical strain energy release rate for mixed-mode delamination, for a range of mode I to mode II loading ratios, can be found using the modified NASA mixed-mode bending or MMB test, described by Reeder [26]. Various data reduction methods for obtaining the critical strain energy release rates from DCB, ENF and MMB tests are discussed in [26-30].

### 2.2.4 Strain energy release rate failure criteria

When fracture is dominated by one mode or when the critical strain energy release rate is not dependent on mode of fracture, it is reasonable to predict crack growth by the simple criterion below.

$$G \geq G_c \tag{2.17}$$

where $G_c$ is the value corresponding to the dominant mode. Since composites are not homogeneous and are very anisotropic, the value of $G_c$ is generally quite different for different modes of fracture. This has resulted in the proposal of many interactive failure criteria for mixed-mode delamination.

Analysis of mode III delamination is not encountered often in the literature and most failure criteria are only functions $G_I$ and $G_{II}$. Failure envelopes can be constructed by plotting the strain energy release rate at failure on a graph with $G_I$ on one axis and $G_{II}$ on the other. A pure mode I value, a pure mode II value, and several mixed-mode

data points are required. Many mathematical models have been proposed to curve fit these failure envelopes. Reviews of strain energy release rate failure criteria have been made by Garg [31] and Reeder [26]. Garg reported frequent use of the following criterion in the literature:

$$\left(\frac{G_I}{G_{Ic}}\right)^m + \left(\frac{G_{II}}{G_{IIc}}\right)^n \geq 1 \qquad (2.18)$$

where m and n are empirically determined constants, and mentioned several researchers had found n = m = 1 for mixed-mode delamination in composites. Reeder [26] and Rhee [32] both found n = m = 1 worked well for carbon / PEEK composites. Mixed-mode data given by Kinloch et al [33] for carbon / epoxy also shows very close correlation with n = m = 1. However, Reeder did not find (2.18) satisfactory in modelling mixed mode data for carbon / epoxy composites, even when n and m were obtained by curve-fitting the data. Tests conducted by Hwu et al [34] showed m = 1.25 and n = 1.5 for glass / epoxy. Bradley [35] found that the values of n and m varied considerably between eight different composite materials and were not close to 1. Thus, there seem to be very conflicting views on this criterion and different composite systems have very different failure loci.

Another, more complicated, failure criterion was proposed by Hashemi et al [36] which can model the increasing $G_I$ with mode II loading sometimes observed for certain material systems. In this case, crack propagation is predicted when,

$$\left(\frac{G_I}{G_{Ic}} - 1\right)\left(\frac{G_{II}}{G_{IIc}} - 1\right) - \left[a + b\left(\frac{G_I}{G_I + G_{II}}\right)\right]\left(\frac{G_I}{G_{Ic}}\right)\left(\frac{G_{II}}{G_{IIc}}\right) \geq 0 \qquad (2.19)$$

where a and b are empirical constants found from mixed-mode tests. Reeder [26] found the above criterion matched his mixed-mode data for carbon / epoxy very well. However, he also found just as good correlation with a much simpler bilinear criterion. The increasing $G_I$ with mode II loading and the sudden "kink" in his carbon / epoxy failure envelopes could be characterised by,

$$G_I = \xi.G_{II} + G_{Ic} \tag{2.20a}$$

$$G_I = \zeta.G_{II} - \zeta.G_{IIc} \tag{2.20b}$$

where $\xi$ and $\zeta$ are the slopes of the two line segments in the failure envelope, as seen in figure 2.5. He explained the kink in the failure locus was due to a change in the failure mechanism somewhere between pure mode I and pure mode II loading.

More failure criteria can be found in [26] and [31]. At this point it is sufficient to say that as yet there is no unanimous agreement as to what failure criteria to use for a particular material system. A conservative and simple approach would be to use (2.18) with m = n = 1.

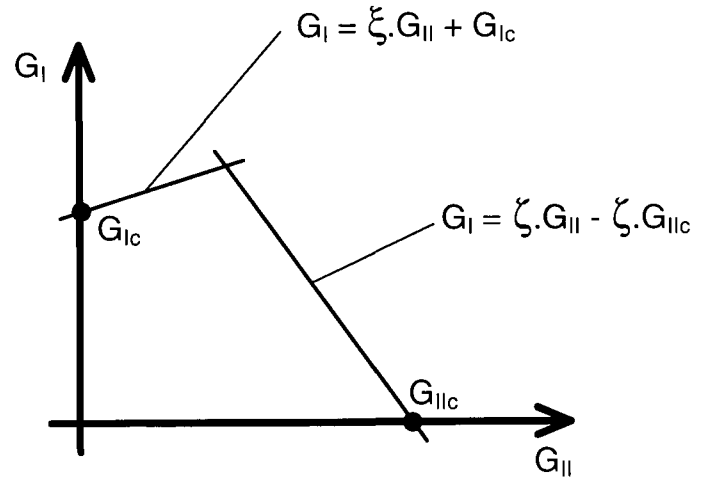


**FIG. 2.5** Schematic diagram of bilinear failure criterion [26]

## 2.3 Applications to real structures

The following is an account of the use of stress based and strain energy release rate based approaches for predicting delamination in composite structures, which was found in the literature. By comparing the predictions to the experimental results in each case, it will be possible to see the strengths and weaknesses of the different approaches. It will also be possible to see areas where there is a need for further research.

### 2.3.1 Stress based methods

Sen and Fish [37] subjected flat composite laminates to torsion loading to induce delamination failure due to interlaminar shear. Using the simple maximum interlaminar shear criterion they were able to predict the failure loads to within 5% for nine laminates with different lay-ups.

Vizzini and Lee [12] used the finite element method to analyse several different laminates with internal ply drops. They modelled the resin pocket at the end of the ply-drops and the resin rich layers between plies separately from the composite material. Hence, they were able to predict delamination failure using the von Mises criterion. However, since the stresses in the resin rich layers varied significantly with their assumed thickness, only a qualitative comparison with the experimental results could be made. When they assumed the resin pocket at the ends of the discontinued plies was initially cracked, the predicted locations of failure initiation and crack propagation matched the test results.

Altus and Dorogoy [17] also made qualitative predictions of delamination, in this case in a flat laminated plate with a circular hole subjected to in-plane loading. When the maximum through-thickness tensile stress criterion was used, the position of delamination initiation matched the experimental results, but the shapes of the delaminated regions didn't compare well. Better results were obtained using the maximum three-dimensional principal stress criterion. The criterion they proposed, (2.10), was not very successful.

On the other hand, Whitney and Nuismer [20] found both their failure criteria worked well in predicting the in-plane failure loads of quasi-isotropic glass / epoxy laminates with circular holes and $(0° / \pm 45°)_s$ carbon / epoxy laminates with initial in-plane cracks. Unfortunately, the failure mode was not mentioned. The predicted reduction in strength with increasing hole diameter and crack length matched their experimental results, and they used the same values of $a_0 = 3.8$mm and $d_0 = 1$mm for all their predictions. Thus, they assumed the characteristic distances to be independent of the type of geometric discontinuity, lay-up and material.

Nuismer continued using the averaging distance method with Labor [38,39]. Good results were reported, although different values of $a_0$ were used for the same carbon / epoxy material system; $a_0$ = 2.3mm in [38], and $a_0$ = 6.2mm in [39]. Testing and analysis by Morris and Hahn [40] also showed the averaging dimension depended on laminate lay-up.

Kim and Soni [41] used the averaging distance method to predict free-edge delamination in carbon / epoxy laminates under axial tension and compression. They obtained the average through-thickness tensile stress near the free-edges and compared it with the in-plane transverse strength. Thus, by assuming transverse isotropy and $a_0$ = 1 ply thickness, they were able to predict the onset of delamination reasonably well for laminates with six different lay-ups. The scale of the specimens was varied by changing the laminate thickness. The criterion matched the experimentally observed reduction in strength with increase in thickness reasonably well.

Fish and Lee [18] used their own criterion, (2.11), and the simple maximum interlaminar shear stress criterion, in conjunction with the averaging distance method, to predict delamination in two types of multidirectional glass / epoxy laminates. They tried using four different averaging distances: ½ a ply thickness; 1 ply thickness; 1½ ply thicknesses; and 2 ply thicknesses. When using the maximum interlaminar shear stress criterion with $a_0$ = 1 ply thickness, the predicted locations of delamination matched the experimental observations, and the predicted failure loads fell within 3% of the experimental results. However, their modified Tsai-Wu criterion was not very successful and was more sensitive to the averaging distance.

Zhou and Sun [42] applied the averaging distance method with the quadratic stress criterion, (2.8a), given earlier, to predict free edge delamination in carbon / epoxy laminates. The predicted failure loads were very close to the experimental values, but this time an averaging distance of 2 ply thicknesses was used.

Shokrieh and Lessard [16] used their quadratic stress criterion, (2.9), which takes account of non-linear shear stress - strain response, to predict the initiation of free-edge delamination at circular holes in three different carbon / epoxy laminates. They criticised the Whitney-Nuismer methods for lacking physical meaning and quoted the use of four different values of $a_0$ found in the literature. However, their alternative was not by any means more rational. They used the stresses averaged over each element in their finite element model, which means their predictions were mesh size dependent. Nevertheless, comparison with the test results was quite good. Predictions assuming linear-elasticity, i.e. using (2.8a), were very unconservative.

### 2.3.2 Strain energy release rate methods

Among the first to apply the strain energy release rate approach to study delamination in composites were Rybicki et al [43]. They applied the virtual crack closure technique using the finite element method to obtain the strain energy release rate for free edge delamination in a multidirectional boron / epoxy laminate under axial tension. From the curves of the total strain energy release rate against crack length they were able to determine when the propagation switched from stable to unstable. There was good correlation with the test results.

Later, Wang and Crossman [44] and Crossman et al [45] made quantitative predictions of free edge delamination in carbon / epoxy laminates. Again , they used the total strain energy release rate and assumed $G_c$ to be independent of mode ratio. Using the maximum values of G from the graphs of G against crack length, they predicted the onset of delamination at loads very close to the averaged experimental values.

A very similar approach was taken by O'Brien [46]. He found the strain energy release rate reached a constant asymptotic value after a short crack propagation. This value matched the value from an analytical solution he derived, and was used to predict the load at the onset of free edge delamination in carbon / epoxy laminates. Specimens were manufactured with three different thicknesses and the total strain

energy release rate criterion, (2.17), predicted the reduction in failure strain with specimen thickness reasonably well. Shortly after, he studied the effect of mode ratio more closely [47]. Three multidirectional carbon / epoxy laminates were designed to produce different mode ratios at the free edges when loaded in tension. As expected, failure was found to depend on the mode ratio, and the mode I component dominated the onset of delamination.

Years later, Wang [48] used the maximum total strain energy release rate to predict free edge delamination in carbon / epoxy laminates, even though there was mixed mode loading. However, account was taken of the thermal residual stresses when calculating G, and reasonably good agreement with experimental results was obtained.

Finn and Springer [49] described a strain energy release rate approach for predicting delamination growth initiating at transverse matrix cracks and propagating along the interfaces with uncracked plies. They assumed the strain energy release rate was equal to the strain energy per unit area in the block of transversely cracked plies. In other words, they neglected the change in strain energy in the surrounding uncracked plies. Finn et al [50] then applied the approach to predict the size and shape of delaminations in several different carbon / epoxy, carbon / toughened epoxy and carbon / PEEK laminates under out-of-plane loading. There was good agreement with experimental results.

Delamination from transverse matrix cracks was also predicted by Takeda and Ogihara [51], but in this case for laminates under in-plane tension. They derived a closed form solution for G, and assuming $G_c = G_{IIc}$ were able to accurately predict the delamination length as a function of axial strain for three types of laminate.

Lammerant and Verpoest [52] predicted delamination growth from transverse matrix cracks in carbon / epoxy cross-ply laminates under out-of-plane shear loading. Using the virtual crack closure technique with the finite element method, they predicted delamination growth at the same locations as those observed in the tests. The loads at delamination growth were predicted reasonably well.

### 2.3.3 Use of both stress and strain energy release rate

Brewer and Lagace [53] applied a stress criterion similar to (2.8a) along with the averaging distance method to predict free edge delamination in carbon / epoxy laminates. Specimens were prepared with three different lay-ups and five thicknesses in each case. By best fitting all the test data, they obtained a value for the interlaminar shear strength and a value for the averaging distance, $a_0$ = 0.178mm (which is different from all the previously quoted values of $a_0$ for carbon / epoxy). They then calculated the strain energy release rate for edge delamination in the specimens and obtained a value of $G_c$ for each family of lay-up by best fitting each set of experimental data. The average stress approach generally modelled the size effect more accurately than the strain energy release rate approach. However, this might be due to the fact that there were more empirical constants to best fit the data in the stress based approach.

Cui et al [54] compared several stress based failure criteria and the strain energy release rate criterion, for predicting delamination in unidirectional glass / epoxy specimens waisted through the thickness. In this case, where there were no stress singularities, the stress based criteria were more successful than the strain energy release rate approach. There was not a great deal of difference between the predicted failure loads with the different interactive stress based criteria.

Cui et al [55] also made a comparison of failure criteria for predicting delamination in glass / epoxy specimens with discontinuous plies. In this case, there were stress singularities. Application of both the Whitney-Nuismer methods with the Tsai-Wu criterion showed that the characteristic distances, $a_0$ and $d_0$, were not material constants. Application of the total strain energy release rate criterion, (2.17), showed that $G_c$ was a function of the ratio of discontinuous to continuous plies, and the scale of the specimen. However, the former could be due to different mode ratios between specimens with different numbers of discontinuous plies. On the whole, the strain energy release rate approach was more accurate than the stress based approaches.

Davies and Robinson [56] analysed quasi-isotropic carbon / epoxy plates with different thicknesses under out-of-plane loading. Using the maximum shear stress criterion they predicted the damage area as a function of impact force. There was good correlation with the test data for 1mm thick plates, but not for the 2mm and 4.3mm plates. A closed form solution for the delamination strain energy release rate in the plates was derived. Using the value of $G_c$ from ENF tests, the loads at the initiation of damage were predicted reasonably well for all the plates.

Minguet and O'Brien [23] used the maximum stress criterion to determine the location and initiation load of matrix cracking in carbon / epoxy skin-stringer specimen in four-point bending. There was good agreement with the test data. Finite element analysis was then conducted and the strain energy release rate was found for delamination from the location of damage initiation. This was done using the change in total energy approach, described in section 2.2.2. The first value of G on the curve of G verses crack length was used to predict failure. There was good agreement with the experimental results, but since the initial value of G was used, his approach was very mesh size dependent.

Hwu et al [34] overcame the mesh size dependency problem by assuming the initial crack length was equal to a characteristic defect size. They used the mixed-mode strain energy release rate criterion, (2.18), with m = 1.25 and n = 1.5, to predict the locations and onset loads of free edge delamination in four different types of glass / epoxy specimens. Assuming an initial flaw size of 1 ply thickness, the failure loads were predicted within 10% of the experimental results, and the right delamination locations were predicted in every type of specimen. They also applied the quadratic stress criterion, (2.8a), using the stresses averaged over a distance of 2 ply thicknesses. The predicted delamination locations were correct and the failure loads from the analysis were within 7% of the test data.

However, when similar specimens were prepared with 4mm edge delaminations by using PTFE inserts, the strain energy release rate approach gave failure loads within 8% of the experimental results, whilst the stress based criterion gave discrepancies of

more than 20%. Thus, the stress based criterion worked better than the modified strain energy release rate approach when there was no initial damage, and in cases where there was an existing crack, the strain energy release rate approach worked best.

Work by Davies et al [57,58] appears to reflect this. In [57], delamination was predicted in a carbon / epoxy quasi-isotropic circular plate under a uniform pressure. The maximum interlaminar shear stress criterion was used to predict the initiation of fracture, and the strain energy release rate approach was then used to predict the growth of delamination. Low velocity impact tests were also performed on woven glass / phenolic resin laminates. The analysis showed that a stress based criterion was needed to predict the initiation of damage but that the strain energy release rate approach became more suitable after the damage area had grown. Similar conclusions were drawn in [58], from a study of delamination in circular carbon / epoxy laminates in bending.

## 2.4 Discussion

From the literature survey given above we can see there is a large amount of work on predicting free edge delamination in flat laminates under in-plane loading. A reasonable amount of work has been done on predicting delamination in laminates with transverse matrix cracks. There are a few papers on delamination in laminates with discontinuous plies under in-plane loading, and delamination due to through-thickness shear loading. Little or no work was found on predicting delamination in curved laminates with discontinuous plies, or laminates with discontinuous plies under out-of-plane loading. Therefore, the work in this thesis will help fill a gap in the field of research.

Comparing the different prediction methods we see that stress based failure criteria are useful tools for predicting the initiation of delamination when there are no stress singularities present. No particular stress criterion stands out as being the most

successful, although the form given in (2.8a) seems to be quite popular. When there are stress singularities or existing cracks, the strain energy release rate approach, via the virtual crack closure technique, seems to work well as long as the mode ratio is accounted for. Again, no particular criterion stands out as being the most successful, although the form given in (2.18) is the most popular and easy to use.

The Whitney-Nuismer methods are less recommendable since the characteristic distances are obviously not material constants and depend on the lay-up of the laminate. Furthermore, the physical foundation on which they are based is not as strong as the strain energy release rate approach. However, when the latter approach is used for situations where no crack is present, an initial defect has to be assumed. The size of this initial defect was previously ambiguous, but work in this thesis will show you can relate it to the size of the yield or damage zone at the stress singularity. Since the yield zone size is estimated from the calculated stress distribution, the initial crack size is not ambiguous.

The use of a stress based criterion to predict damage initiation, and then a strain energy release rate criterion to predict damage growth, seems to be the way ahead. This approach can be automated by using specially designed elements which model the interface between plies in a finite element model. Work in this area is still in its early stages of development. Chapter 8 in the thesis will survey work by the other authors in this field, and the approach will be applied to straight and curved laminates with discontinuous plies.

There was much work in the literature reporting the use of either the averaging distance method, or the strain energy release rate approach, for modelling the reduction in strength with increasing laminate thickness. On the whole, both methods worked reasonably well. However, both these methods are used for predicting delamination from stress singularities or geometric discontinuities. When these are not present in the structure there is still a reduction in strength with increasing stressed volume. To take account of this volumetric size effect another approach has to be taken. This is the subject of the next chapter.

# Chapter 3

# Weibull Theory Applied to Curved Laminates

## 3.1 Introduction

Curved laminates under out-of-plane loading can fail due to a combination of through-thickness tensile and interlaminar shear stresses. When there are no geometric discontinuities which can cause stress singularities, failure can be predicted with a stress based failure criterion, such as those given in section 2.1.2. Some experimental studies on through-thickness failure criteria have been performed, for example using waisted tensile specimens [54], or curved beams in tension [10], but there was a need for further experimental data. Therefore, a type of specimen was designed and tested to look at the problem of combined interlaminar shear and tension, and to see if a simple stress based failure criterion was able to accurately predict failure [2].

From the analysis it was found that the peak tensile stress in some of these specimens was higher than the interlaminar tensile strength measured previously [60] from specimens with no shear stress. However, the volume of highly stressed material in the former type of specimen was much smaller than that in the latter type of specimen. Thus, account was taken of the volumetric size effect to try to explain the

discrepancy. After adjusting the stresses using Weibull theory, the failure envelope matched a simple stress based failure criterion reasonably well.

## 3.2 Description of specimens

The author was not involved with the design and testing of these specimens. However, a summary will be given to introduce the reader to the analysis. A more exhaustive description of the specimen manufacture and testing is given in [2].

A schematic diagram of the specimen and test arrangement can be seen in figure 3.1. The specimen consists of 32 plies of unidirectional E glass / 913 epoxy cured in the form of a miniature croquet hoop, and is loaded in three-point bending. The shape of the hoop incorporates three straight portions and two 90° curved portions. The out-of-plane shear force caused by the central loading roller produces interlaminar shear stresses, and the bending moment gives rise to through-thickness tensile stresses in the curved portions of the specimen. The maximum values of both types of stresses occur in the curved portions of the specimen near the border with the central straight section. Thus, failure is due to a combination of the two types of stress.

Furthermore, the ratio between the two types of stress could be changed simply by varying the lengths of the two straight "leg" portions. This is because longer legs splayed out more during loading, thus giving rise to higher bending moments in the curved sections. Hence, longer specimens had a higher relative through-thickness tensile stress compared to the interlaminar shear stress. Specimens were manufactured with two different lengths to obtain the strengths corresponding to two different ratios of interlaminar stress. The distance between the ends of the specimen to the inside of the central flat surface was 13mm for the short specimens and 50mm for the long specimens, as seen in figure 3.1.

Several specimens of both lengths were cut to a width of 10mm and loaded until failure. Failure was due to interlaminar cracking close to the mid-thickness of the

specimens. Crack propagation was unstable and extended around most of the length of the specimens. The bending strain and load at failure were recorded in each test. The bending strain was measured by a strain gauge placed directly under the loading roller. Tables 3.1 and 3.2 show the loads and strains recorded at failure, together with the measured specimen dimensions.

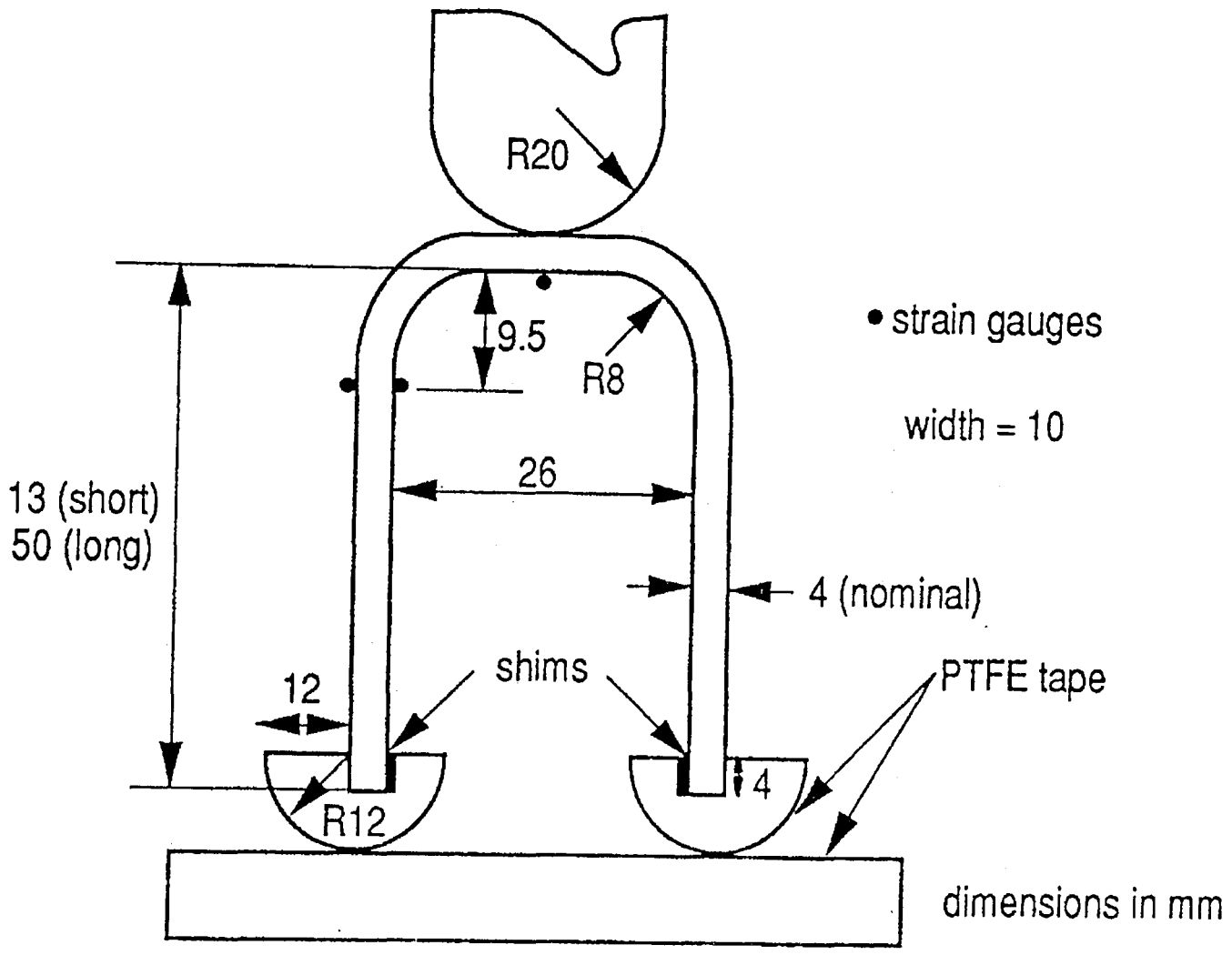


**FIG. 3.1** Schematic diagram of hoop specimen and test arrangement

| Speci -men no. | Width (mm) | Mean thickness of curved portions (mm) | Thickness of straight central section (mm) | Load at failure (N) | Strain at failure |
|---|---|---|---|---|---|
| 1 | 10.04 | 3.78 | 4.36 | 2651 | 0.02628 |
| 2 | 10.00 | 3.73 | 4.24 | 2498 | 0.02809 |
| 3 | 10.03 | 3.80 | 4.39 | 2737 | 0.02815 |

**TABLE 3.1** Summary of results for long specimens

| Speci -men no. | Width (mm) | Mean thickness of curved portions (mm) | Thickness of straight central section (mm) | Load at failure (N) | Strain at failure |
|---|---|---|---|---|---|
| 1 | 9.92 | 3.75 | 4.34 | 3665 | 0.02789 |
| 2 | 10.04 | 3.83 | 4.40 | 3860 | 0.02705 |
| 3 | 9.45 | 3.66 | 4.24 | 3381 | 0.02782 |
| 4 | 9.34 | 3.72 | 4.31 | 3103 | 0.02380 |

**TABLE 3.2** Summary of results for short specimens

## 3.3 Finite element analysis

A two dimensional linear elastic finite element analysis was carried out to determine the interlaminar stresses in the test specimens. The analysis was performed using ABAQUS [59], with four noded plane stress elements of type CPS4. Small deflection theory was used. The mesh is shown in figure 3.2, together with the boundary conditions. Forces and boundary conditions were applied to produce the correct loading in the curved section based on the experimental measurements. Due to symmetry it was only necessary to analyse half of the specimen. Only the first five mm of the leg of the specimen was modelled. This was sufficient to allow the loads to be applied without affecting the stresses in the curved section. The elements in the curved section measured 0.25mm in the thickness direction and about 0.25mm in the circumferential direction.

The thickness of the specimen was modelled as constant. Although in practice it was higher in the flat portions, these were only included in order to introduce the load correctly into the curved section, and so accurate specification of the thickness was not critical. A value of 3.75mm was used, based on the average thickness of the curved sections for the two types of specimen.

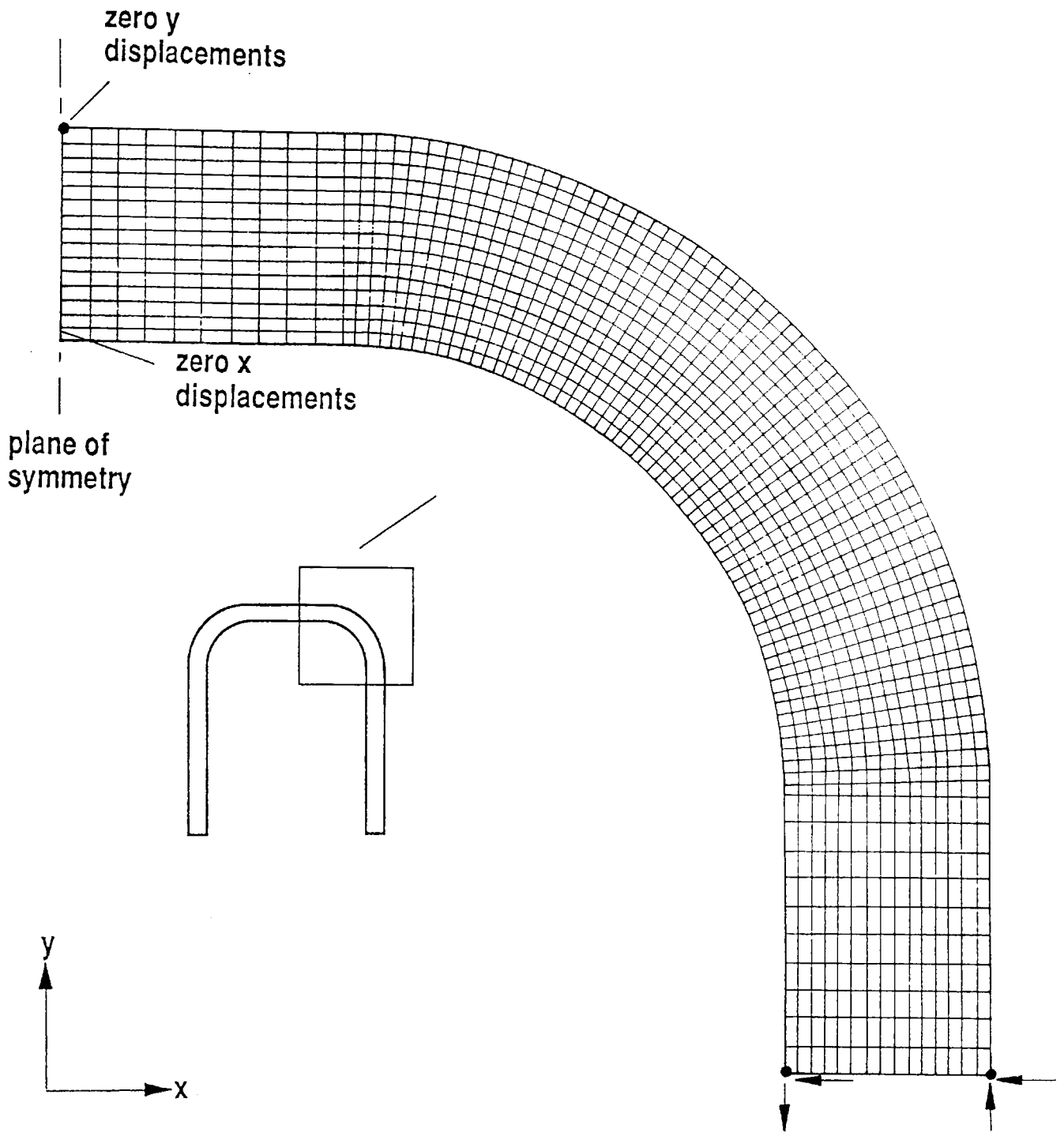


**FIG. 3.2** Finite element model and boundary conditions

The material properties for E glass / 913 epoxy are shown in table 3.3. These correspond to a nominal ply thickness of 0.127mm, and are based on in-plane measurements assuming transverse isotropy. The fibre direction modulus was corrected for volume fraction based on the average thickness of the curved section, by multiplying by the ratio of nominal thickness to measured thickness. This gave a corrected value of $E_1$ of 47.6 GPa. No corrections were applied to the other values. For the curved section, properties were defined in a cylindrical coordinate system.

| | |
|---|---|
| Fibre direction modulus, $E_1$ (GPa) | 43.9 |
| Transverse modulus, $E_3$ (GPa) | 15.4 |
| Shear modulus, $G_{13}$ (GPa) | 4.34 |
| Poisson's ratio, $\nu_{13}$ | 0.3 |

**TABLE 3.3** Material properties for finite element analysis

Symmetric boundary conditions were applied at the mid-plane, and a vertical restraint was imposed at the centre on the top surface at the point of contact of the roller. Forces were applied to the lower end of the beam to reproduce the loading in the curved section at failure as closely as possible. Based on the mean experimental loads per unit width at failure, upward vertical forces of 131.1 N/mm and 180.5 N/mm were applied to the half models of the long and short specimens respectively. For simplicity, these were applied as two equal point forces at nodes on the two surfaces of the specimen.

The moments per unit width at the centre of the beams were calculated from the strains, $\varepsilon$ recorded by the gauges under the loading rollers. The thickness at the centre, $t_{cen}$, was significantly higher than that in the curved section, and so the volume fraction must have been proportionately lower. The Young's modulus, $E_1$ from table 3.3 was therefore corrected by the ratio of the nominal thickness of 4.064mm to the thickness $t_{cen}$ at the location of the strain gauge. The moment per unit width M is therefore given by:

$$M = 4.064E_1.\varepsilon.t_{cen} / 6 \qquad (3.1)$$

The average values for the long and short specimens were 3541 Nmm/mm and 3424 Nmm/mm respectively. This moment is caused mainly by the vertical force at the contact point between the lower cylindrical rollers and the flat plate. However, there is also a contribution resulting from the horizontal force acting due to friction. The magnitude of this is uncertain, but it can be estimated based on an assumed coefficient of friction of 0.05.

The moments at the centre of the specimens due to the vertical and horizontal forces applied at the lower end were calculated, and hence the additional moments to apply at the end of the model to produce the correct central moment were determined. The effect of any change in geometry due to deformation of the specimen was ignored. The moments calculated were 1688 Nmm/mm and 873.3 Nmm/mm for the long and short specimens, respectively. These moments were applied as two equal and opposite forces at the two corner nodes on the surface of the lower end of the model.

Since the horizontal forces due to friction were only estimated, the analyses were repeated without these forces. The applied moments were adjusted to give the same central moments and the results compared to see how much effect the frictional forces had on the stresses in the curved section.

To check the accuracy of determining the bending strain from the central strain gauge, two additional strain gauges were attached on one of the legs on one of the long specimens, as seen in figure 3.1. The strain gauges were positioned on either side of the top of the leg, 9.5mm below the lower surface of the central straight section. The bending moment at the location of the strain gauges was calculated from the gauge readings, and the central moment was then determined based on the geometry of the specimen and the applied load. The value differed by about 5% from the bending moment estimated from the central strain gauge. This confirms that the procedure for calculating the moment is reasonable.

Figure 3.3 is a contour plot of the interlaminar tensile stresses for the short specimens. Only the curved section and the central flat portion is shown. The stresses are negligible in the straight section, as expected. In the curved section they increase from approximately zero on the surfaces up to a peak near the centre of the specimen. The maximum value is 86.1 MPa, towards the end nearest the central loading roller. Away from this point the stresses reduce as the bending moment decreases. Stresses at the surface are not exactly zero, because of the size of the elements, and the way the stresses are extrapolated out to the nodes based on the assumption of the 4 noded elements that the stress is constant through the thickness. Refining the mesh would

reduce these stresses. However, the values at the centre of the elements and where stresses from elements on either side are averaged would not be greatly affected by further mesh refinement.

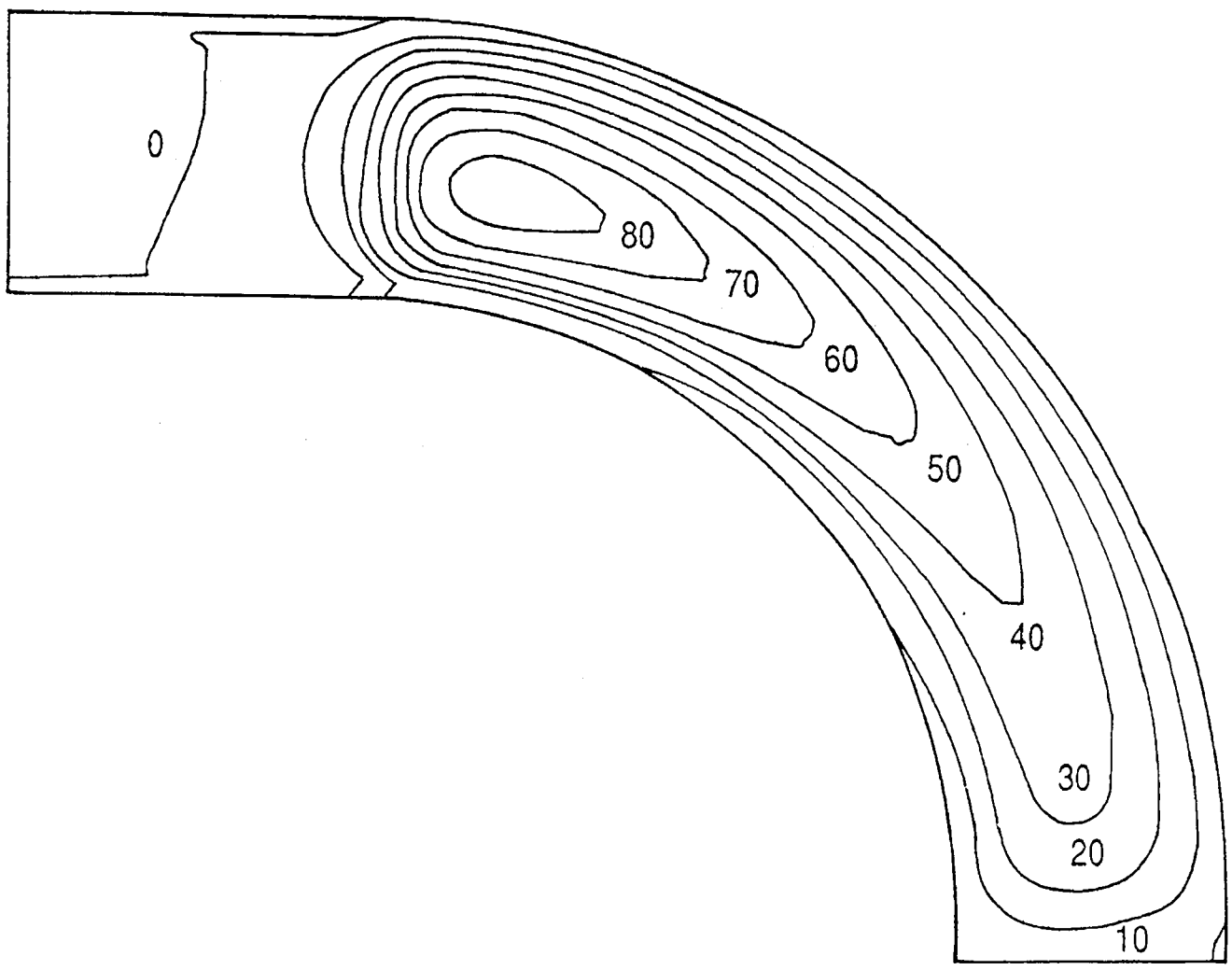


**FIG. 3.3** Through-thickness tensile stress distribution in short specimen (MPa)

Figure 3.4 shows a similar plot for the interlaminar shear stresses. The plot shows the expected distribution from close to zero stress near the surfaces up to a maximum near the centre of the specimen in both the curved and straight sections. The maximum value of -77.3 MPa occurs at the end of the curved section near the loading roller. This is close to the location of maximum interlaminar tensile stress. Interlaminar shear stresses also reduce around the curved section due to the change in angle, which means that the shear force is gradually transformed into a compressive axial force.

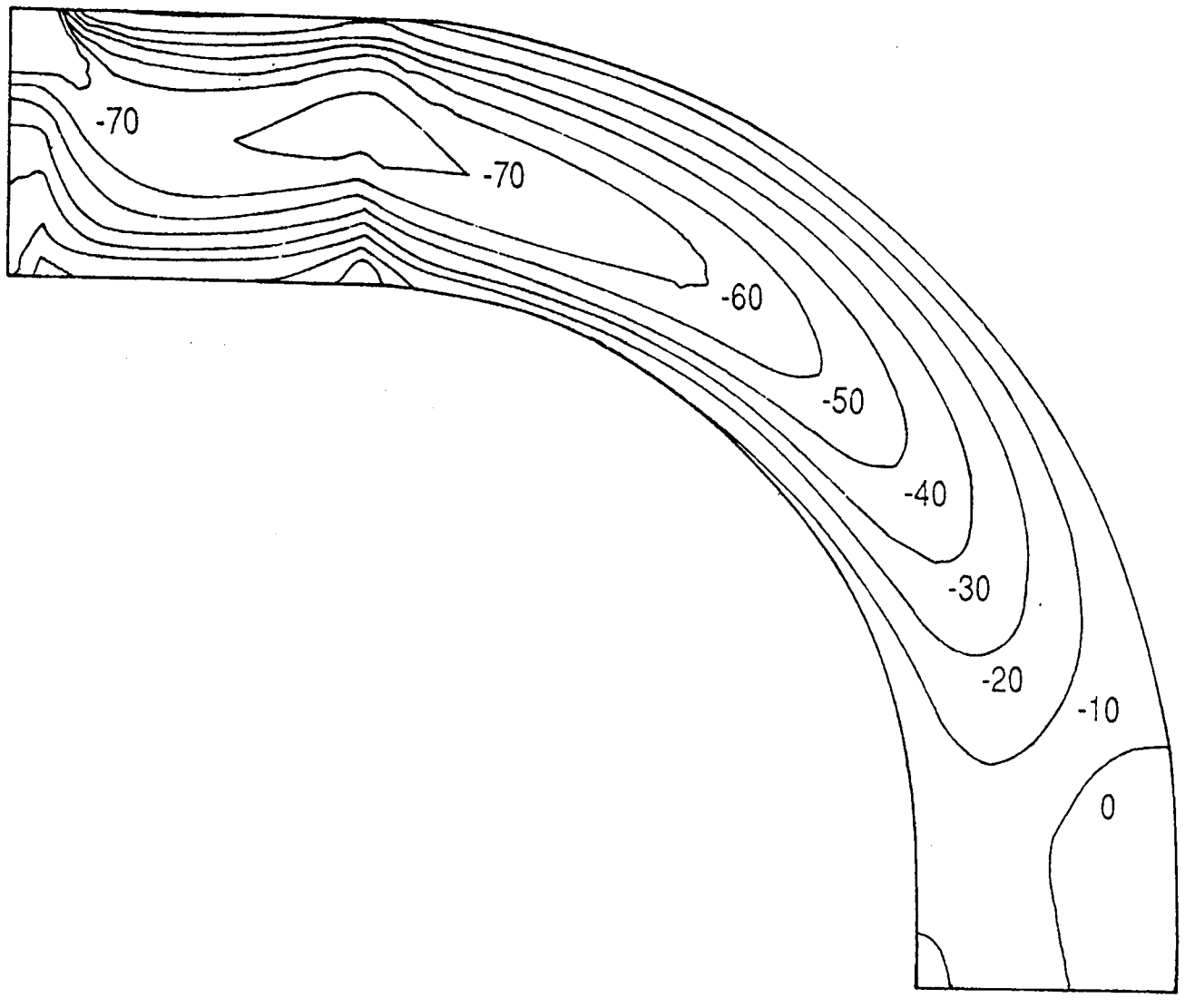


**FIG. 3.4** Interlaminar shear stress distribution in short specimen (MPa)

There is a disturbance in stress at the transition from the central flat section to the curved section. This is caused by the ending of the curvature induced radial forces modifying the distribution of shear stress at the start of the straight section. As with the tensile stresses, interlaminar shear stresses should be exactly zero on the surface, and the small values shown on the plot are due to the way the stresses are extrapolated out to the nodes. High stresses arising near the point of roller contact have not been shown on the plot because they are very localised, and not believed to be representative. If the loading arrangement had been fully modelled with contact over an area rather than at a point, these stresses would have been much lower.

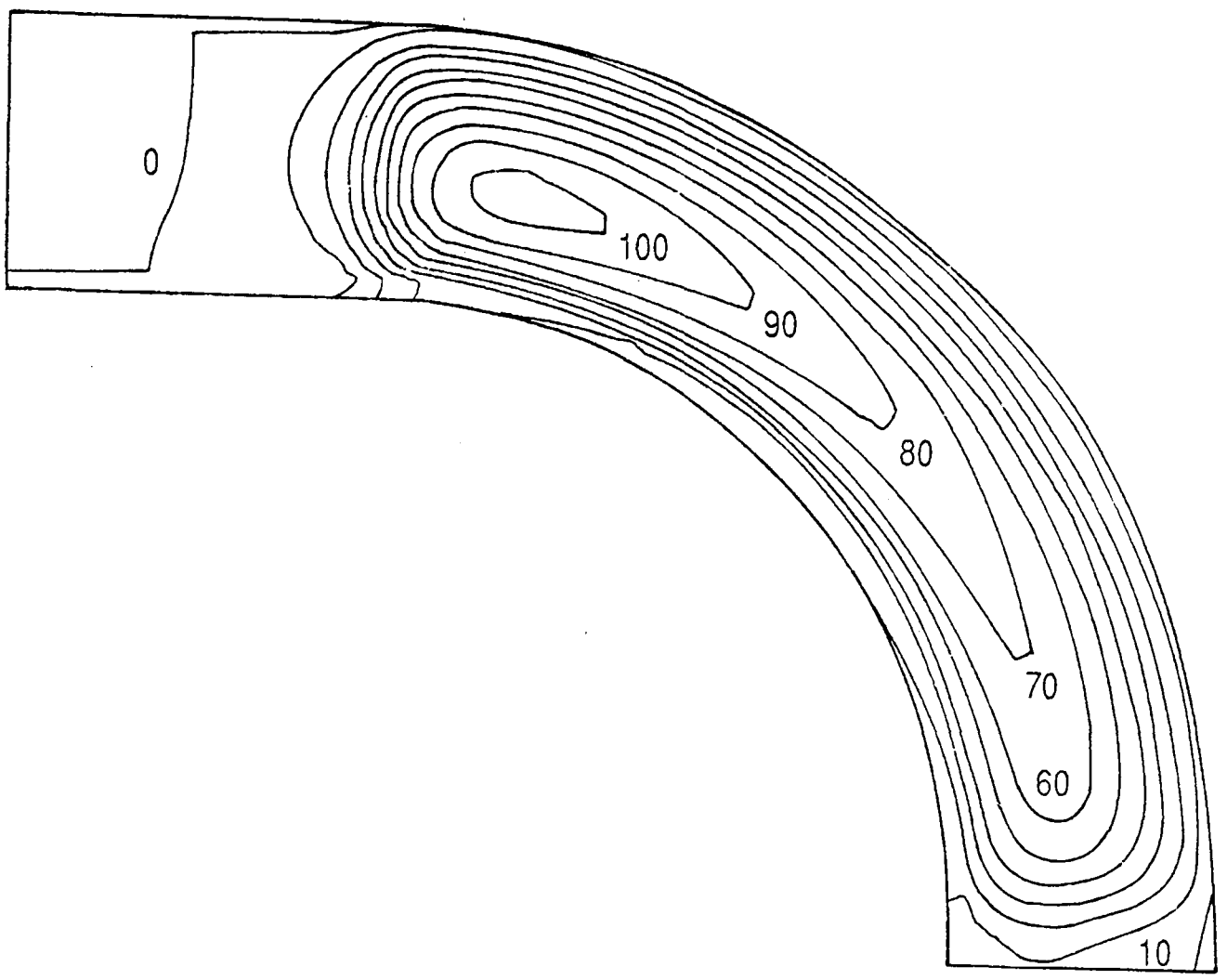


**FIG. 3.5** Through-thickness tensile stress distribution in long specimen (MPa)

Figures 3.5 and 3.6 show similar contour plots of interlaminar tensile and shear stresses for the long specimens. The overall distributions of stresses are very similar, although the interlaminar shear stresses are lower, with a peak value of -62.6 MPa, and the interlaminar tensile stresses are higher, with a maximum of 104.4 MPa.

Repeating the analysis without the frictional forces gave very similar results. For both the short and long specimens, the maximum interlaminar shear and tensile stresses were the same as before. Stresses around the curved section were also very similar. For example for the short specimen, at a point about 30° around the curve, the maximum tension and shear stresses were 66.8 and 62.1 MPa compared with 67.4 and 60.3 MPa with the frictional force included. Differences were even less for the long specimens. This shows that the results are relatively insensitive to how the load is applied provided that the bending moment and shear force in the critical area are

correct. Since these were based on experimentally measured values, the analysis should be accurate despite the uncertainty in the value of friction coefficient.

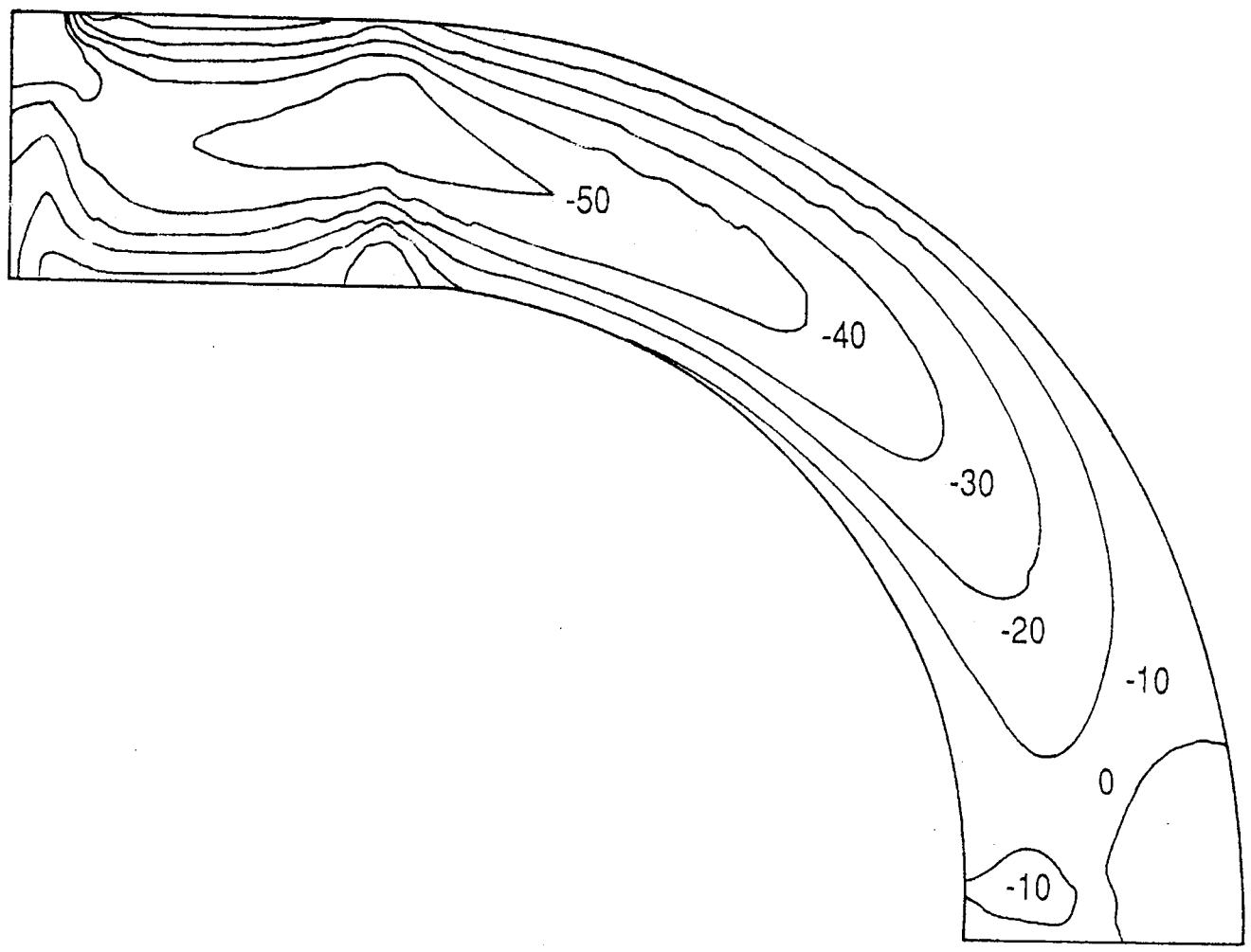


**FIG. 3.6** Interlaminar shear stress distribution in long specimen (MPa)

## 3.4 Interpretation of test results

The experimental results can now be assessed in the light of the stresses at failure calculated by the finite element analysis. In order to compare them with strengths due to interlaminar tension alone, the results from curved beams loaded in pure bending are used. Specimens of the same material, and with the same thickness, width and radius of curvature were previously tested in four point bending [60]. An interlaminar tensile strength of 95.1 MPa was deduced from the results. Straight specimens from the same plates of material were tested in a short beam shear fixture where there are no interlaminar tensile stresses present. The results showed an interlaminar shear

strength of 90.0 MPa [60]. Schematic diagrams of the two types of specimen and test arrangement can be seen in figures 3.7 and 3.8. A full description is given in [60].

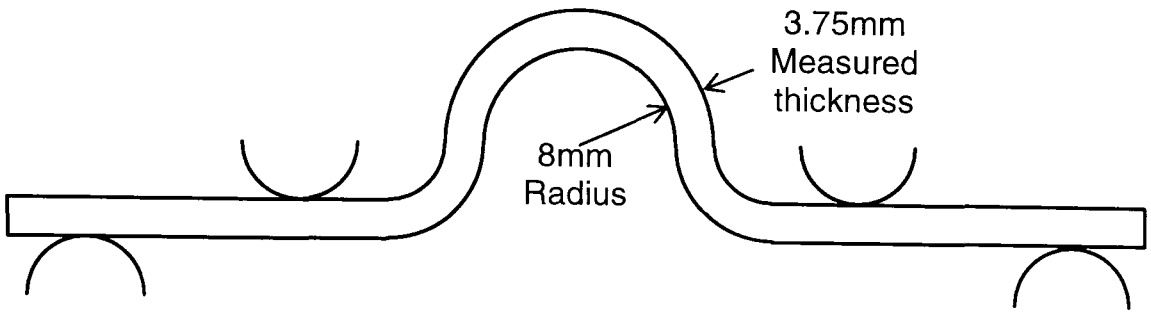


**FIG. 3.7** Test to measure interlaminar tensile strength

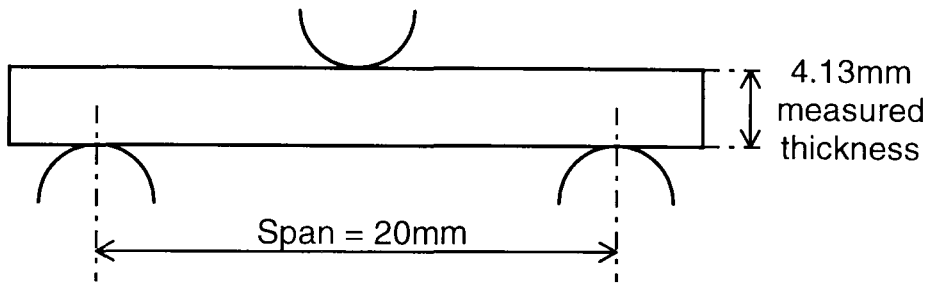


**FIG. 3.8** Test to measure interlaminar shear strength

As mentioned at the end of the previous chapter, no particular stress criterion stands out as being the most successful, but the form given in (2.8a) seems to be quite popular and takes account of the interaction between the stresses. When there are no through-width shear stresses, $\tau_{23}$, the criterion reduces to:

$$\left(\frac{\sigma_3}{Z}\right)^2 + \left(\frac{\tau_{13}}{S}\right)^2 \geq 1 \qquad (3.2)$$

where $\sigma_3$ is the interlaminar tensile stress, $\tau_{13}$ is the interlaminar shear stress, and Z and S are the respective strengths. This simple quadratic interaction equation will be used in this study.

Figure 3.9 shows the experimental results for the hoop specimens compared with the expected results based on (3.2) and the strengths for specimens loaded in tension and

shear alone. It can be seen that the fit is quite poor for both types of specimen, with the actual strengths lying well beyond the failure envelope. In fact the interlaminar tensile stress at failure for the long specimens, where a substantial shear stress is also present, is higher than that for specimens subject to interlaminar tension alone.

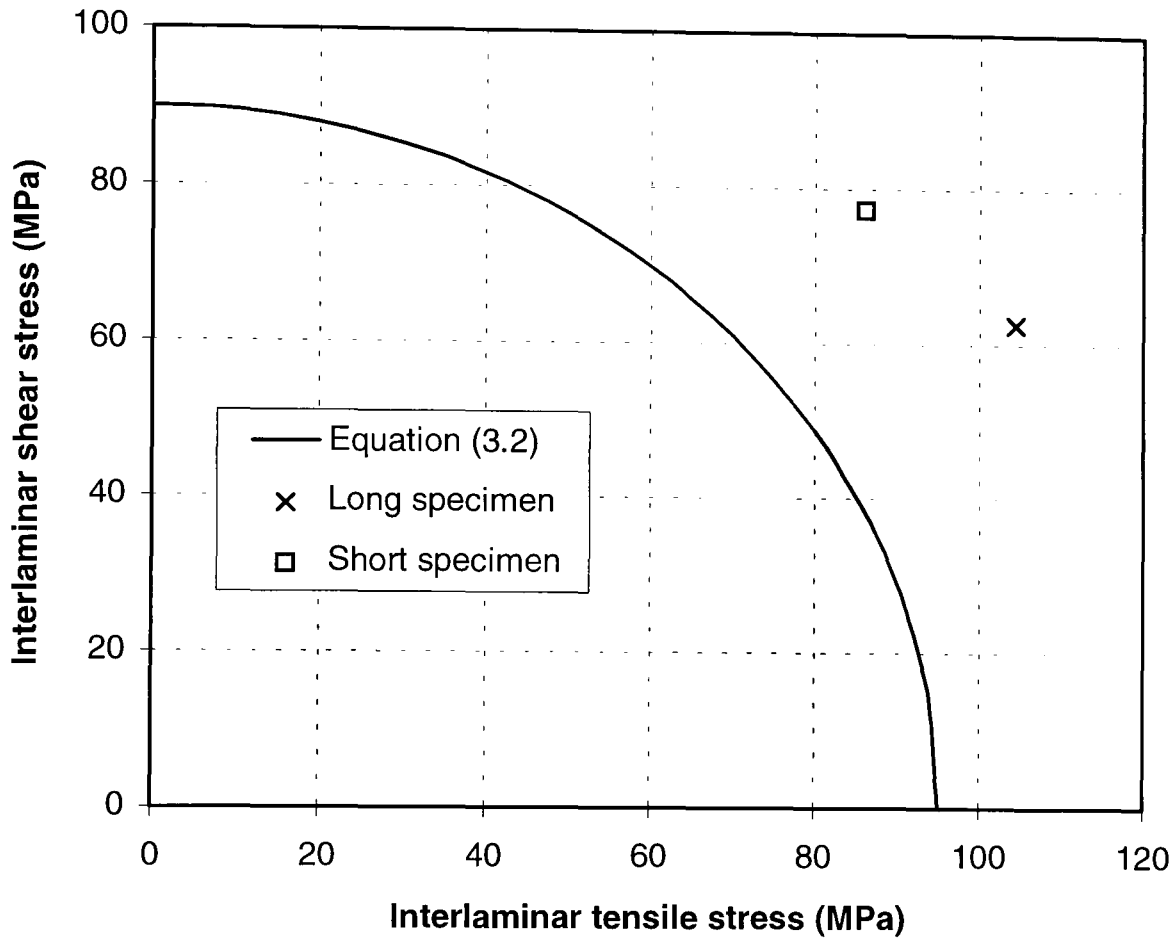


**FIG. 3.9** Maximum stresses at failure

At first sight this is a rather surprising result, and makes attempts at establishing a failure criterion for interaction between these stress components look rather difficult. The explanation is believed to be related to the volume of material under stress. It can be seen in figures 3.3 - 3.6 that the maximum stresses occur over a relatively small area. In contrast, for the tests used to establish the interlaminar tensile and shear strengths, the stress distributions were constant along the length of the specimens, and so much larger volumes of material were subject to the maximum stress. When specimens of different sizes were tested, with all dimensions scaled, a substantial variation in strength was found, particularly for interlaminar tension [60].

Scaled specimens with linear dimensions increased by a factor of 4 were found to give interlaminar tensile and shear strengths 44% and 12% lower respectively than similar small specimens.

It is therefore necessary to take account of this size effect in order to explain the apparently higher strength under combined shear and tension than under pure tension, and to develop a more accurate method of predicting failure.

## 3.5 Introduction to Weibull theory

The strength of brittle materials, such as glass or carbon, exhibits a dependency on volume. For example, if two glass fibres of equal diameters but different lengths were to be put under a gradually increasing load, the longer fibre would be likely to fail first. Griffith [21] attributed this to the existence of microscopic flaws or cracks in the material. Since the size and position of these flaws are random, a larger volume of material is likely to contain a larger flaw, and thus would be expected to have a lower apparent strength. However, this randomness means there will be scatter in the data.

Later, Weibull [61] proposed a statistical method of predicting the strength of brittle materials. He defined the survival probability, $P_s$, of a sample of brittle material under a uniformly distributed tensile stress, $\sigma$, as:

$$P_s = \exp\left\{-\left(\sigma/\sigma_0\right)^m\right\} \tag{3.3}$$

where $\sigma_0$ is the characteristic strength and m is the Weibull modulus. The above function results in probability distributions such as the ones in figure 3.10. The values of $\sigma_0$ and m can be found by fitting experimental data, and are assumed to be material constants. The higher the value of m, the more well-defined the failure stress is, and the lower the value of m, the more scatter there is in the data.

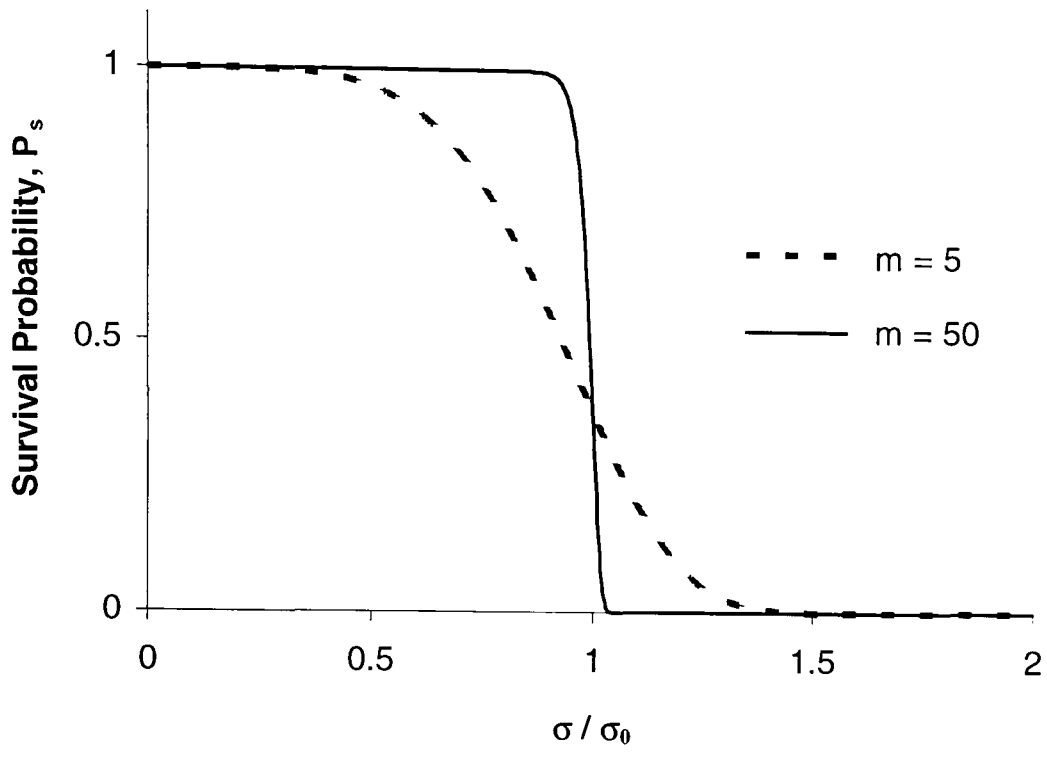


**FIG. 3.10** The Weibull distribution function

Let the definition of $P_s$ in (3.3) correspond to samples of volume $1mm^3$. The probability of n such identical samples all surviving is $P_s^n$. If all the samples were joined together to form a chain of volume n x $1mm^3$, the survival probability would still be $P_s^n$, since failure in one of the samples would result in failure of the chain. Hence, the survival probability of a chain of volume V, is:

$$P_s(\text{chain}) = P_s^V = \exp\left\{-V\left(\sigma/\sigma_0\right)^m\right\} \tag{3.4}$$

From this we can see that at a particular applied stress, Weibull theory predicts a decreasing probability of survival for an increasing volume. Alternatively, the predicted mean failure stress will decrease as the volume increases, and the extent to which this occurs is related to the value of m. A lower value of m will result in a stronger size effect.

Now, let us consider a structure of volume V under a non-uniform stress distribution. If we divide the structure into infinitely small elements of volume dV, and assume

failure of one of the elements results in failure of the whole structure. then the survival probability of the whole structure is equal to the product of the survival probabilities of each of the elements. Hence,

$$P_s = \exp\left\{-\int\left(\sigma/\sigma_0\right)^m dV\right\} \tag{3.5}$$

Note that the probability of failure, $P_f$, is simply,

$$P_f = 1 - P_s = 1 - \exp\left\{-\int\left(\sigma/\sigma_0\right)^m dV\right\} \tag{3.6}$$

For composites, this approach has been applied mainly to tensile failure. It is able to take account of both the effects of specimen size and stress gradients on strength [62-64]. Weibull theory can also be applied to interlaminar failure of composites [60,65], and is reasonably straightforward when there is only one stress component of interest. Statistical approaches have also been proposed where there are several stress components which interact to cause failure [66,67], although the situation becomes more complicated in this case. A pragmatic approach is adopted here whereby failure due to each of the stress components acting on its own is considered first, and then the interaction is accounted for.

## 3.6 Application of Weibull theory in present study

Taking first the interlaminar tensile stresses, the probability of failure is given by:

$$P_f = 1 - \exp\left\{-\int\left(\sigma_3/\sigma_0\right)^{m_3} dV\right\} \tag{3.7}$$

where $\sigma_0$ and $m_3$ are the Weibull parameters for interlaminar tensile failure.

An equivalent constant interlaminar tensile stress, $\overline{\sigma}_3$, is then calculated. This is defined as the constant stress which when acting on the same volume of material as the actual variable stress distribution $\sigma_3$, gives equal probability of failure:

$$P_f = 1 - \exp\left\{-V\left(\overline{\sigma}_3 / \sigma_0\right)^{m_3}\right\} \tag{3.8}$$

Equating (3.7) and (3.8) gives:

$$\overline{\sigma}_3 = \left[\frac{1}{V}\int \sigma_3^{m_3} dV\right]^{1/m_3} \tag{3.9}$$

In the finite element analysis the volume integral is replaced by a summation over all the elements:

$$\overline{\sigma}_3 = \left[\frac{1}{V}\sum_{i=1}^{n} \sigma_{3i}^{m_3} V_i\right]^{1/m_3} \tag{3.10}$$

where $\sigma_{3i}$ is taken as the interlaminar tensile stress at the centre of element i, $V_i$ is the element volume, and n is the number of elements.

The interlaminar shear stresses are then considered on their own. In the same way the equivalent constant interlaminar shear stress, $\overline{\tau}_{13}$, which gives the same probability of failure as the actual variable shear stress distribution is,

$$\overline{\tau}_{13} = \left[\frac{1}{V}\int \tau_{13}^{m_{13}} dV\right]^{1/m_{13}} \tag{3.11}$$

where $m_{13}$ is the Weibull modulus for interlaminar shear. This can be approximated to the following for finite element analysis:

$$\bar{\tau}_{13} = \left[ \frac{1}{V} \sum_{i=1}^{n} \tau_{13i}^{m_{13}} V_i \right]^{1/m_{13}} \tag{3.12}$$

where $\tau_{13i}$ is the interlaminar shear stress at the centre of element i.

The interaction between interlaminar shear and tension is then accounted for by using the quadratic equation:

$$\frac{\bar{\sigma}_3^2}{\bar{Z}^2} + \frac{\bar{\tau}_{13}^2}{\bar{S}^2} \geq 1 \tag{3.13}$$

with $\bar{Z}$ and $\bar{S}$ being the failure stresses due to interlaminar tension and shear alone, for the same volume of material, V, as the specimen whose strength is to be predicted. These values need to be derived from experimental results, corrected for the variable stress distribution in the tests and for any difference between the volume of the test specimen and the volume V.

The scaled tests mentioned earlier did not give a consistent size effect for failure due to interlaminar tension and interlaminar shear [60]. The Weibull moduli $m_3$ and $m_{13}$ for these two failure modes were estimated to be 7.1 and 31.5, respectively. The approach adopted provides a relatively simple way of dealing with the interaction between these stress components, and avoids some of the difficulties arising from the different Weibull moduli for the different stress components.

Using these Weibull parameters, the corrected strengths $\bar{Z}$ and $\bar{S}$ were calculated. For interlaminar tension, this was done from a 2-D finite element analysis of the 180° curved section of the specimen shown in figure 3.7, assuming the bending moment to be constant. Equation (3.10) was then used to calculate $\bar{Z}$. No further correction was required because the volume of the curved section was the same as the volume of the two curved parts of the hoop specimens tested here. This gave an equivalent

interlaminar tensile strength, $\overline{Z}$, under uniform stress of 81.1 MPa. For comparison, the strength derived in [60] based on the maximum stress across the section was 95.1 MPa.

For the interlaminar shear strength, finite element analysis was not necessary. The parabolic shear stress distribution through the thickness of the short beam shear specimen was simply substituted into (3.11) to yield the following equation:

$$\overline{S} = \left[ \frac{s.w}{V} \int_{-t/2}^{+t/2} \left[ \left( \frac{P}{16I} \right) \left( t^2 - 4z^2 \right) \right]^{m_{13}} dz \right]^{1/m_{13}} \qquad (3.14)$$

where s is the span of the support rollers as seen in figure 3.8, w and t are the width and thickness of the specimen respectively, I is the second moment of area about the mid-thickness plane, z is the through-thickness distance from the mid-thickness plane, and P is the failure load at the central loading roller. The volume of the curved portions of the hoop specimens is substituted into V. This accounts for the difference in stressed volume between the short beam shear specimens and the hoop specimens.

The resulting equivalent interlaminar shear strength, $\overline{S}$, was 84.3 MPa, compared with the value determined previously of 90.0 MPa based on the maximum stress. The difference between these values is less than for the interlaminar tensile strengths because of the higher Weibull modulus for shear compared with tension.

Using the results of the finite element analysis presented in section 3.3 and equations (3.10) and (3.12), the equivalent constant stresses at failure were calculated for the long and short hoop specimens. These are shown in table 3.4. In figure 3.11 they are plotted together with the quadratic failure envelope from equation (3.13). The correlation is very much improved compared with figure 3.9, where no statistical effects were considered. For both cases the results are conservative, by 6% and 11% for the short and long specimens, respectively.

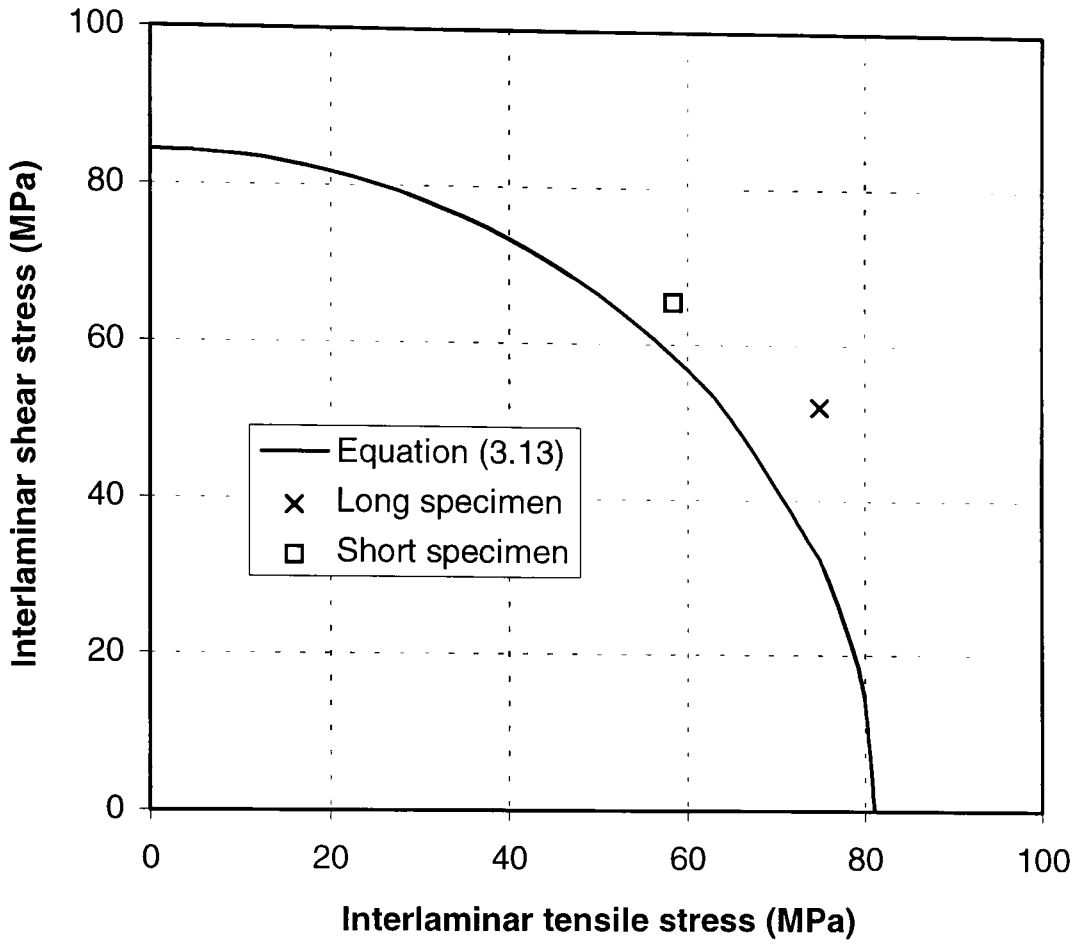


**FIG. 3.11** Equivalent stresses at failure corrected for volume effect

| | Long specimen | Short specimen |
|---|---|---|
| Interlaminar tensile stress, $\bar{\sigma}_3$ (MPa) | 74.9 | 58.4 |
| Interlaminar shear stress, $\bar{\tau}_{13}$ (MPa) | 52.1 | 65.5 |

**TABLE 3.4** Equivalent uniform stresses calculated at failure loads

## 3.7 Discussion

Use of Weibull theory has shown that the higher apparent strength of the long hoop specimens under combined interlaminar tension and shear compared with previous specimens subject to tension only is explained in terms of the smaller volume of material under stress. In this case the prediction ignoring the statistical effects would be conservative because the stressed volume of the hoop specimens is smaller than for the specimens used to measure interlaminar strengths. However, in cases with

large stressed volumes, where small specimens were used to determine allowable stresses, unconservative predictions would arise if the statistical effects were ignored.

When the stressed volume is accounted for, it is apparent that there is an interaction between the two stress components. It can be seen in figure 3.11 that for the two sets of experimental data, both the interlaminar shear and tensile stresses are less than the values which would be expected to cause failure acting alone. Use of the quadratic equation seems to be a reasonable way of accounting for this interaction, giving conservative predictions.

The interaction occurs because the interlaminar tensile and shear stresses arise at the same location. However, the approach of considering failure due to each stress component separately would imply interaction even if the maximum values occurred at different locations, and so might be over conservative. Some judgement is therefore necessary as to what is the appropriate volume over which to do the calculations. Taking the total volume of the part where failure is being considered seems to be a reasonable approach, although in larger structures there may be several areas of high stress which need to be considered separately, rather than performing a single calculation.

## 3.8 Conclusions

Finite element analysis of croquet-hoop-shaped specimens in three-point bending show that it is possible for specimens subject to combined interlaminar tension and shear to withstand higher stresses than when subject to interlaminar tension only. The reason for this is believed to be the size effect, which means that a high stress does not necessarily cause failure if the stressed volume is sufficiently small. When this effect is taken into account, it is seen that there is an interaction between interlaminar tension and shear, and a quadratic interaction equation gives a reasonable fit to the data. Experimental results for the two sets of hoop specimens were within 11% of the failure envelope proposed, and were conservative in both cases.

The results confirm the importance of accounting for the size effect in determining acceptable interlaminar stress levels. The statistical approach presented provides a reasonable way of predicting through-thickness failure based on the interlaminar stress distributions and experimental data for tensile and shear strengths. This approach is recommended for curved laminates without geometric discontinuities. The following chapter describes an analytical method for predicting delamination in laminates with geometric discontinuities.

# Chapter 4

# Parametric Study on Delamination in Laminates with Discontinuous Plies

## 4.1 Introduction

In the previous chapter we dealt with the problem of predicting through-thickness failure in curved laminates without ply discontinuities. In the rest of the thesis we will deal with predicting delamination initiating at ply terminations, starting with the problem of a straight laminate under a combination of axial loading and out-of-plane bending.

Stress based criteria have been used to predict delamination initiating at dropped plies [12] but a fracture mechanics approach is more useful in these situations. This is because very high stress gradients exist near the ends of discontinuous blocks which means the predicted failure load will be highly dependent on mesh size. Average or point stress criteria [18,20] can be used but they involve certain characteristic lengths which do not have a very strong theoretical foundation. The stress intensity factor can be used to predict delamination [68] but most authors use the strain energy release rate approach along with results from finite element analysis. The latter method has been used to predict delamination in a beam in four point bending with discontinuous internal plies [69], in beams with cut central plies under axial loading [70], from the end of a stringer bonded to a composite skin in

four point bending [23], and in tapered laminates under axial loading [71-76]. Good correlation was generally found with experimental data and it was seen that delamination could also be predicted in these cases from analytical solutions for determining the strain energy release rate, G, for stable crack propagation.

If closed form solutions exist for G, finite element analysis is not required and so time and energy can be saved. In [77] an analytical solution is derived for the strain energy release rate corresponding to a single delamination in a unidirectional beam in three-point bending. In [28] closed form solutions are derived for evaluating G for two delaminations in a beam in three-point bending and an end-notched flexure specimen. In [46] an equation was presented which gave the strain energy release rate due to edge delamination in terms of the loss of axial stiffness of the laminate. Davies and Robinson [56] derived a closed form solution for delamination in a flat circular plate under quasi-static impact loading. In [78] an analytical solution was used to obtain the strain energy release rates associated with delaminations spreading from a bimaterial notched four-point bending specimen. Excellent correlation was obtained with finite element analysis. Closed form solutions have also been derived for delamination propagation from transverse cracks in laminates under axial tension [51,79]. Lastly, Wisnom derived a closed form solution for cracks propagating between the continuous and discontinuous plies of a unidirectional beam under pure axial loading [72], and later for the case of pure bending [69].

In this chapter, an analytical solution for G is derived for cracks propagating between the continuous and discontinuous plies of a straight beam under both axial loading and out-of-plane bending. Such a solution has not been found in the current literature and it is a valuable tool in the preliminary design of tapered laminates. The equation is then used to show the effect of changing the ratio between bending and axial loading, changing the thickness of the block of discontinuous plies, and varying the position of the discontinuous block through the thickness. The solution assumes the discontinuous block, the continuous block above it, and the continuous block below it consist of three different materials. Therefore, the effect of having different combinations of ±45° blocks and 0° blocks in the laminate can be assessed. Finally, a

conservative failure envelope for delamination based on the axial strain at the discontinuous block of plies is presented.

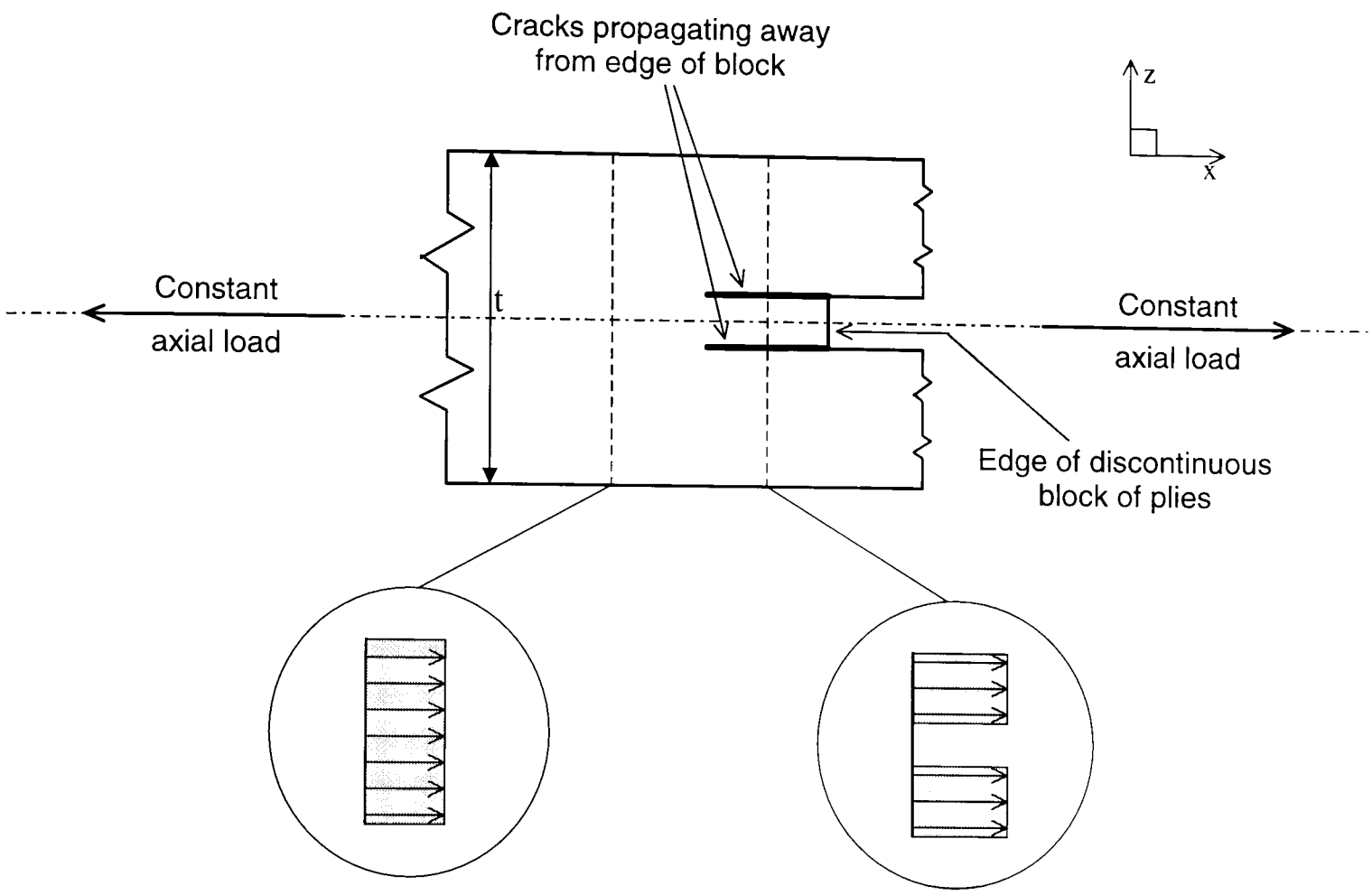


**FIG. 4.1** Delamination in a symmetrical laminate under pure tension showing axial strain distributions ahead and behind crack tips

## 4.2 Derivation of analytical solution for evaluating G

Refer to figure 4.1 for a schematic diagram of a homogeneous laminate with a discontinuous block of plies at its mid-thickness. A constant tensile load is being applied and cracks are propagating above and below the discontinuous block. Some distance ahead of the crack tips axial stresses are transferred into the discontinuous block from the surrounding continuous material by way of interlaminar shear stresses. So the discontinuous block contributes to supporting the applied load. However, some distance behind the crack tips, the central block is not contiguous with the surrounding plies. Thus, ignoring friction, the surrounding plies cannot transfer axial stresses into the discontinuous block. So the central block is

unburdened by the applied load and the surrounding material has to carry higher loads to make up for it. Therefore, the axial strain in the continuous material is higher behind the crack tips than ahead of them, and the axial strain in the discontinuous block is zero behind the crack tips, as seen in figure 4.1. The effect of the crack propagating by an increment, $\Delta a$, is to change the strain distribution in a volume of material, V, from the one in front of the crack tips to the one behind the crack tips, where,

$$V = t.w.\Delta a \tag{4.1}$$

and t and w are the thickness and width of the laminate, respectively. Note that the local stress field around the crack tip doesn't change and just moves with the crack.

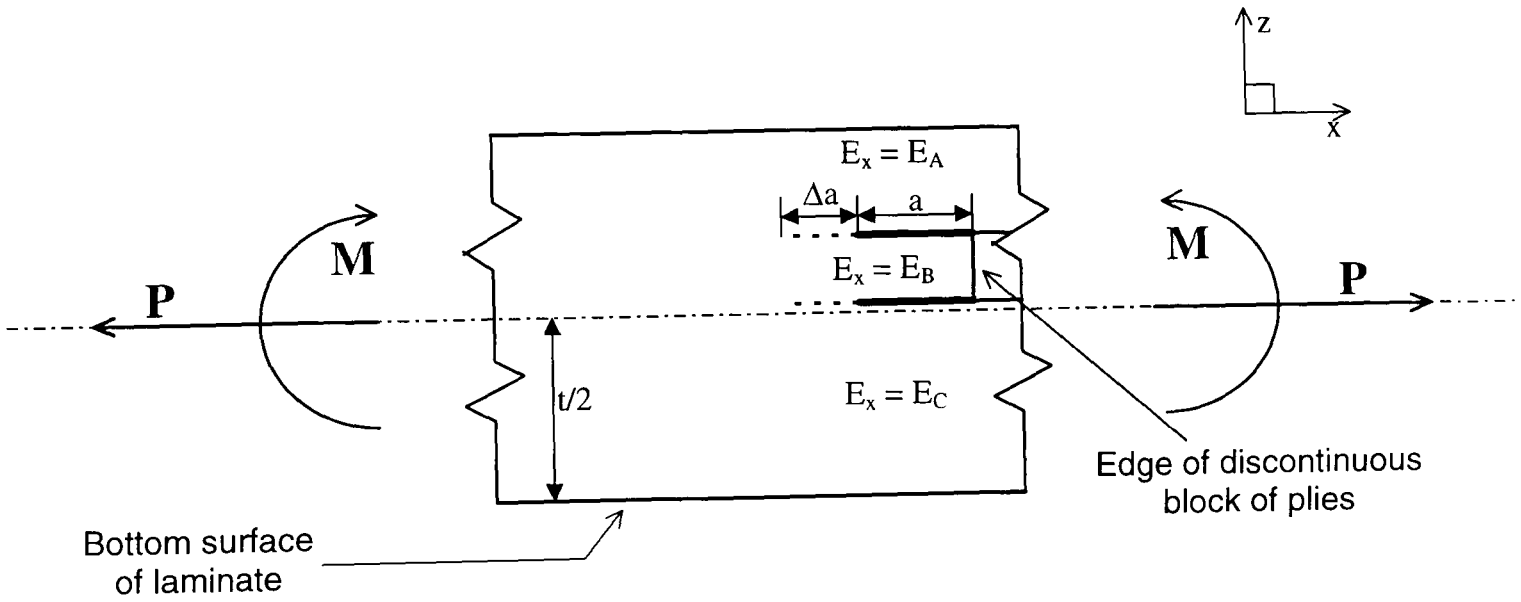


**FIG. 4.2** Delamination above and below a discontinuous block in a general laminate under a combination of bending and axial loading

Figure 4.2 shows a more general laminate which is under a combination of a bending moment, M, and an axial force, P, both per unit width. As in the previous example, cracks are propagating away from the end of a discontinuous block of plies along the interfaces with the surrounding continuous material. M and P are assumed to remain constant and act about and along the mid-thickness of the laminate. The laminate could either be tapered or another block of plies could be butted against the edge of

the discontinuous block. In the former case there would be some additional interlaminar stresses near the end of discontinuous block due to the geometry of the taper, but the effect on G has been shown not to be significant [71]. The strain energy release rate was calculated from finite element analysis for constant thickness specimens with cut central plies and tapered specimens with dropped central plies under pure axial loading. The cut-ply specimens were similar to the dropped-ply specimens except they were not tapered. The strain energy release rates for cracks propagating between the continuous and discontinuous plies reached the same constant value after the crack had propagated a short distance. Thus, the geometry of the taper did not affect G after a short initial propagation. The constant value which both strain energy release rates reached was identical to the value from an analytical solution which neglected taper effects. Failure load predictions using this constant value agreed well with experimental results. Therefore, delamination in tapered laminates can be predicted using an analytical solution for G which ignores the geometry of the taper. The following is an account of the derivation of such an analytical solution for the situation seen in figure 4.2.

When constant loads, M and P, are applied to the more general laminate, the effect of the crack length increasing by $\Delta a$ would be to change the strain distribution in a volume of material, V, from the one seen in figure 4.3a to the one in figure 4.3b[1]. This assumes there is a uniform strain gradient across contiguous plies, and plane transverse sections of the laminate remain plane after bending.

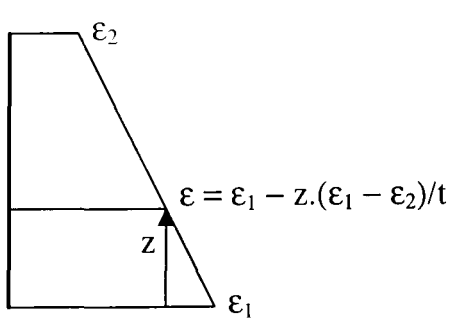


a). Before delamination

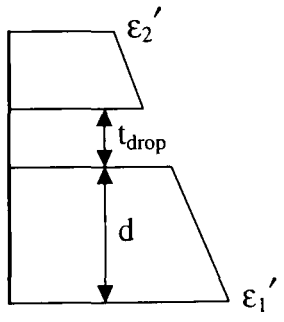


b). After delamination

**FIG 4.3** Axial strain distribution through thickness of laminate

[1] Note that the bending strain in the discontinuous block caused by the flexural deformation of the surrounding material has been ignored. However, the relative contribution of this strain to G would be small in all cases where G is high enough to cause delamination. Hence, the practical value of the following derived solutions and failure envelopes is not affected.

Let the distance from the bottom surface of the laminate be z, the axial strain at the bottom surface be $\varepsilon_1$ before crack propagation and $\varepsilon_1'$ after crack propagation, and the axial strain at the top surface be $\varepsilon_2$ before crack propagation and $\varepsilon_2'$ after crack propagation. The axial strains at z are therefore,

$$\varepsilon = \varepsilon_1 - z.(\varepsilon_1 - \varepsilon_2) / t \qquad \text{for} \quad 0 \le z \le t \qquad (4.2)$$

$$\varepsilon' = \varepsilon_1' - z.(\varepsilon_1' - \varepsilon_2') / t \qquad \text{for} \quad 0 \le z \le d \quad \text{and} \quad (d + t_{drop}) \le z \le t \qquad (4.3)$$

$$\varepsilon' = 0 \qquad \text{for} \quad d \le z \le (d + t_{drop}) \qquad (4.4)$$

where $\varepsilon$ is the axial strain before crack propagation and $\varepsilon'$ is the axial strain after, d is the distance of the discontinuous block from the bottom surface and $t_{drop}$ is the thickness of the discontinuous block.

We shall assume the laminate is made up of three homogeneous blocks of material. Let the axial Young's moduli be $E_A$ in the block above the discontinuous material, $E_B$ in the discontinuous block, and $E_C$ in the continuous block underneath. Let the three blocks have the same Poisson's ratio, $\nu_{xy}$, and coefficients of thermal expansion, $\alpha_x$ and $\alpha_y$. The effect of these assumptions is discussed later. The axial stresses, $\sigma$, before the cracks have propagated are therefore,

$$\sigma = E_A.[\varepsilon_1 - \zeta.(\varepsilon_1 - \varepsilon_2)] \qquad \text{for} \quad (\alpha + \beta) \le \zeta \le 1 \qquad (4.5)$$

$$\sigma = E_B.[\varepsilon_1 - \zeta.(\varepsilon_1 - \varepsilon_2)] \qquad \text{for} \quad \beta \le \zeta \le (\alpha + \beta) \qquad (4.6)$$

$$\sigma = E_C.[\varepsilon_1 - \zeta.(\varepsilon_1 - \varepsilon_2)] \qquad \text{for} \quad 0 \le \zeta \le \beta \qquad (4.7)$$

where $\zeta = z / t$, $\alpha = t_{drop} / t$, and $\beta = d / t$, and similarly, after crack propagation.

$$\sigma' = E_A.[\varepsilon_1' - \zeta.(\varepsilon_1' - \varepsilon_2')] \quad \text{for} \quad (\alpha + \beta) \leq \zeta \leq 1 \tag{4.8}$$

$$\sigma' = 0 \quad \text{for} \quad \beta \leq \zeta \leq (\alpha + \beta) \tag{4.9}$$

$$\sigma' = E_C.[\varepsilon_1' - \zeta.(\varepsilon_1' - \varepsilon_2')] \quad \text{for} \quad 0 \leq \zeta \leq \beta \tag{4.10}$$

Integrating the axial stresses throughout the cross-section of the laminate gives P:

$$P = t.\int_0^1 \sigma.d\zeta \tag{4.11}$$

The "hogging" bending moment (per unit width) about the bottom surface, $M_b$, can similarly be evaluated from,

$$M_b = t^2.\int_0^1 \sigma.\zeta.d\zeta \tag{4.12}$$

and the strain energy, U, in the volume of material defined in (4.1) is,

$$U = \tfrac{1}{2}.V.\int_0^1 \sigma.\varepsilon.d\zeta \tag{4.13}$$

The strain energy release rate, G, is defined as,

$$G = (\Delta W - \Delta U) / \Delta A \tag{4.14}$$

where $\Delta W$, $\Delta U$ and $\Delta A$ are the changes in external work, strain energy and crack surface area, respectively. For linear-elastic materials under constant loading,

$$\Delta W = 2.\Delta U \tag{4.15}$$

thus,

$$G = \Delta U / \Delta A \tag{4.16}$$

Finally, since the change in crack area due to cracks propagating above and below the discontinuous block, is $2.\Delta a.w$, the strain energy release rate is equal to:

$$G = \frac{U_{after} - U_{before}}{2.\Delta a.w} \tag{4.17}$$

where $U_{after}$ is the strain energy after the crack has propagated and $U_{before}$ is the strain energy before. We wish to have an expression for G in terms of P and M. Hence, if (4.5) to (4.7) are substituted into (4.11) and (4.12) the following expressions are obtained:

$$B.\varepsilon_1 - C.(\varepsilon_1 - \varepsilon_2) = P / t \tag{4.18}$$

$$C.\varepsilon_1 - D.(\varepsilon_1 - \varepsilon_2) = M_b / t^2 \tag{4.19}$$

where,

$$B = E_C.\beta + E_B.\alpha + E_A.(1 - \beta - \alpha) \tag{4.20}$$

$$C = E_C.\beta^2 / 2 + E_B.(\alpha.\beta + \alpha^2 / 2) + E_A.[1 - (\beta + \alpha)^2] / 2 \tag{4.21}$$

$$D = E_C.\beta^3 / 3 + E_B.(\alpha.\beta^2 + \beta.\alpha^2 + \alpha^3 / 3) + E_A.[1 - (\beta + \alpha)^3] / 3 \tag{4.22}$$

Equations (4.18) and (4.19) are simultaneous equations which can be solved to give $\varepsilon_1$ and $(\varepsilon_1 - \varepsilon_2)$ in terms of P, $M_b$, $\alpha$, $\beta$, and the Young's moduli. By substituting (4.8) to (4.10) into (4.11) and (4.12), $\varepsilon_1'$ and $(\varepsilon_1' - \varepsilon_2')$ can similarly be found in terms of these variables.

We now need to find expressions for $U_{after}$ and $U_{before}$ in terms of P, $M_b$, $\alpha$, $\beta$, and the Young's moduli. When (4.1), (4.2) and (4.5) to (4.7) are substituted into (4.13),

$U_{before}$ can be obtained in terms of $\varepsilon_1$ and $\varepsilon_2$, and hence, in terms of P, $M_b$, $\alpha$, $\beta$, and the Young's moduli. Similarly, when (4.1), (4.3), (4.4), and (4.8) to (4.10) are substituted into (4.13), $U_{after}$ can be found in terms of $\varepsilon_1'$ and $\varepsilon_2'$, and hence, in terms of P, $M_b$, $\alpha$, $\beta$, and the Young's moduli. The following expression can then be used to give $U_{after}$ and $U_{before}$ in terms of M instead of $M_b$:

$$M_b = P.t / 2 - M \tag{4.23}$$

Note that M is a "sagging" bending moment, as seen in figure 4.2. Finally, by substituting the expressions for $U_{after}$ and $U_{before}$ into (4.17) we can obtain an expression for G in terms of P, M, $\alpha$, $\beta$, and the Young's moduli.

After algebraic simplification the following equation was obtained:

$$G = \frac{3M^2}{E_A t^3}\left[\frac{c_1}{4c_1c_3 - 3c_2^2} - \frac{c_4}{4c_4c_6 - 3c_5^2}\right] + \frac{3PM}{E_A t^2}\left[\frac{c_2 - c_1}{4c_1c_3 - 3c_2^2} - \frac{c_5 - c_4}{4c_4c_6 - 3c_5^2}\right] + \frac{P^2}{4E_A t}\left[\frac{4c_3 - 6c_2 + 3c_1}{4c_1c_3 - 3c_2^2} - \frac{4c_6 - 6c_5 + 3c_4}{4c_4c_6 - 3c_5^2}\right] \tag{4.24}$$

where,

$$c_1 = 1 - (\alpha + \beta) + k.\beta \tag{4.25}$$

$$c_2 = 1 - (\alpha + \beta)^2 + k.\beta^2 \tag{4.26}$$

$$c_3 = 1 - (\alpha + \beta)^3 + k.\beta^3 \tag{4.27}$$

$$c_4 = 1 - \alpha - \beta + j.\alpha + k.\beta \tag{4.28}$$

$$c_5 = 1 + (\alpha + \beta)^2.(j - 1) + \beta^2.(k - j) \tag{4.29}$$

$$c_6 = 1 + (\alpha + \beta)^3.(j - 1) + \beta^3.(k - j) \tag{4.30}$$

and,

$$j = E_B/E_A \tag{4.31}$$

$$k = E_C/E_A \tag{4.32}$$

Furthermore, if j = k = 1, i.e. the laminate is unidirectional, (4.24) simplifies to:

$$G = \frac{3M^2}{E_x t^3}\left[\frac{(1-\alpha)}{(1-\alpha)^4 + 12\alpha\beta(1-\alpha-\beta)} - 1\right] + \frac{3MP}{E_x t^2}\left[\frac{\alpha(1-\alpha-2\beta)}{(1-\alpha)^4 + 12\alpha\beta(1-\alpha-\beta)}\right] + \frac{P^2}{4E_x t}\left[\frac{\alpha(1-\alpha^3)}{(1-\alpha)^4 + 12\alpha\beta(1-\alpha-\beta)}\right] \tag{4.33}$$

where $E_x$ is the axial Young's modulus. When M = 0 and the discontinuous block is located in the mid-thickness of the laminate, (4.33) reduces to the analytical solutions given in [72,79], and (4.24) simplifies to the one in [51] without thermal residual stresses. Similarly when P = 0, (4.33) reduces to the expression given in [69] for the strain energy release rate in a unidirectional beam under pure bending with cut central plies.

The strain energy release rate from (4.24) for a non-symmetric laminate under a combination of bending and axial load was verified with finite element analysis using shell elements. The laminate was modelled as a flat plate consisting of three layers of material with different axial Young's moduli. The Young's modulus of the middle block was then assigned to zero to model a completely delaminated laminate. The strain energy release rate was found from the difference in strain energy between the original and delaminated models. The value of G was almost identical to the one from (4.24).

The expressions in (4.24) and (4.33) can also be used to calculate G for a laminate with a discontinuous block on the surface ($\beta + \alpha = 1$ or $\beta = 0$). However, since the change in crack surface area is half that of when the discontinuous block is embedded, the value of G from the analytical solution must be doubled. Finally, when more than one block of plies is dropped in a laminate without interleaving continuous plies, some engineering judgement is required. If the ends of the discontinuous blocks are close enough together they may interact and therefore should be counted as one single discontinuous block [80].

## 4.3 Influence of axial stiffness and ratio of bending to axial loading

The analytical solution was used to examine the variation of G with the change in ratio between axial loading and bending moment for a number of different laminates. Several simple laminates were chosen solely for the purpose of studying the effect of having discontinuous plies with different Young's moduli to the surrounding material. The magnitude of the axial strain at the more highly strained surface of each laminate was kept at 1% throughout the whole range of loading conditions. The lay-ups were:

| | |
|---|---|
| $(0°_{22} / \underline{0°}_4 / 0°_6)$ | E glass / 913 epoxy |
| $(0°_{22} / (\underline{45°/-45°})_2 / 0°_6)$ | E glass / 913 epoxy |
| $((45°/-45°)_{11} / \underline{0°}_4 / (45°/-45°)_3)$ | E glass / 913 epoxy |
| $((45°/-45°)_{11} / (\underline{45°/-45°})_2 / (45°/-45°)_3)$ | E glass / 913 epoxy |
| $(0°_{22} / \underline{0°}_4 / 0°_6)$ | XAS carbon / 913 epoxy |

where the plies are given in order from the bottom of the laminate to the top, and the discontinuous plies are underlined. Note that the laminates are all 32 plies thick, and the positions and thicknesses of the discontinuous plies were kept constant. Each of the three "sublaminates" which made up the laminate were assumed to be homogeneous. The value of the axial Young's modulus, $E_x$, for each type of sublaminate is given in table 4.1, and the thickness of each ply was assumed to be 0.125mm. The axial Young's modulus of the ±45° glass sublaminates was taken as the equivalent membrane elastic modulus found from laminated plate theory. Linear-elastic material behaviour was assumed throughout the study.

| | 0° E Glass/ 913 Epoxy | ±45° E Glass/ 913 Epoxy | 0° XAS Carbon/ 913 Epoxy |
|---|---|---|---|
| $E_x$ | 43.9 GPa | 13.9 GPa | 138 GPa |
| In-plane failure strain (tension) | 2.78% | 2% | 1.66% |
| In-plane failure strain (compression) | -2.53% | -2% | -1.66% |
| $G_c$ (axial tension) | 1.08 N/mm | 1.08 N/mm | 0.82 N/mm |
| $G_c$ (axial compression) | 0.54 N/mm | 0.54 N/mm | 0.32 N/mm |

**TABLE 4.1** Material properties of sublaminates

In multidirectional laminates there can be additional stresses due to the Poisson's ratio mismatch, and thermal and moisture effects. Therefore, a check was carried out to see if the relatively different values of Poisson's ratio, $\nu_{xy}$, in the 0° and ±45° glass sublaminates had a significant effect on the strain energy release rate. In practice, thermal residual stresses reduce with time due to creep and may also be reduced by moisture absorption. However, as a first approximation, the thermal residual stresses were taken into account based purely on the coefficients of thermal expansion, $\alpha_x$ and $\alpha_y$, and the difference between the cure temperature and room temperature. Coefficients of thermal expansion vary throughout the temperature drop but for simplicity they were assumed to remain constant when calculating the stresses.

G was calculated for a $(0°_{14}$ / $\underline{-45° / 45°})_s$ and $((45°/-45°)_7$ / $\underline{0°_2})_s$ laminate in pure tension, using the strains and stresses from laminated plate theory and the material properties in table 4.2. The values calculated from the analytical solution (which assumes constant values of $\nu_{xy}$, $\alpha_x$ and $\alpha_y$ throughout the thickness) were both within 20% of the values from laminated plate theory (which took these effects into account). The effect on predicted failure stress or strain would therefore be within 10%. This is an extreme case due to the large differences in properties between 0° and ±45° plies. In more practical lay-ups the effect would be much less, and the equation should be sufficiently accurate to be able to determine the general trends in G with respect to the different parameters studied in this chapter, and for use in initial design calculations.

| | |
|---|---|
| Fibre direction Young's modulus, $E_1$ | 43.9 GPa |
| Young's modulus transverse to fibres, $E_2$ | 15.4 GPa |
| Poisson's ratio, $\nu_{12}$ | 0.3 |
| Coefficient of thermal expansion in fibre direction, $\alpha_1$ | $6.6 \times 10^{-6}$ / °C |
| Coefficient of thermal expansion transverse to fibres, $\alpha_2$ | $30 \times 10^{-6}$ / °C |
| Curing Temperature | 125 °C |
| Laboratory Temperature | 20 °C |

**TABLE 4.2** Material properties of E glass / 913 epoxy for laminated plate theory

The following ratio was used to gauge the relative contributions of applied bending deformation and applied axial deformation:

$$R = \frac{\varepsilon_b}{|\varepsilon_a| + |\varepsilon_b|} \tag{4.34}$$

where $\varepsilon_a$ is the axial strain, equal to $(\varepsilon_1 + \varepsilon_2) / 2$, and $\varepsilon_b$ is the bending strain, equal to $(\varepsilon_1 - \varepsilon_2) / 2$. Thus, when R = 1 the laminate is under pure bending (and M is positive), when R = 0 the laminate is under pure axial deformation, and when R = -1 the

laminate is under pure bending (and M is negative). For each value of R there exist two loading conditions; one corresponding to axial tension, and one to axial compression. G was calculated for a range of values of R for each of the laminates, and the curves plotted on the graph given in figure 4.4. Note that only the curves corresponding to axial tension are given for clarity. The curves corresponding to axial compression are identical except they are reflected across the R = 0 axis.

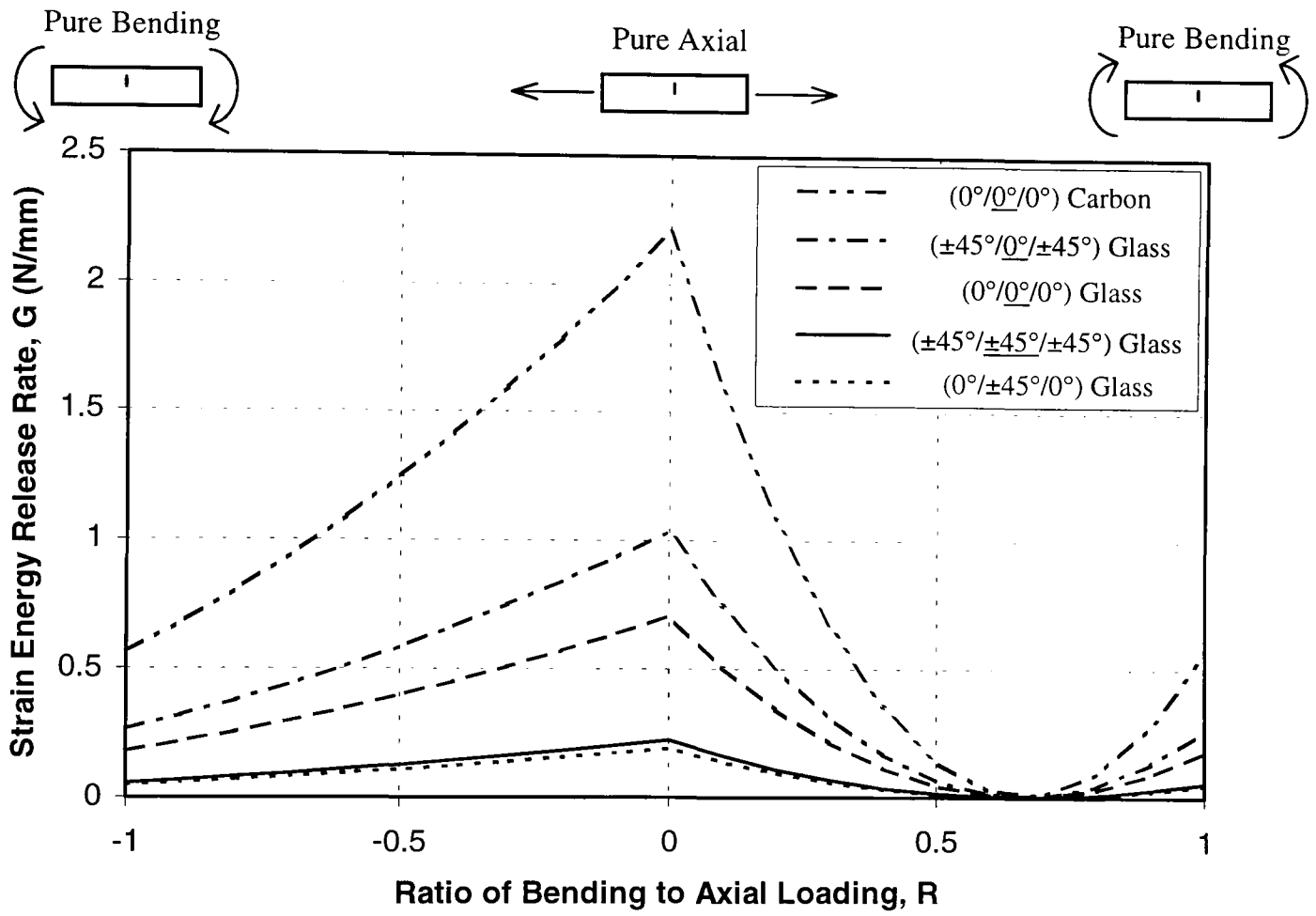


**FIG. 4.4** Variation of G with respect to ratio between bending and axial deformation for various types of laminates with same number & position of discontinuous plies. (Magnitude of strain at more highly strained surface kept at 1%)

One can see that the shape of each curve is similar for every laminate. The strain energy release rate is higher under pure axial deformation than pure bending deformation. At the same time, the strain in the discontinuous block is higher under pure axial deformation compared to pure bending deformation. Similarly, G is very low under some combinations of bending and axial loading where the resultant strain in the discontinuous block is also very low. This means the strain at the mid-

thickness of the discontinuous block, $\varepsilon_d$, could be an important parameter for predicting G.

Comparing the curves for each of the "homogeneous" laminates (unidirectional glass and carbon, and pure ±45° glass) one can notice the increase in G with increase in stiffness. In fact, G is proportional to $E_x$ according to the analytical solution, when the strain is kept constant. It can also be seen that the curves for the glass ($0°_{22}$ / $\underline{0°}_4$ / $0°_6$) and (($45°/-45°)_{11}$ / $\underline{0°}_4$ / $(45°/-45°)_3$) laminates lie close together, as do the curves for the ($0°_{22}$ / $(\underline{45°/-45°})_2$ / $0°_6$) and (($45°/-45°)_{11}$ / $(\underline{45°/-45°})_2$ / $(45°/-45°)_3$) laminates. G is therefore more dependent on the stiffness of the discontinuous block than of the surrounding material. The change in stiffness of the laminate depends entirely upon the stiffness of the discontinuous plies. The relationship implied by O'Brien's closed form solution for edge delamination [46] is that the strain energy release rate is proportional to the change in stiffness of the laminate due to delamination. Thus, the relationship between G and the change in stiffness for the case studied in this chapter is similar to the one corresponding to edge delamination.

Finally, it is interesting to compare laminates with the same block of discontinuous plies. One will notice that a stiffer surrounding material results in lower values of G, even though higher values of M and P have to be applied to maintain the condition of 1% strain at the surface. The absolute change in stiffness of the laminate due to delamination is constant when the block of discontinuous plies remains the same. However, the ratio between the stiffness before delamination, $K_{before}$, and the stiffness after delamination, $K_{after}$, is lower when the continuous plies are stiffer. Therefore, G is related to the ratio, $K_{before}$ / $K_{after}$. In [81] a range of different dropped-ply laminates were tested in axial compression. Failure was due to delamination. It was found that as the ratio of the stiffness of the thick section over the stiffness of the thin section increased, the strength of the laminates decreased. The stiffness of the thick section is equivalent to $K_{before}$ and the stiffness of the thin section is equivalent to $K_{after}$. Thus, assuming the strength of the laminate is inversely related to G, the results in [81] can be explained by the relationship given above.

The above observed patterns led to the idea of normalising the results by plotting $G / (\varepsilon_d^2.E_B.t)$ against R for different ratios of $E_x$ of the discontinuous plies over $E_x$ of the surrounding material. In this case, the latter ratio is equal to j, i.e. $E_B/E_A$, since $E_A = E_C$. Also note that, from (4.24) it can be deduced that G would be proportional to the thickness of the laminate, t, when the loading is expressed in terms of strain. Hence, at a particular value of j, the values of $G / (E_B.t)$, $\varepsilon_a$ and $\varepsilon_b$ were found for a wide range of values of M and P. The values of R and $\varepsilon_d$ could then be found from $\varepsilon_a$ and $\varepsilon_b$. Thus, the "normalised" strain energy release rate, $G / (\varepsilon_d^2.E_B.t)$, could be plotted against R. The graph is given in figure 4.5. As in figure 4.4, only the curves corresponding to axial tension are given since the curves for axial compression are identical except they are reflected across the R = 0 axis. The three curves correspond to j = 1, for all the "homogeneous" lay-ups, j = 0.318, for the $(0°_{22} / (\underline{45°/-45°})_2 / 0°_6)$ laminate, and j = 3.149, for the $((45°/-45°)_{11} / \underline{0°}_4 / (45°/-45°)_3)$ laminate.

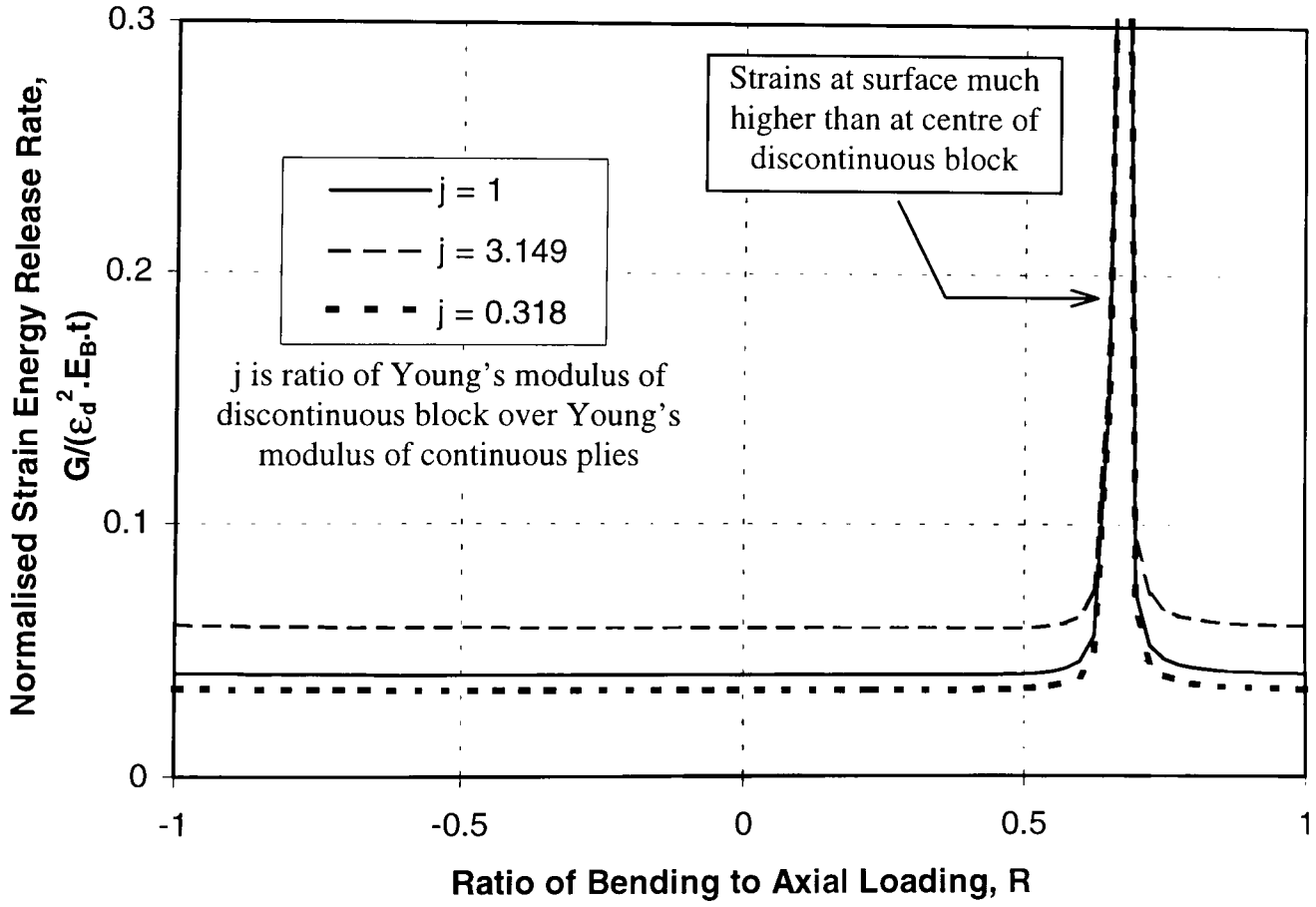


**FIG. 4.5** Virtual independence of normalised G from loading conditions

An interesting conclusion can be drawn from the figure. One will notice that the variation of G is very low for a wide range of loading conditions when $\varepsilon_d$, $E_B$ and t are kept constant. The value of $G / (\varepsilon_d^2.E_B.t)$ only deviates from the almost constant value when the applied axial force and bending moment induce strains at the discontinuous block of opposite signs and similar magnitudes. This results in values of $\varepsilon_a$ and $\varepsilon_b$ much higher than $\varepsilon_d$. In practice, in-plane failure would occur before delamination in most composite laminates under such loading conditions due to the high strains at the surface. Thus, for a particular number and position of discontinuous plies, a practical value of G could be determined reasonably accurately for a general laminate just from the values of $\varepsilon_d$, $E_B$, t and j.

The relatively low increase in strain energy release rate with increase in j can clearly be seen. Furthermore, at a particular value of R, the relationship between j and $G / (\varepsilon_d^2.E_B.t)$ was found to be linear. This can be explained by the relationship between G and $(K_{before} / K_{after})$ mentioned above. If, for simplicity, we consider a symmetrical laminate under pure axial loading,

$$K_{before} = [E_A.(1 - \alpha - \beta) + E_B.\alpha + E_C.\beta].t \tag{4.35}$$

and,

$$K_{after} = [E_A.(1 - \alpha - \beta) + E_C.\beta].t \tag{4.36}$$

and since $j = E_B / E_A$ and $E_A = E_C$,

$$G \propto [1 + j.\alpha/(1 - \alpha)] \tag{4.37}$$

which shows G is linearly related to j when both the applied strain and the change in stiffness remain constant. The change in stiffness is proportional to $E_B$, so the value of $G / (\varepsilon_d^2.E_B.t)$ should be linearly related to j.

## 4.4 Influence of thickness and position of discontinuous block

To investigate the effects of varying the number and position of discontinuous plies. G was evaluated for several unidirectional glass laminates. The total number of plies was kept constant but the number of discontinuous plies and their position in the thickness direction was varied. A graph of G against the ratio between bending and axial loading, R, can be seen in figure 4.6. As before, only the curves corresponding to axial tension are given, and the strain at the surface was kept at 1%.

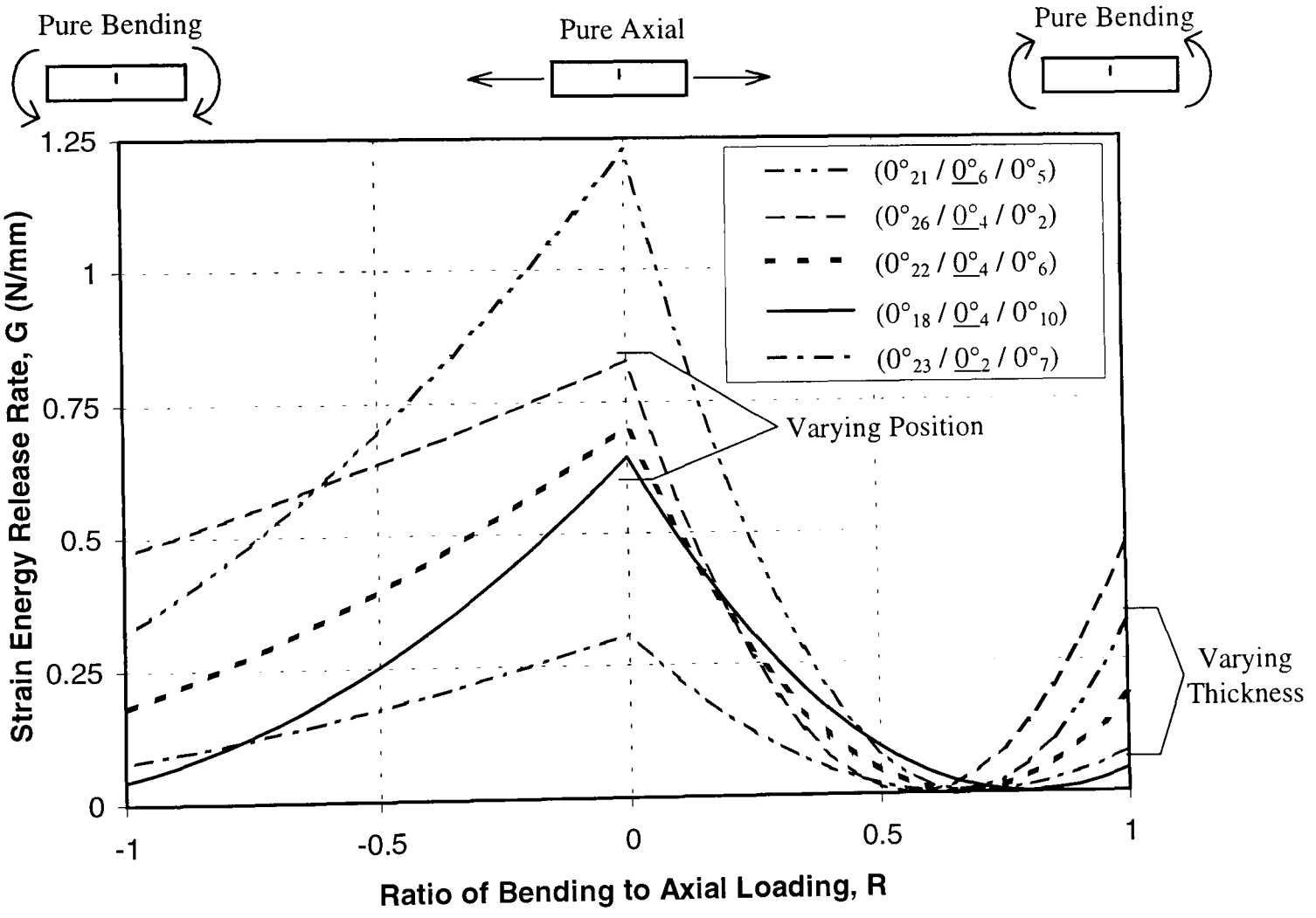


**FIG. 4.6** Variation of G with respect to ratio between bending and axial loading for U-D glass laminates with various numbers & positions of discontinuous plies (Magnitude of strain at more highly strained surface kept at 1%)

The influence of the relative thickness of the discontinuous block can be seen by comparing the three curves corresponding to the $(0°_{21} / \underline{0°}_6 / 0°_5)$, $(0°_{22} / \underline{0°}_4 / 0°_6)$ and $(0°_{23} / \underline{0°}_2 / 0°_7)$ lay-ups. Note that the mid-thicknesses of the discontinuous

blocks all lie exactly 1mm from the mid-thicknesses of the laminates. Thus the value of the axial strain at the mid-thickness of the discontinuous block, $\varepsilon_d$, remains constant and there is no change in the effective position of the block. As would be expected, the thicker the block of discontinuous plies the higher the value of G, since the greater the change in stiffness.

The effect of the position of the discontinuous block can be seen by comparing the curves corresponding to the $(0°_{18} / \underline{0°}_4 / 0°_{10})$, $(0°_{22} / \underline{0°}_4 / 0°_6)$ and $(0°_{26} / \underline{0°}_4 / 0°_2)$ lay-ups. If we first look at the pure bending cases (R = ±1) we will notice G is higher when the discontinuous block is closer to the surface. This is to be expected since the change in bending stiffness is greater when the discontinuous block is further from the centre. Also, for a constant value of strain at the surface the value of $\varepsilon_d$ will be higher when the block is closer to the surface, and as mentioned in the previous section, G is related to $\varepsilon_d$. What is not so obvious is the increase in G with distance from the laminate mid-thickness when only axial strain is applied (R = 0). Although there is no bending before delamination, when the discontinuous block is not at the centre of the laminate there is some bending after delamination due to non-symmetry. So the change in bending stiffness is still important when R = 0, and higher values of G would be expected when the discontinuous plies are further from the mid-thickness of the laminate. However, this effect is much lower under pure axial loading, so the variation in G is higher for R = ±1 compared to R = 0.

As an attempt to show all the above trends, a graph of the normalised strain energy release rate, $G / (\varepsilon_d^2.E_B.t)$, against the non-dimensional thickness of the discontinuous block, $\alpha$, was plotted. This was done for three values of j (the ratio between the Young's modulus of the discontinuous block over that of the continuous material above). Furthermore, for each value of j there are three positions of the discontinuous block, described by $\beta$, the non-dimensional distance of the discontinuous block from the bottom surface. This was done for the pure axial loading case (M = 0), and the graph is given in figure 4.7. As can be seen from figure 4.5, the value of normalised G is very similar for almost any value of R and so the plot in figure 4.7 would be virtually identical for pure bending , and most combinations of bending and axial loading. From figure 4.7 one should therefore be able to get a reasonable

approximation of the strain energy release rate for any laminate based on the value of the axial strain at the mid-thickness of the discontinuous block, $\varepsilon_d$. Note that only values of $\beta$ greater or equal to 0.5 have been shown since the value of $G / (\varepsilon_d^2.E_B.t)$ for $\beta = n$ (where $0 < n < 1$) is equal to the value corresponding to $\beta = (1 - \alpha - n)$ with the opposite sign of M. It can be seen that the higher the values of j, $\alpha$ and $\beta$, the higher the value of $G / (\varepsilon_d^2.E_B.t)$. Furthermore, the effect of $\beta$ becomes more pronounced at higher values of j and $\alpha$. For $\alpha \leq 0.05$ and for $j \leq 0.2$ the effect of $\beta$ is negligible. The effect of j also becomes more pronounced at higher values of $\alpha$. It was found that for $\alpha \geq 0.25$ the independence of normalised G with respect to the ratio between bending and axial loading, R, started to break down as well. However, it is very uncommon to have a single block of dropped plies of thickness greater than a quarter the thickness of the whole laminate in a load bearing composite structure.

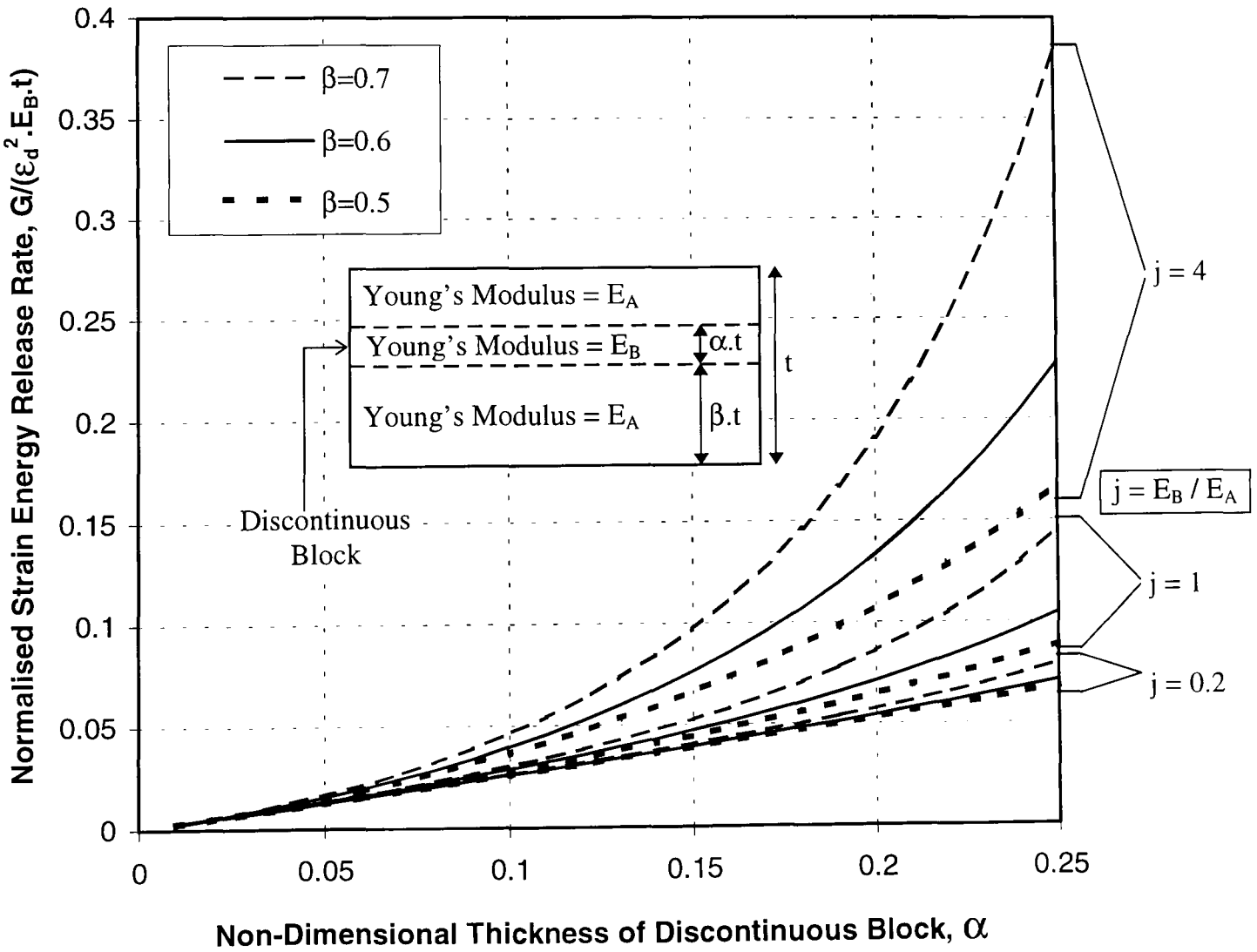


**FIG. 4.7** Master plots for strain energy release rate

## 4.5 Failure envelope based on allowable values of strain at the discontinuous block

The results of the parametric study paved the way for developing a simple and conservative method for predicting delamination. For a laminate of a given material (or combination of materials) one should be able to obtain the safe limits of the axial strain at the discontinuous block, $\varepsilon_d$, for any thickness and position of the discontinuous block from a single graph. Furthermore, certain simple design rules could be obtained, such as the maximum number of plies that can be dropped together for no delamination to occur under any loading condition. This would enable a design engineer to ensure delamination will not take place in a composite structure without the need for detailed finite element analysis, fracture mechanics calculations or extensive testing. Note that in this study we are only concerned with delamination above and below a discontinuous block of plies. Delamination can also propagate into the thin section of a tapered laminate if the geometric discontinuity is too severe, but this can generally be avoided by keeping the taper angle low. In previous tests no thin section delamination was observed with angles up to 12° [74].

As an initial example, a failure envelope was constructed for unidirectional E glass / 913 epoxy laminates. The assumed values of in-plane failure strain and the critical strain energy release rate, $G_c$ are given in table 4.1. Note that there are two values of the critical strain energy release rate. They were calculated from tests done on straight unidirectional laminates with two cut central plies and eight surrounding continuous plies [70]. The value of $G_c$ for axial tension was calculated from the axial tensile load at which delamination occurred between the cut plies and the continuous plies. This corresponds to pure mode II delamination. Similarly, the value of $G_c$ for axial compression comes from the axial compression load at which delamination occurred. In this case, as well as mode II, there is also mode I due to the through-thickness tensile stresses near the crack tips. The value of the mixed mode $G_c$ corresponding to compression is therefore lower. In practice this value may vary due to differences in the mode ratio but the value chosen is considered to be reasonably representative. It should also be noted that if the discontinuous plies are on the

surface, the situation is reversed, and axial tensile loading will produce mixed mode delamination, and compression will give pure mode II.

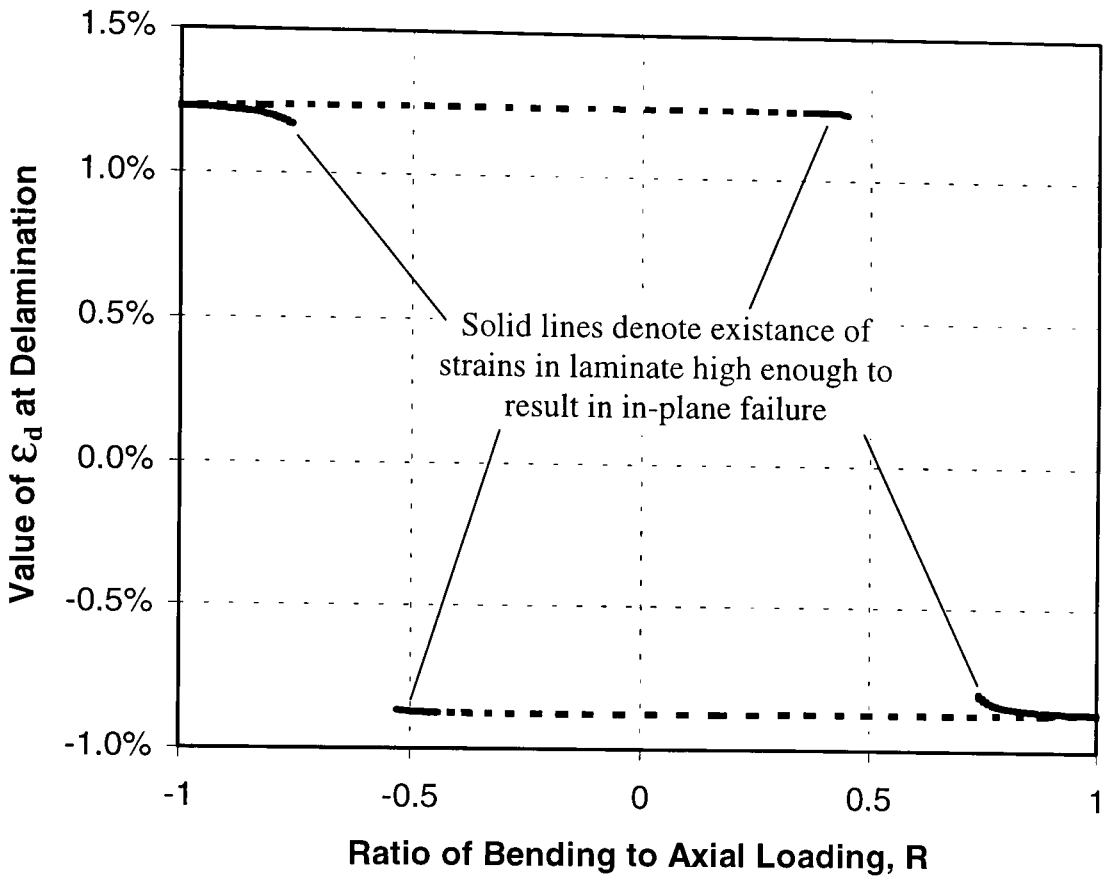


**FIG. 4.8** Axial strain at mid-thickness of discontinuous block at delamination for range of loading conditions

Values of the axial strain at the mid-thickness of the discontinuous block at delamination were calculated for a $(0°_{22} / \underline{0°}_4 / 0°_6)$ laminate at a range of loading conditions. The loading conditions were calculated to produce $G = G_c$ (compression) when the value of $\varepsilon_d$ was negative, and $G = G_c$ (tension) when $\varepsilon_d$ was positive. At the same time, the axial strains throughout the laminate were checked to see if in-plane failure would occur. The results can be seen in the graph of $\varepsilon_d$ against R, in figure 4.8. The solid lines signify in-plane failure would occur under the loading conditions. The main observation one can make from the graph is that the value of $\varepsilon_d$ at which delamination takes place is virtually independent of the ratio of bending to axial loading. Whenever the curves deviate from the virtually constant value, in-plane failure would occur before delamination. Notice also that the magnitude of the negative axial strain at delamination is lower than the corresponding positive (tensile)

value. This is because the $G_c$ value for compression is lower. There are sometimes two values of $\varepsilon_d$ at delamination of the same sign corresponding to the same value of R. This is because, for any value of R the axial force can either be tensile or compressive.

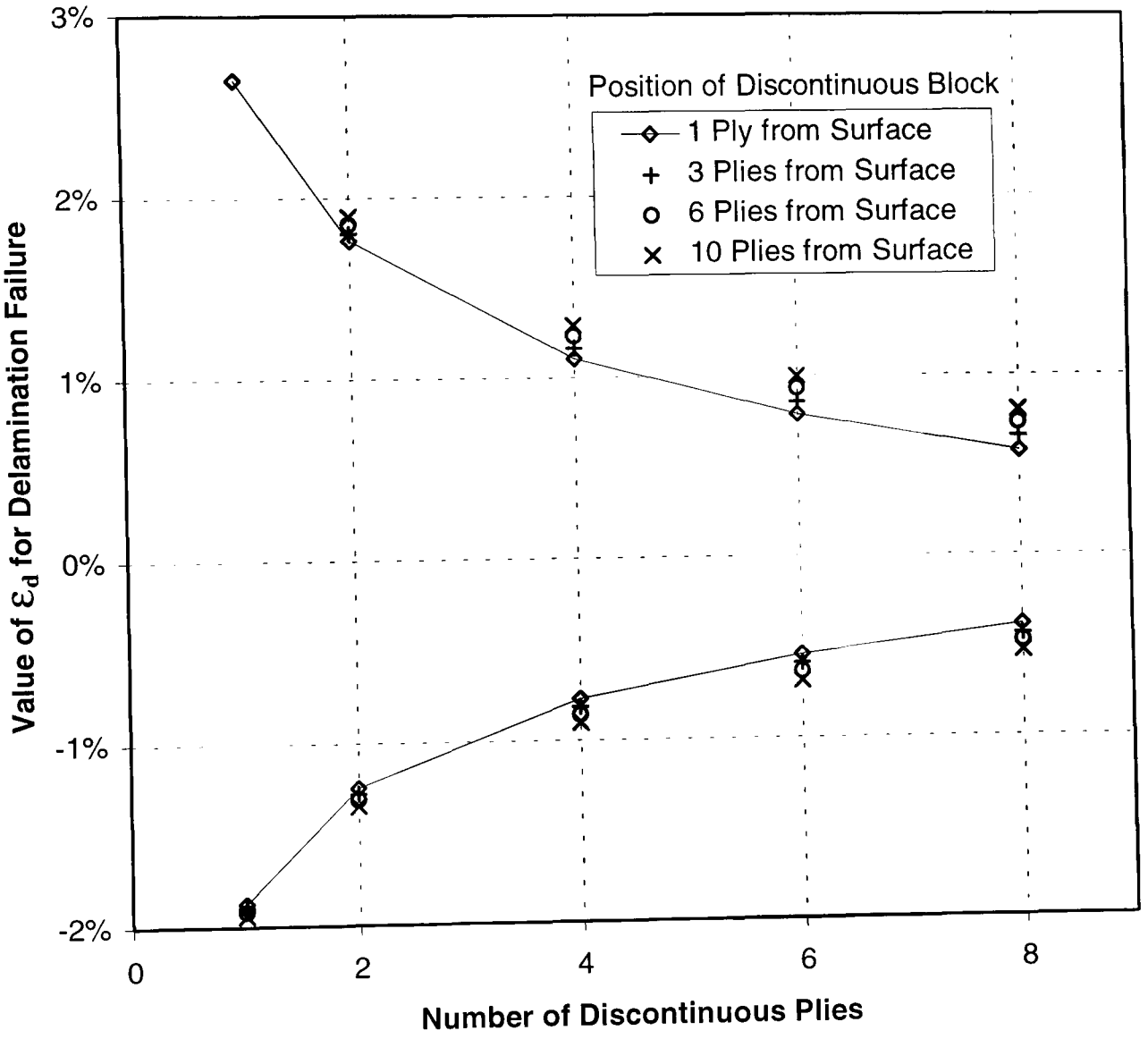


**FIG. 4.9** Failure envelope for 32-ply unidirectional glass laminates

To construct a failure envelope we need to obtain the values of $\varepsilon_d$ at delamination failure from the graph. We ignore the solid regions of the curves as these correspond to in-plane failure. The dashed portions of the curves are almost horizontal but the values of $\varepsilon_d$ do vary by a very small amount. Therefore, to get conservative limits of $\varepsilon_d$ for delamination, the lowest positive value and the highest negative value of $\varepsilon_d$ were used. The same technique was used to obtain conservative limits of $\varepsilon_d$ for delamination for unidirectional laminates with various numbers and positions of

discontinuous plies. The difference between the maximum and minimum values of $\varepsilon_d$ (of the same sign), not including-in-plane failure cases, was always less than 5%, except when the discontinuous block was 8 plies thick. And even in this extreme case the difference was always less than 15%. In other words, it was still reasonably accurate to use conservative values of $\varepsilon_d$, and ignore the ratio between M and P. The results can be seen on a single graph, in figure 4.9.

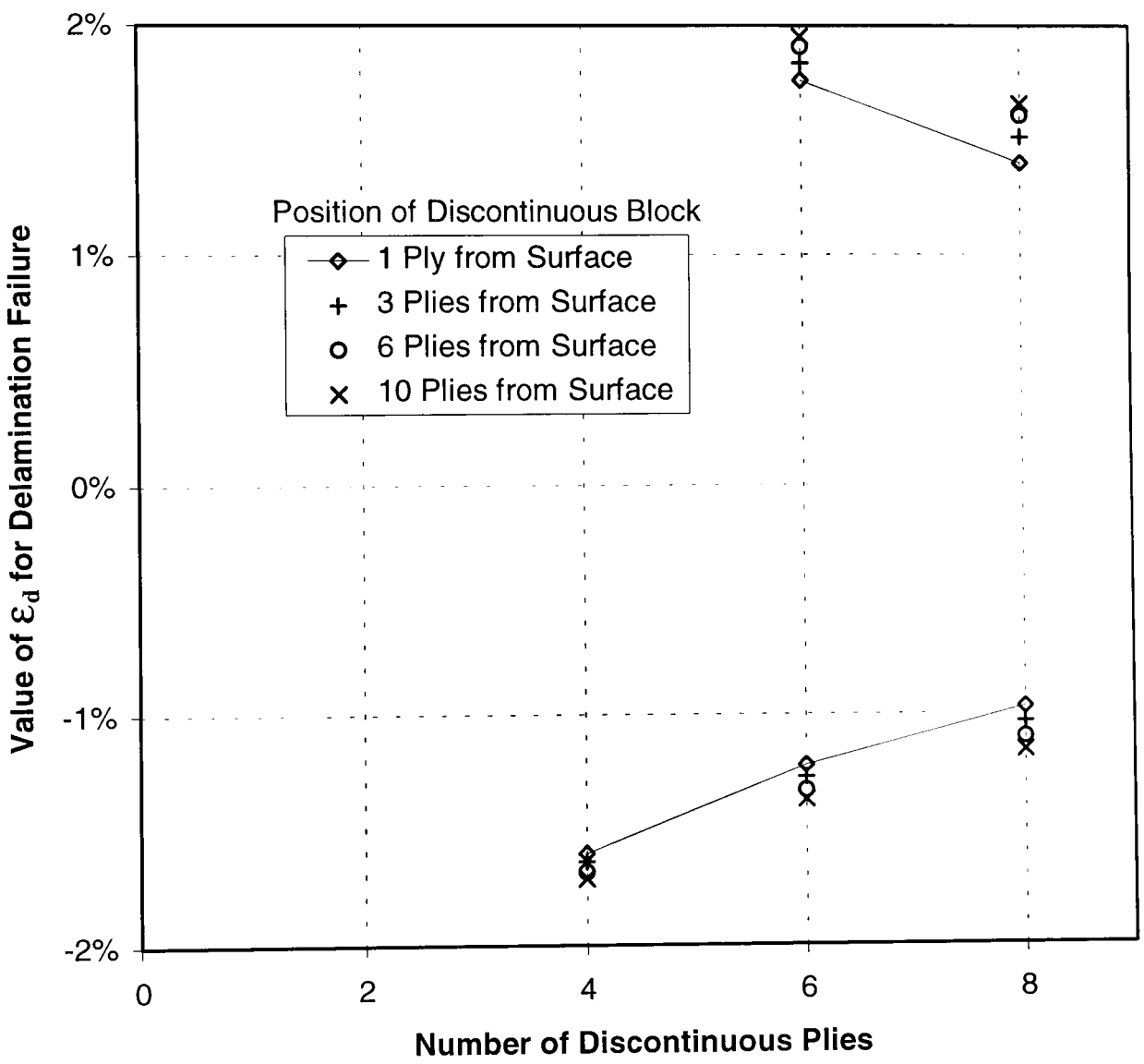


**FIG. 4.10** Failure envelope for 32-ply ($0°_x$ / $\pm\underline{45°}_x$ / $0°_x$) glass laminates

One can clearly see that the safe limits of $\varepsilon_d$ reduce as the number of plies in the discontinuous block increases. The limits also reduce when the discontinuous block is situated closer to the surface. However, the effect is quite small when less than six plies are discontinued. For convenience the line connecting the data points corresponding to the block one ply from surface could be used as a conservative

failure envelope for any position of discontinuous block. One may also notice that when there is only one discontinuous ply in axial tension there is only one data point. This is because in-plane failure always occurred before delamination when the block was in any position except one ply from the surface.

Similar graphs, seen in figures 4.10 to 4.13, were constructed for ($0°_x$ / $\underline{\pm 45°}_x$ / $0°_x$), ($\pm 45°_x$ / $\underline{0°}_x$ / $\pm 45°_x$), and pure ±45° glass laminates, and unidirectional XAS carbon / 913 epoxy laminates. Again, the material properties are given in table 4.1. Axial in-plane strain limits of ±2% were assumed for ±45° glass. These values were not intended to represent the failure strains but merely practical safe limits of the material. In any case, the values of $\varepsilon_d$ for the failure envelopes were not very sensitive to them.

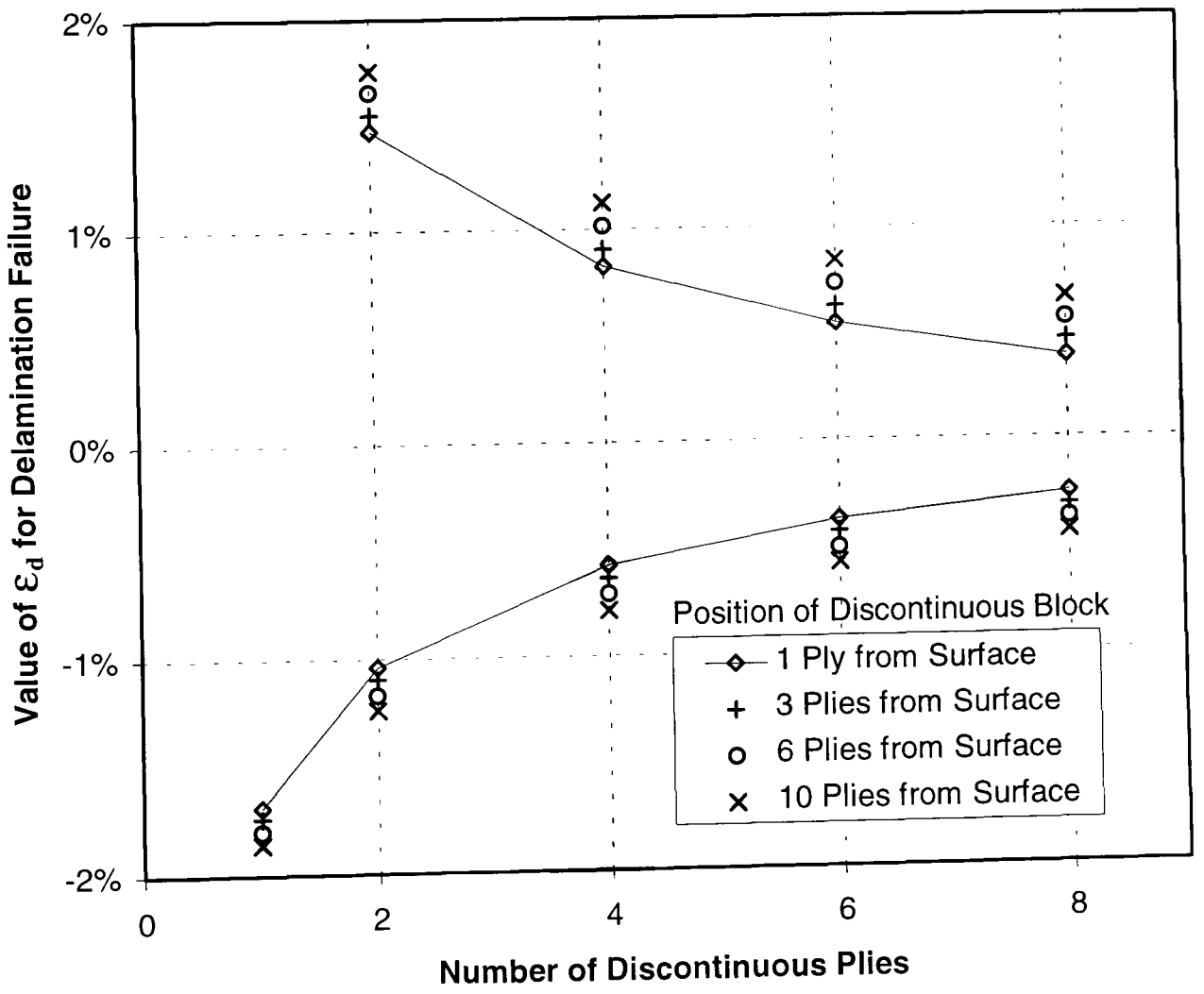


**FIG. 4.11** Failure envelope for 32-ply ($\pm 45°_x$ / $\underline{0°}_x$ / $\pm 45°_x$) glass laminates

To check if it was still valid to ignore the ratio between M and P, the difference between the maximum and minimum values of $\varepsilon_d$ for failure due to delamination was found for a number of carbon and multidirectional glass laminates. The difference was always less than 5%, except when 8 plies were discontinued. For this extreme case the difference was still less than 15%.

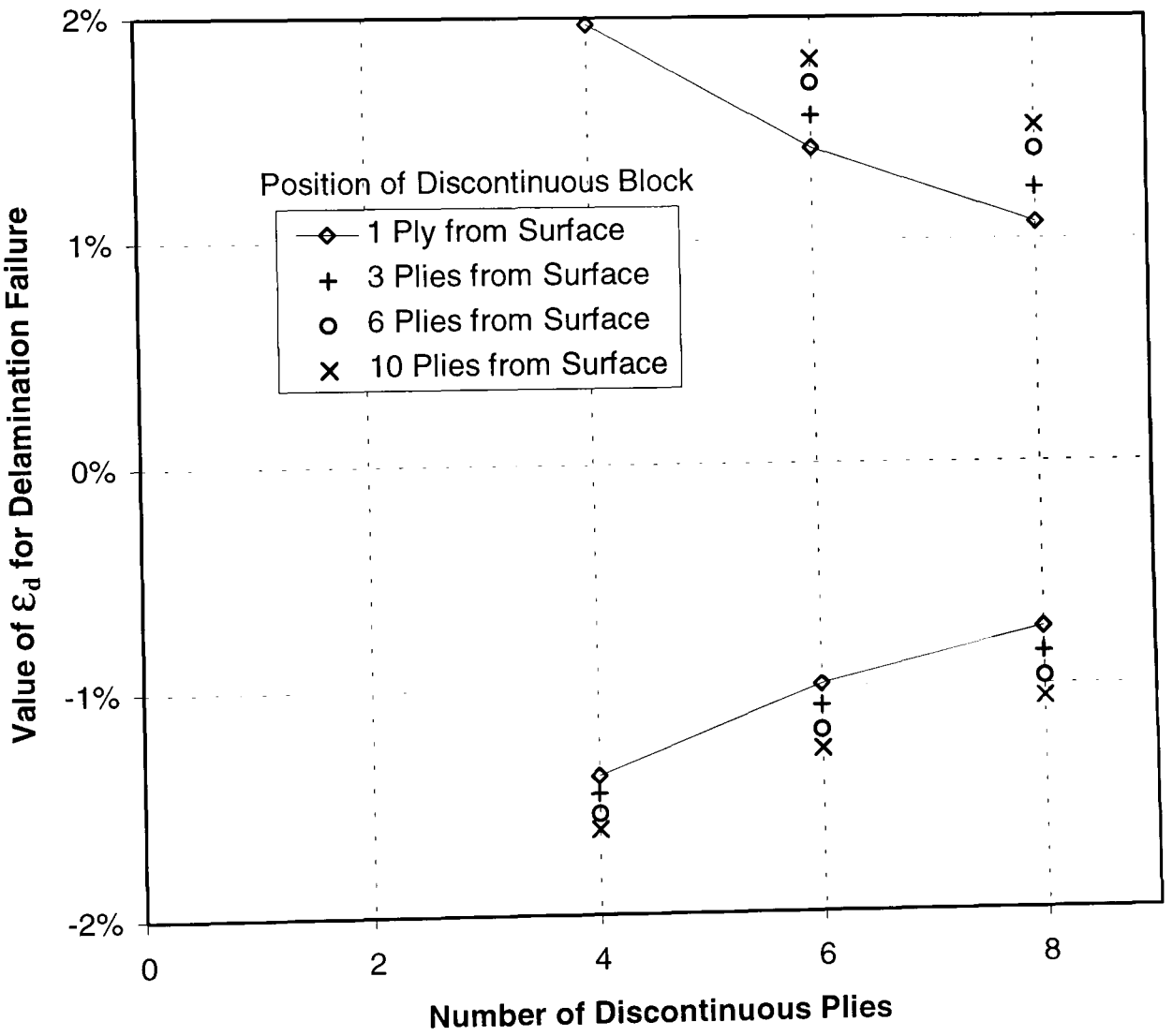


**FIG. 4.12** Failure envelope for 32-ply pure ±45° glass laminates

Using figures 4.9 to 4.13, estimates of the safe limits of $\varepsilon_d$ can be found for similar laminates of any thickness, since G is proportional to t, and therefore $\varepsilon_d$ at delamination is related to $(1 / \sqrt{t})$. However, note that $\varepsilon_d$ for delamination is not exactly proportional to $(1 / \sqrt{t})$ since it also depends on the in-plane failure strains.

which are not proportional to t. Therefore, the following conversion factor is only a first estimate:

$$\varepsilon_d' = \varepsilon_d.\sqrt{(t / t')} \tag{4.38}$$

where $\varepsilon_d$ is the value given by a failure envelope corresponding to a 32-ply specimen, t = 4mm, and $\varepsilon_d'$ is the safe limit of strain corresponding to a laminate of thickness t' (in mm). When converting safe limits of $\varepsilon_d$ for laminates of other thicknesses the non-dimensional thickness and position of the discontinuous block, $\alpha$ and $\beta$, should be used rather than the actual number of plies.

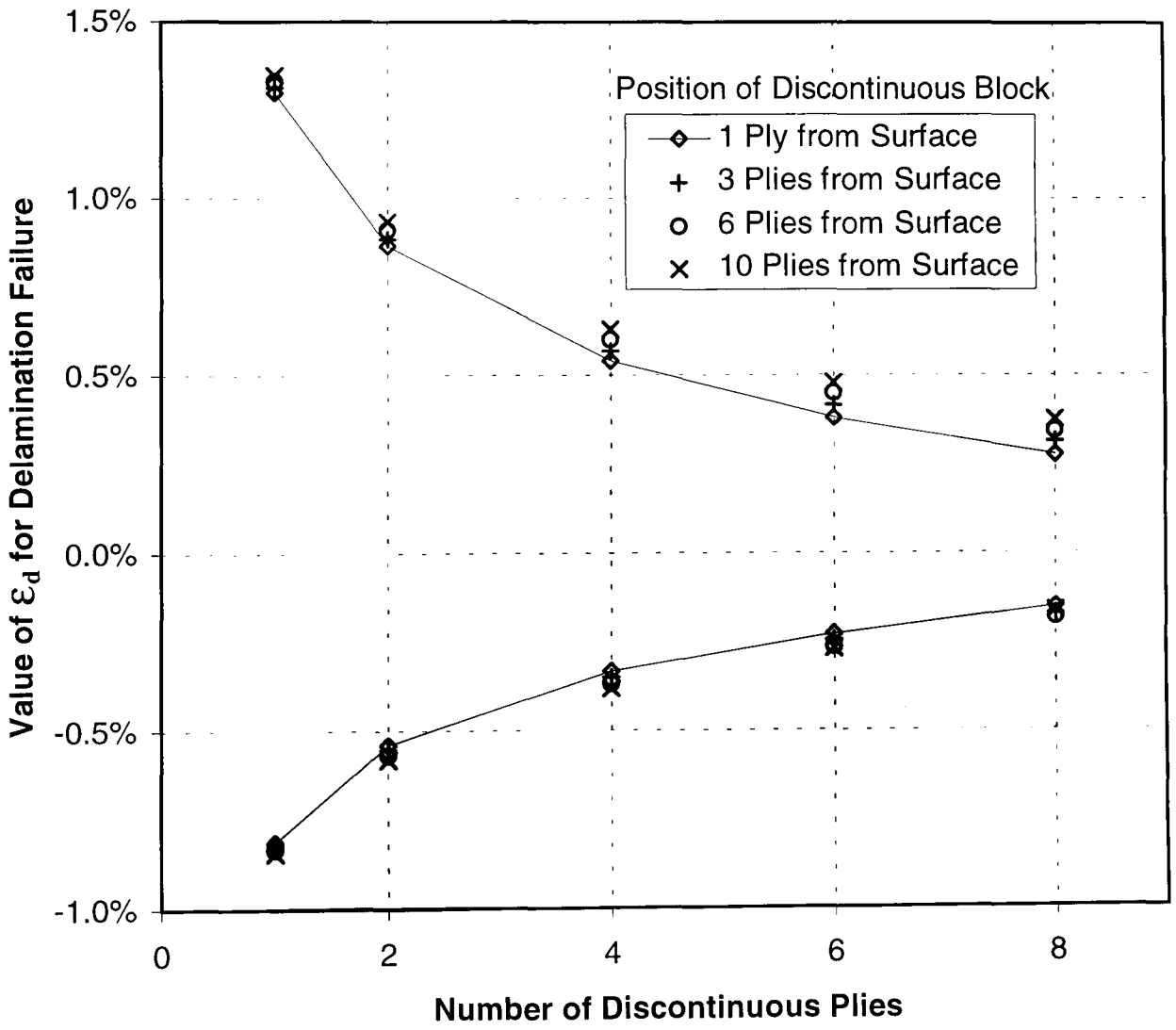


**FIG. 4.13** Failure envelope for 32-ply unidirectional carbon laminates

### Design rules from failure envelopes

Comparing figure 4.9 with figure 4.11, and figure 4.10 with figure 4.12, one will be able to see that the failure envelopes are similar when the type of discontinuous block is the same. Comparing figures 4.9, 4.12 and 4.13, one can see that the stiffer the discontinuous block, the lower the safe limits of $\varepsilon_d$. The lower the value of the axial Young's modulus, $E_x$, of the discontinuous block, the more likely in-plane failure will be the critical failure mode. Thus, for example, it is generally safer to drop ±45° plies than 0° plies. It is also safer to drop plies as close to the neutral axis as possible but remaining on the side generally under axial tension. The effect of the position of the discontinuous block is more pronounced when the surrounding material is less stiff. If an axial design strain is specified, the number of plies that can be discontinued at the same time can be established. For example, for E glass / 913 epoxy, assuming design strains of ±1%, two 0° plies or three pairs of ±45° plies can be safely dropped off internally without risk of delamination.

## 4.6 Conclusions

A closed form solution based on linear-elastic fracture mechanics was derived for calculating the strain energy release rate of delaminations propagating along the interfaces of continuous and discontinuous plies in a composite laminate. The laminate was assumed to consist of three different homogeneous sublaminates and to be under a combination of out-of-plane bending and axial loading.

A parametric study using the analytical solution led to several main observations. Firstly, the strain energy release rate, G, for delaminations above and below a discontinuous, or dropped, block of plies is strongly related to the axial stiffness and strain of the discontinuous block. The position of the discontinuous block through the thickness has a smaller effect on G when the strain at the mid-thickness of the discontinuous block, $\varepsilon_d$, is held constant. For practical purposes, the effect of the ratio between bending and axial loading has negligible effect on G when $\varepsilon_d$ is held

constant. This means that the strain energy release rate can be found quite accurately from a single graph, such as the one in figure 4.7, for any laminate, with any discontinuous block, under virtually any loading conditions. The required parameters are the values of $\varepsilon_d$, ratio of Young's modulus of the discontinuous block to the surrounding continuous material, thickness of laminate, and Young's modulus, position and thickness of the discontinuous block.

Using the analytical solution, failure envelopes for delamination were plotted for various types of laminates based on the strain at the discontinuous block, rather than the applied moment or axial load. The failure envelopes clearly show that the allowable strain at the discontinuous block reduces substantially when the thickness and stiffness of the block increases. The allowable strain is also lower when the discontinuous block is situated closer to the surface, especially if it is under axial compression.

This approach can be used to construct delamination failure envelopes for any material or lay-up. Simple design rules can then be obtained for a specified in-plane design strain.

However, if the laminate is under a significant through-thickness shear loading another route must be taken, as the closed form solution does not account for this. The best option in this case would be to calculate the strain energy release rate using the finite element method.

The next chapter will deal with a straight laminate in bending with shear loading. The virtual crack closure technique via the finite element method will be used to determine the mode I and mode II components of strain energy release rate so that a mixed-mode failure criterion can be employed.

# Chapter 5

# Improved Fracture Mechanics Approach for Laminates with Discontinuous Plies

## 5.1 Introduction

In this chapter the strain energy release rate due to delamination from discontinuous plies in a laminate under three-point bending is calculated using the finite element method. It is found that the strain energy release rate by itself is not adequate for predicting the failure load, although the predicted locations of the delaminations match the test results. Account is, therefore, taken of the yielding which occurs in the resin before crack propagation and a mixed-mode failure criterion is employed. The results of this improved approach compare very well with the experimental data.

Fracture mechanics is a powerful tool for predicting delamination growth in composites. As we saw in chapter 2, the strain energy release rate, G, is often calculated from finite element analysis via the virtual crack closure technique. This procedure has been performed to investigate delamination from the ends of discontinuous plies [69,82]. In [69] the laminates were in four-point bending and in [82] pure axial tension was applied. In [23] a stress based criterion was used to predict the initiation and location of damage in a composite specimen in pure

bending. Fracture mechanics was then used to predict the growth of delamination from the initial damage. Amrutharaj et al [83] developed an approach which modelled the initiation of a fracture process zone with a stress-based criterion, and then used fracture mechanics to predict the propagation of the crack. Thus it was not necessary to ambiguously assume an initial defect. It was used to predict free-edge delamination in laminates. There was good correlation with experimental data, although the value of the yield stress was obtained by curve-fitting the data. A similar approach is used in this chapter to predict delamination from the ends of discontinuous plies.

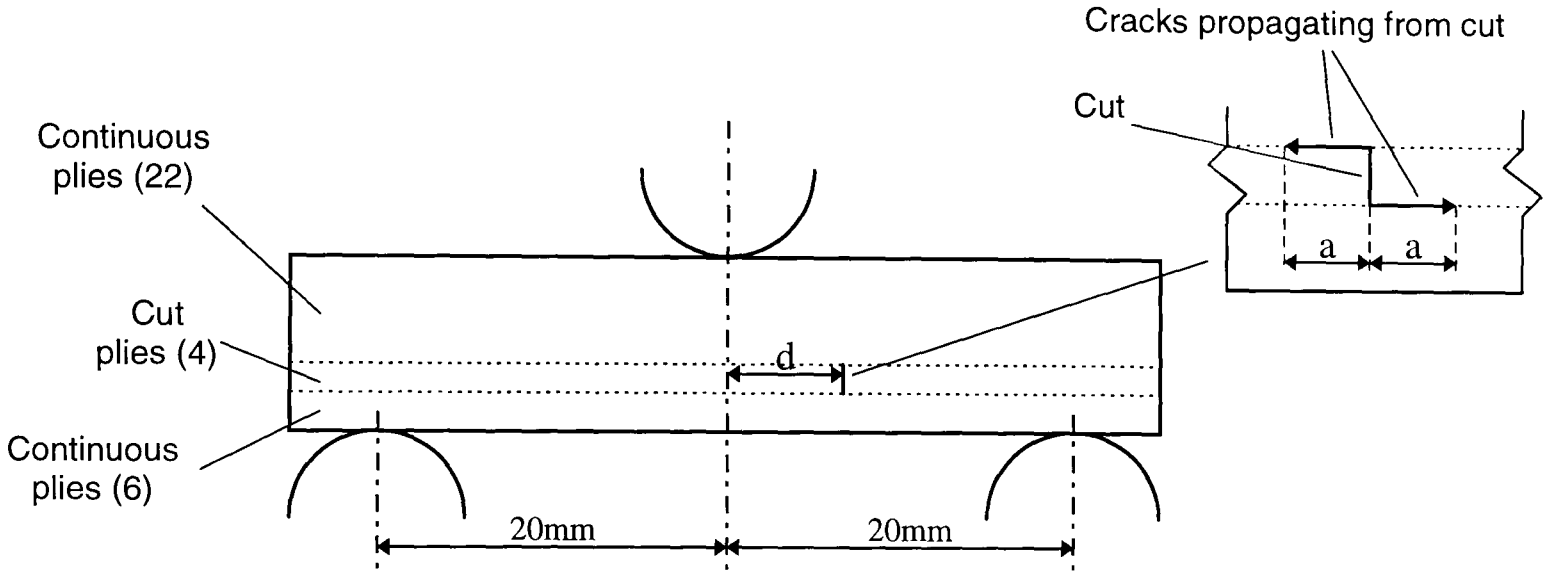


**FIG. 5.1** Schematic diagram of specimen with cut plies in three-point bending

In [84] an account is given of the testing of straight unidirectional laminates in three-point bending, shown schematically in figure 5.1. The laminates consisted of 32 plies of E glass / 913 epoxy and were nominally 10mm wide. Four of the plies near the tension surface were cut across the complete width. The bending moment caused local interlaminar stresses to arise around the cut similar to those induced at ply-drops. The shear force caused overall interlaminar shear stresses to arise in the section of the specimen between the loading rollers. The combination of these two stress distributions caused cracks to initiate at the cut and propagate along the interfaces of the continuous and cut plies, as seen in figure 5.1. Thus, specimen failure was due to delamination at the top left and bottom right of the cut. The ratio

between the overall and local stresses was varied by changing the axial distance, d, between the cut and the central loading roller. The test results indicated a strong interaction between the two types of stress distributions. It was thought that this might be because the overall interlaminar shear stresses enlarged the zones of yielding in the resin rich layers between plies where the delaminations initiated.

When yielding occurs in the resin, the plies on either side are able to move relative to each other. Hence, strain energy can be released even when no physical crack is present. Thus, the larger the yield zone, the longer the effective crack length [85]. This is similar to Irwin's approach where the crack length is assumed to equal its physical length plus the length of the yield zone ahead of the crack tip. The yield zone length is estimated assuming linear-elastic material behaviour. His approach was developed for predicting crack propagation in metal plates with an initial crack. In this chapter it is adapted for predicting delamination in composite laminates with no initial delamination.

The specimens described above are analysed. Two positions of the cut, d = 5mm and d = 15mm, are studied. A finite element model is created and the strain energy release rates of various positions and combinations of cracks is evaluated. From the curves of G with respect to crack length, the locations of the cracks are predicted. The failure load is then predicted both with and without taking the yield zones into account. Both predictions are then compared to the experimental results.

## 5.2 Finite element model

A two-dimensional finite element model was created using CPS4 elements in ABAQUS [59]. These are four-noded plane-stress elements. A plot of the mesh can be seen in figure 5.2, together with the boundary conditions corresponding to d = 5mm. For d = 15mm the same model was used but the boundary conditions were moved left along the mesh by 10mm. Hence, the central loading point was slightly to the right of the centre of the model when d = 5mm, and slightly to the left when d =

15mm. This is exactly what was done during the tests. Since there were stress singularities present at the top and bottom of the cut a fine mesh was created around these two points. The mesh at the cut can be seen more clearly in figure 5.3. The cut is shown by the bold vertical line and four possible delamination paths are indicated with dashed horizontal lines. At the cut the elements are one ply thick and about 0.031mm long, and the length gradually increases moving away from the cut. There are dual coincident nodes along the possible crack interfaces and ends of the block of cut plies. During the testing of the specimens [84], the resin between the ends of the cut plies was seen to crack well before delamination occurred. Thus, the nodes on either side of the cut are not held together. Each pair of nodes along the crack interfaces is initially held together by one stiff spring acting in the horizontal direction and another acting in the vertical direction. This is to enable the virtual crack closure technique to be used. There are also gap elements along the interfaces to stop the two surfaces from crossing once the springs are removed.

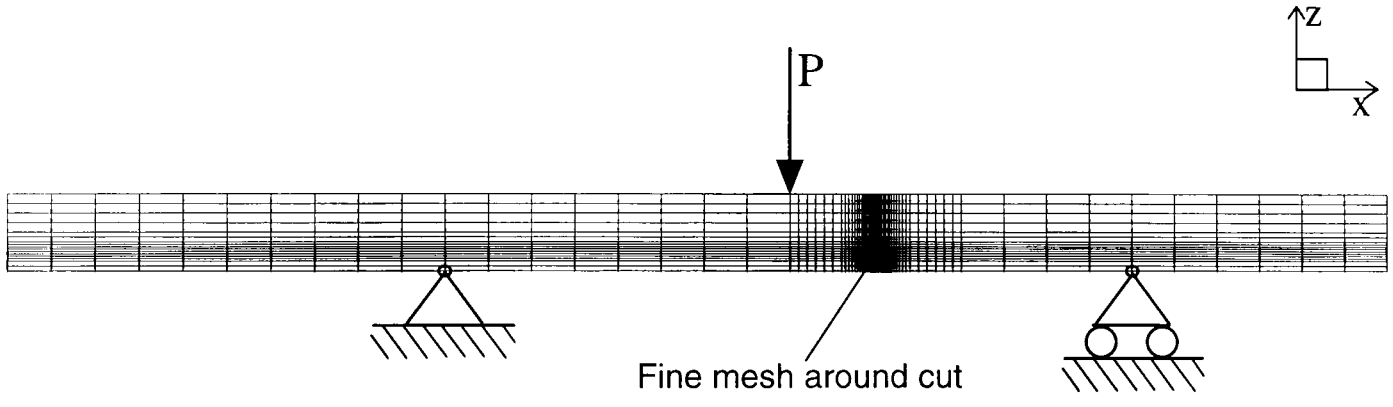


**FIG. 5.2** Finite element model with boundary conditions corresponding to d = 5mm

A downward vertical concentrated load per unit width, P, is applied to the node at the point of contact of the central roller. The node at the point of contact of the left-hand roller is constrained to have zero x and z translation. The node at the point of contact of the roller on the right is constrained to have zero z translation. P is equal to the average experimental failure load per unit width. The value of P is 432.4 N/mm for d = 15mm, and 284.0 N/mm for d = 5mm.

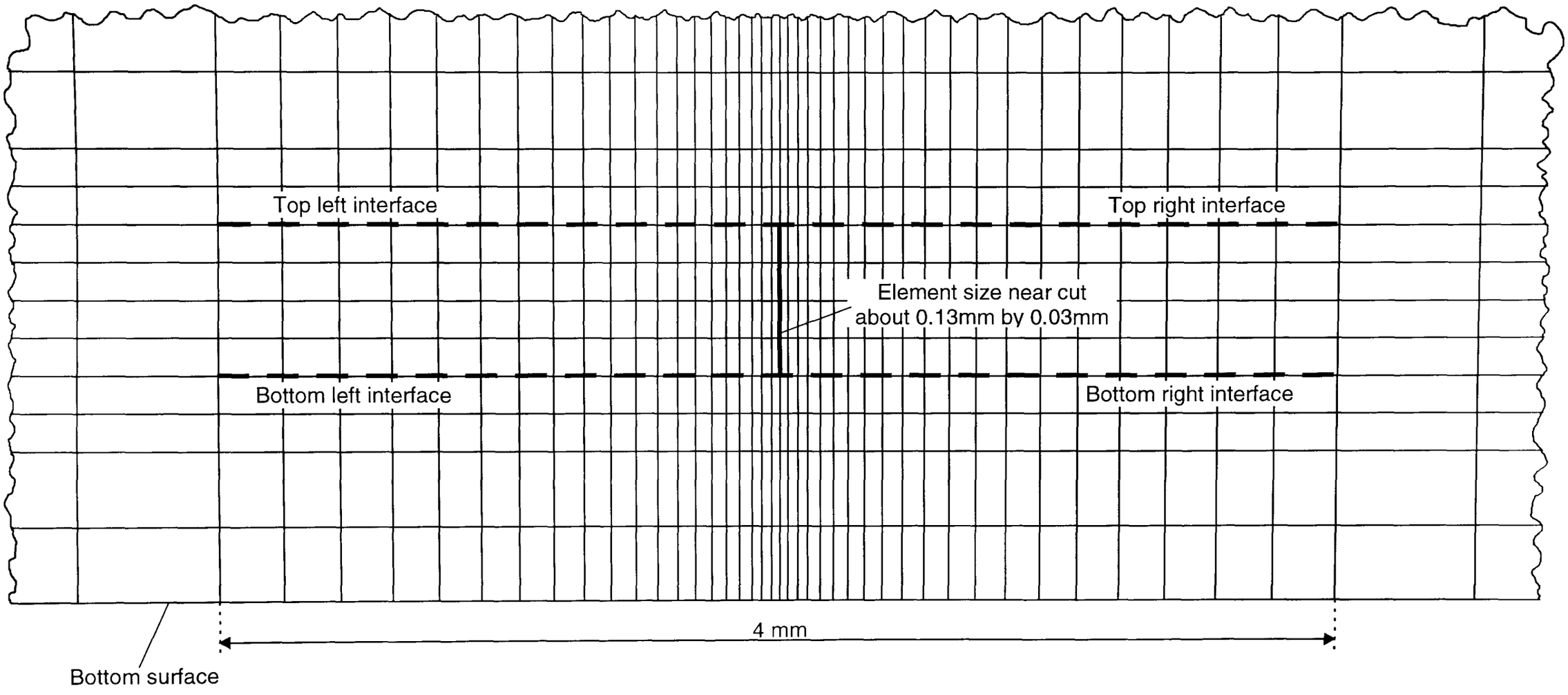


**FIG. 5.3** Close-up of mesh showing cut and possible locations of delaminations

Note that the specimens were loaded under displacement control during the tests. However, the change in stiffness of the model for the crack lengths involved in this study was of the order of only 1%. Hence, the fact that the model was under load control made negligible difference to the following derived strain energy release rate curves and predicted failure loads.

Refer to table 5.1 for the material properties and dimensions of the model. The nominal value of the specimen thickness was initially assumed in the finite element analysis. From the corresponding results, the crack locations were determined. For the failure load predictions, it was deemed more accurate to use the average measured thickness of the specimens and to correct the axial Young's modulus for the lower fibre volume fraction. However, the change in the values of G were small enough not to affect the predicted crack locations.

| | |
|---|---|
| Axial Young's Modulus, $E_x$, for Nominal Thickness | 43.9 GPa |
| Axial Young's Modulus, $E_x$, for Measured Thickness | 41.2 GPa |
| Through-Thickness Young's Modulus, $E_z$ | 15.4 GPa |
| Shear Modulus, $G_{xz}$ | 4.34 GPa |
| Poisson's Ratio, $\nu_{xz}$ | 0.3 |
| Length of Specimen | 80mm |
| Nominal Thickness | 4mm |
| Measured Thickness | 4.33mm |
| Width | 10mm |
| Distance between Outer Rollers | 40mm |

**TABLE 5.1** Material properties and dimensions

## 5.3 Determination of crack locations by total energy approach

The total strain energy release rate, $G_T$, was firstly found for individual cracks at each of the four possible crack locations seen in figure 5.3. $G_T$ was then found for cracks propagating simultaneously along all four crack paths, and finally for cracks propagating simultaneously along the top left and bottom right interfaces.

$G_T$ was calculated from the change in total strain energy in the model as the crack was allowed to propagate by gradually removing the horizontal and vertical springs along the interfaces. This was done at each increment of crack length, a. The schematic definition of a is given in figure 5.1.

Graphs of $G_T$ against a were plotted for all the cases and are given together in figure 5.4 for d = 15mm, and figure 5.5 for d = 5mm. It can be seen that in every case the value of $G_T$ decreases with crack length until it reaches a minimum value, $G_{min}$. After this, the value of $G_T$ generally grows with crack length. This means, as the load is increased, the cracks will propagate in a stable manner up to a short crack length (corresponding to the minimum value of $G_{min}$) and then crack propagation will be unstable. This behaviour was observed in the tests in [84]. Therefore, catastrophic failure occurs when $G_{min}$ reaches the critical value, $G_c$.

Since catastrophic failure depends on the value of $G_{min}$, the locations of the delaminations at failure can be determined by comparing the values of $G_{min}$ corresponding to the different cases studied. The values of $G_{min}$ are given in table 5.2. Referring to the table, it is clear that for d = 15mm the most likely type of failure is by delaminations propagating simultaneously from the top left and bottom right of the cut, since the value of $G_{min}$ is the highest for this situation. For the d = 5mm case, $G_{min}$ is highest when a crack propagates from the bottom right corner only. However, cracks from both the bottom right and top left of the cut were observed in the tests.

Although cracking is primarily mode II due to the type of loading, a small amount of mode I is generally present. Furthermore, the difference between the values of $G_{min}$ for cracking at the bottom right only, and simultaneous cracking at the bottom right and top left is not very great. Thus, the fact that cracking occurred simultaneously at the bottom right and top left, even when the value of $G_T$ was lower in the d = 5mm case, can be explained by more mode I being present. It was therefore concluded that the mode ratio would have to be taken into account for accurately predicting the failure loads.

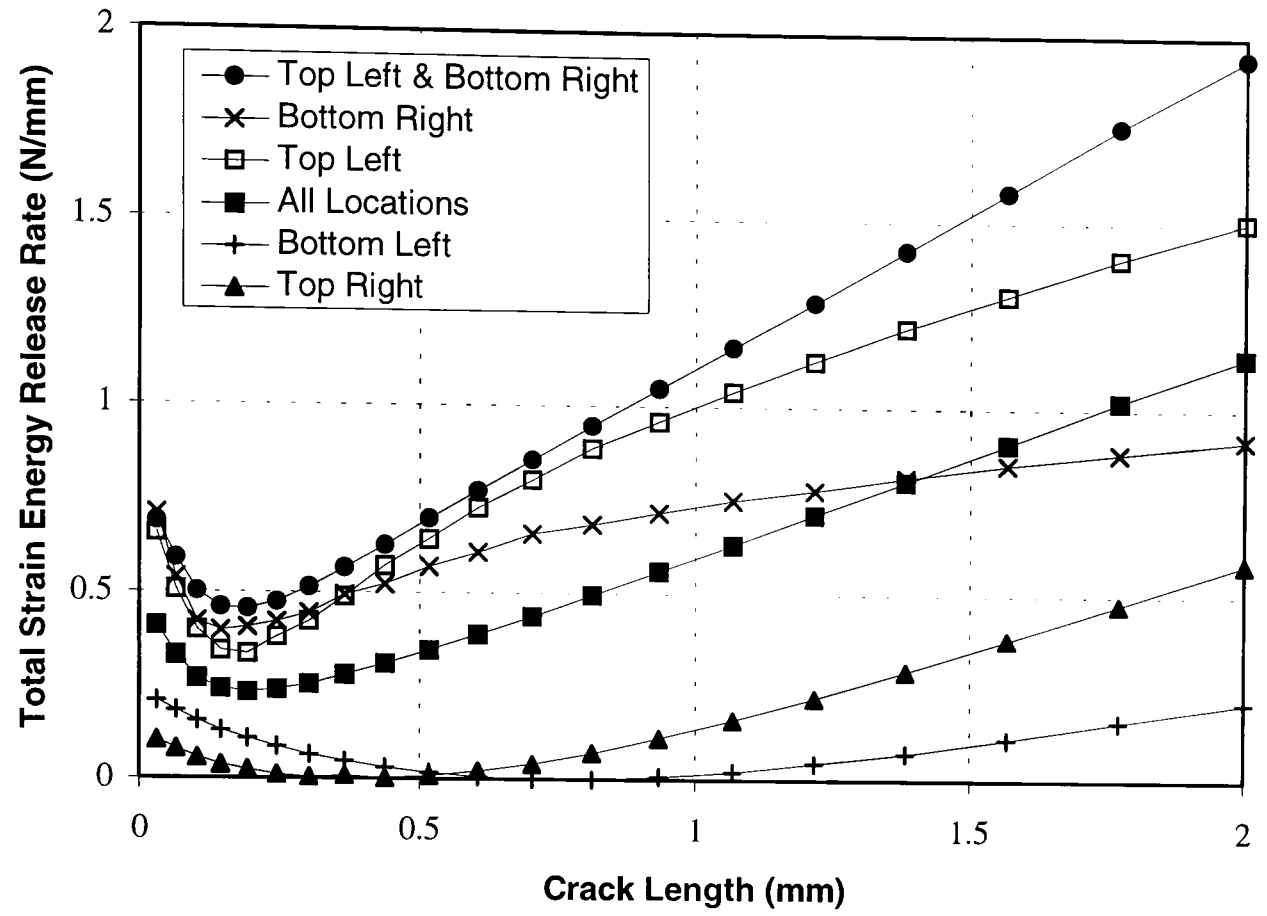


**FIG. 5.4** Strain energy release rate with respect to crack length for different positions and combinations of cracks (cut 15mm from central roller)

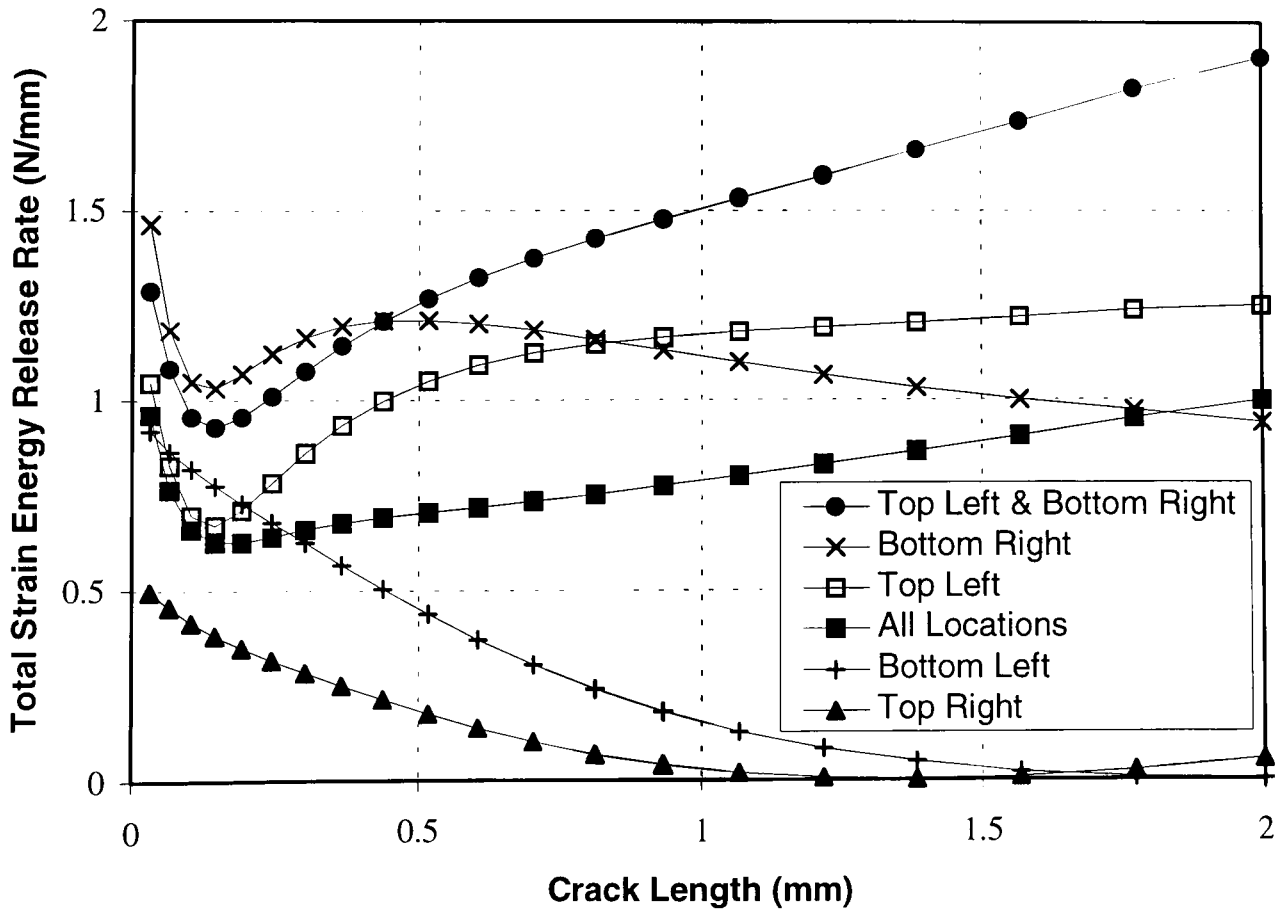


**FIG. 5.5** Strain energy release rate with respect to crack length for different positions and combinations of cracks (cut 5mm from central roller)

| | d = 15mm | d = 5mm |
|---|---|---|
| **Crack at Top Left Only** | 0.34 N/mm | 0.67 N/mm |
| **Crack at Top Right Only** | 0.00 N/mm | 0.00 N/mm |
| **Crack at Bottom Right Only** | 0.39 N/mm | 1.03 N/mm |
| **Crack at Bottom Left Only** | 0.00 N/mm | 0.00 N/mm |
| **Cracks at All Locations** | 0.23 N/mm | 0.63 N/mm |
| **Cracks at Bottom Right & Top Left** | 0.45 N/mm | 0.93 N/mm |

**TABLE 5.2** Minimum values of $G_T$ for various cracks (from figures 5.4 and 5.5)

## 5.4 Failure load predictions using standard mixed mode approach

Cracks were assumed to propagate simultaneously (and at the same rate) along the top left and bottom right interfaces, for both cut positions. The following mixed-mode criterion was used to predict the failure loads:

$$G_I / G_{Ic} + G_{II} / G_{IIc} = 1 \qquad (5.1)$$

where $G_I$ and $G_{II}$ are the mode I and mode II components of the strain energy release rate, respectively, and $G_{Ic}$ and $G_{IIc}$ are their critical values. For E glass / 913 epoxy, the values of the latter obtained from double cantilever beam and end notched flexure tests are $G_{Ic} = 0.25$ N/mm and $G_{IIc} = 1.08$ N/mm, [86].

$G_I$ and $G_{II}$, were found with respect to the crack length, a, using the virtual crack closure technique. This assumes the strain energy released when a crack propagates is equal to the energy required to close the crack. $G_I$ was calculated from the spring forces and relative nodal displacements in the vertical (z) direction, and $G_{II}$ was calculated from the spring forces and relative nodal displacements in the horizontal (x) direction. $G_I$ and $G_{II}$ were then each normalised by their corresponding critical values.

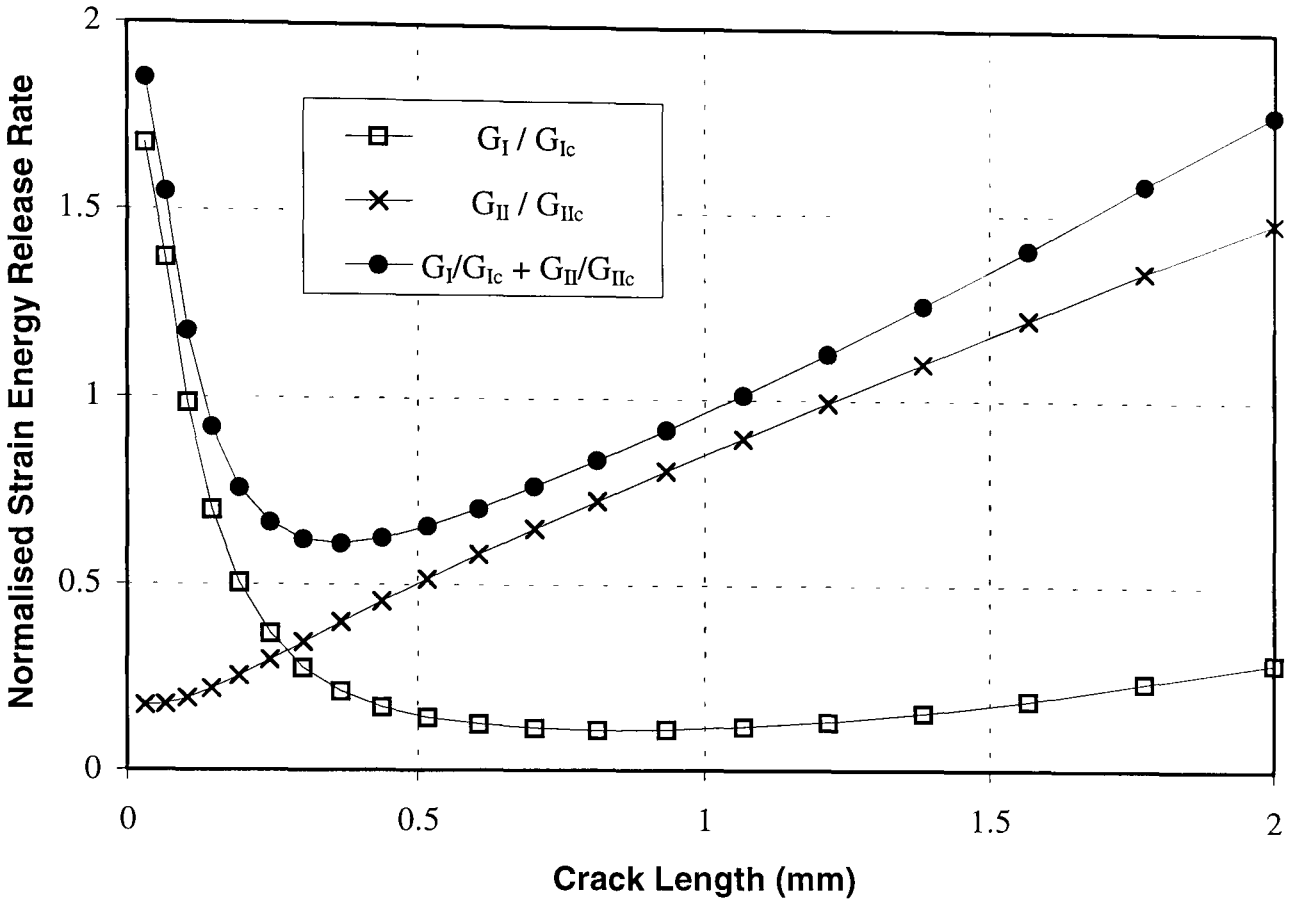


**FIG. 5.6** Normalised strain energy release rate at experimental failure load (cut 15mm from central roller)

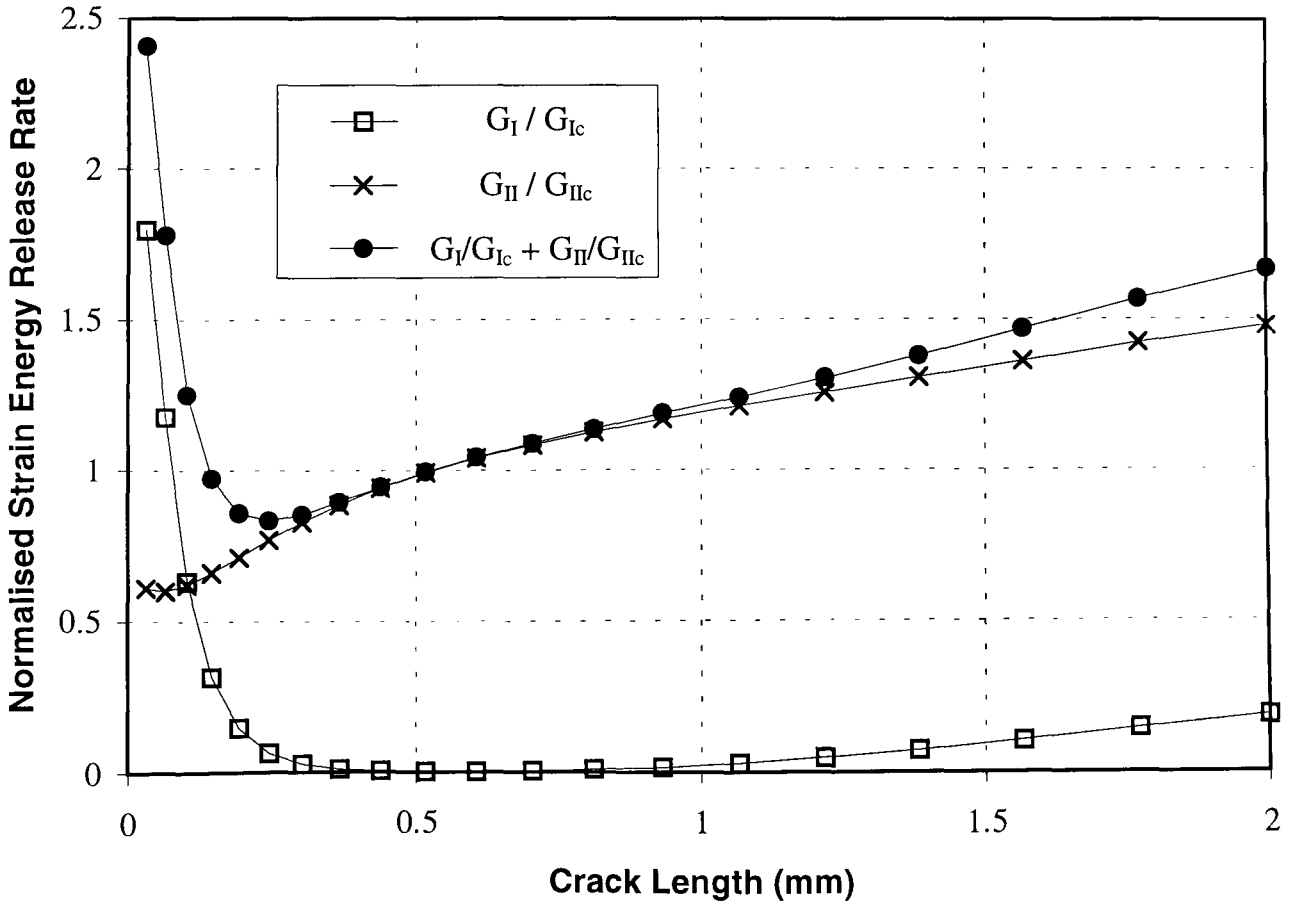


**FIG. 5.7** Normalised strain energy release rate at experimental failure load (cut 5mm from central roller)

The graphs of normalised G against a for the two cut positions (d = 15mm and d = 5mm) can be seen in figures 5.6 and 5.7. One can see the sum of the normalised strain energy release rates, $(G_I/G_{Ic} + G_{II}/G_{IIc})$, decreases to a minimum value as the cracks start propagating. Then, after a crack length between 0.2mm to 0.3mm, the value starts to increase again. As explained in the previous section, this means the load at catastrophic failure is governed by the minimum value of $(G_I/G_{Ic} + G_{II}/G_{IIc})$. At the average experimental failure loads, the minimum values of $(G_I/G_{Ic} + G_{II}/G_{IIc})$ are 0.61 for the d = 15mm case, and 0.83 for the d = 5mm case. Thus, according to (5.1), both the predicted failure loads are higher than the experimental failure loads.

The strain energy release rate is proportional to the square of the applied load, so the predicted failure loads per unit width are 553 N/mm for d = 15mm, and 312 N/mm for d = 5mm.

## 5.5 Improved failure load predictions

The axial distance from the cut to which the zones of yielding material extended was estimated from the finite element analysis. This was done at the top left and bottom right of the cut. The resin along the interfaces of the cut and continuous plies was assumed to yield when the interlaminar shear stress exceeded 70 MPa. This value was estimated from the measured in-plane shear stress-strain response of glass / epoxy ±45° specimens in tension [87], and assuming transverse isotropy. The yield zone length at the top left was averaged with the length at the bottom right. This was the effective initial crack length.

The corresponding value of $(G_I/G_{Ic} + G_{II}/G_{IIc})$ was found by interpolation. If the value of $(G_I/G_{Ic} + G_{II}/G_{IIc})$ was less than one at the effective initial crack length, it meant the predicted failure load was higher than the experimental failure load, and vice versa. If this was the case, the value of $(G_I/G_{Ic} + G_{II}/G_{IIc})$ and the yield zone lengths were recalculated at higher (or lower) values of P.

No further finite element calculations were necessary since the shear stress was proportional to P, and the value of $(G_I/G_{Ic} + G_{II}/G_{IIc})$ was proportional to $P^2$. After a small number of iterations, the predicted failure load converged. The value of $(G_I/G_{Ic} + G_{II}/G_{IIc})$ versus the crack length and the shear stress distributions normalised by the yield stress are all plotted on the same graph in figure 5.8, for the d = 5mm case. Referring to the graph, it can be seen that at the predicted failure load the average yield zone length is equal to the crack length at which equation (5.1) is satisfied. The predicted failure loads for d = 5mm and d = 15mm are given in table 5.3, alongside the previous predictions and the average experimental values.

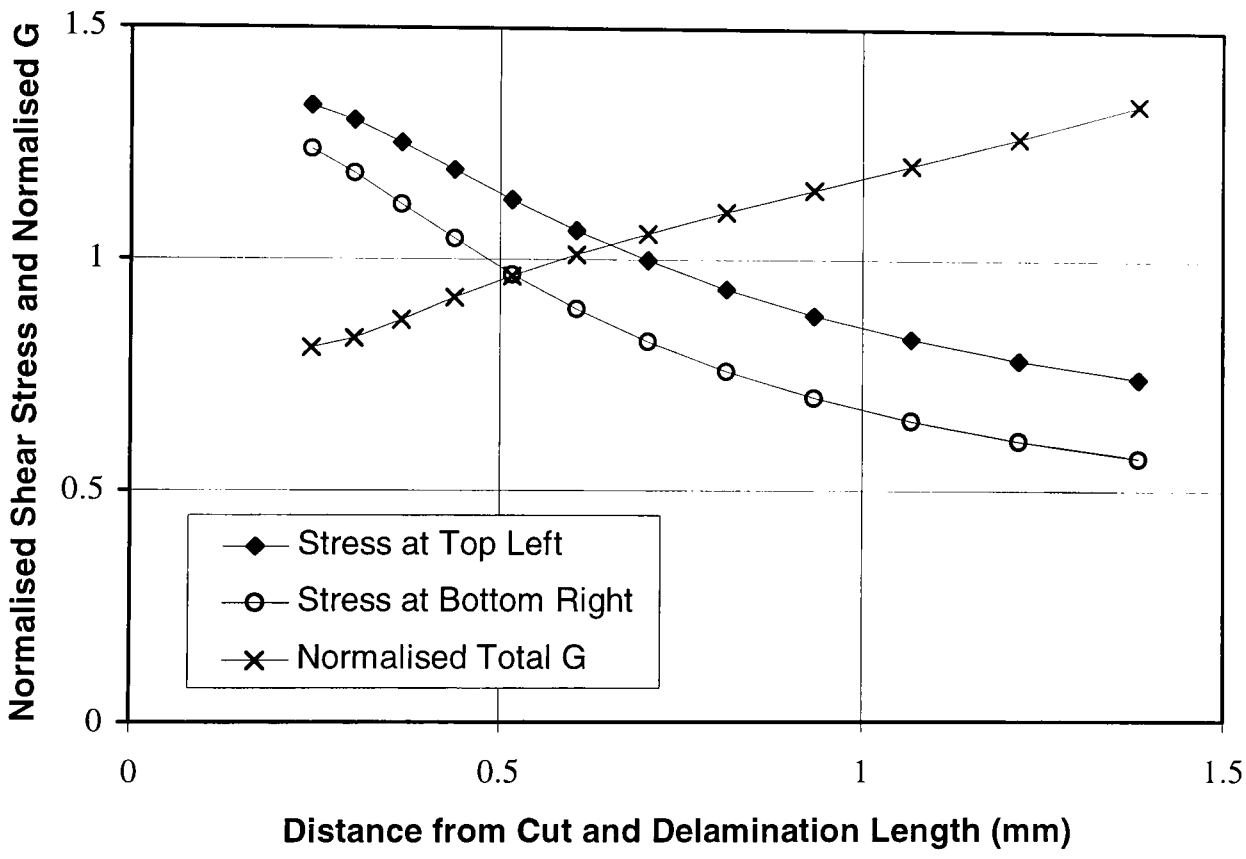


**FIG. 5.8** Normalised strain energy release rate and shear stress distributions at predicted failure load (cut 5mm from central roller)

The values of the yield zone lengths in the d = 5mm case were 0.70 mm at the top left and 0.48 mm at the bottom right of the cut. The values for d = 15mm were 1.57 mm at the top left and 0.38 mm at the bottom right. Although there was a big difference between the latter values, averaging them together was considered to be the best solution for the purposes of keeping the approach manageable.

Note that both the strain energy release rate and the yield zone lengths were calculated assuming linear-elastic material properties. The estimated yield zone lengths would be longer if non-linear stress-strain behaviour was taken into account. However, the strain energy release rate would be lower since yielding limits the stresses at the crack tip. Thus, to some degree these two effects cancel each other out. Also, to accurately predict the yield zone length and corresponding strain energy release rate, the resin along the interfaces would have to be modelled using non-linear material properties. This would require much more computational time, and for the purpose of engineering design, the approach used above is thought to be reasonable.

| | **d = 15mm** | **d = 5mm** |
|---|---|---|
| **Experimental Average** | 432.4 N/mm | 284.0 N/mm |
| **Prediction (Standard Mixed-Mode)** | 553 N/mm | 312 N/mm |
| **Prediction (Including Yield Zones)** | 444 N/mm | 280 N/mm |

**TABLE 5.3** Failure loads (per unit width)

## 5.6 Discussion

Referring to figures 5.4 and 5.5, it is interesting to note that the strain energy release rates corresponding to crack propagation at the top right and bottom left interfaces are generally much lower than the ones corresponding to the top left and bottom right interfaces. This is what would be expected since the overall interlaminar shear stress is of the same sign as the local shear stress at the top left and bottom right of the cut, and of opposing signs at the other two locations. Hence, the interlaminar shear stress is greater in the former locations.

It is also interesting to consider the unusually high mode I component of strain energy release rate in the first 0.2mm of crack growth, as shown in figures 5.6 and

5.7. When the stresses around the cut from finite element analysis were examined, it was found that the high $G_I$ was due to large through-thickness tensile stresses existing locally near the corners of the cut.

The analysis showed that when no account is taken of yielding, linear-elastic fracture mechanics is not able to accurately predict delamination in laminates with significant overall interlaminar shear stresses. Referring to table 5.3, it can be seen that the failure loads predicted without accounting for yielding at the onset of delamination are both very unconservative. The prediction for the d = 15mm case is 28% higher than the experimental value, and the prediction for the d = 5mm case is 10% higher. The prediction corresponding to the d = 15mm case is worse because the ratio between the shear force and the bending moment is higher when the cut is further from the central roller. Hence, the relative importance of the overall interlaminar shear stress is greater, and the yield zones are generally longer when d = 15mm. When the improved approach is applied to the two cases, the predictions are within 3% of the experimental results. Therefore, the improved approach was able to accurately predict the failure loads of laminates with two different levels of yielding.

Previously it was found that a linear interaction equation between the effects of overall interlaminar shear stresses and local stresses at the cut gave a good prediction of failure [84]. The results presented here explain the interaction in terms of the increased effective crack length as the overall interlaminar shear stresses become high compared with the yield stress.

## 5.7 Conclusions

A composite specimen containing cut plies under three-point bending was analysed. The ratio between the bending moment and the shear force at the cut was varied by changing the position of the cut relative to the applied loads. The strain energy release rate was calculated for delaminations spreading from the cut using finite element analysis. A mixed-mode failure criterion, based on the strain energy release

rate, grossly overestimated the failure loads for both cut positions. An improved approach, also based on the mixed-mode failure criterion but which took account of yielding in the resin at the onset of delamination, was able to predict the failure loads to within 3% of the experimental values. This shows the importance of considering the yielding that occurs before crack formation when predicting delamination in laminates under high overall interlaminar shear stresses.

In the next chapter we will extend the application of this approach to curved laminates with discontinuous plies, where there are significant overall through-thickness tensile stress distributions.

# Chapter 6

# Improved Approach Applied to Curved Laminates with Discontinuous Plies

## 6.1 Introduction

In the previous chapter we saw that a fracture mechanics based approach which took account of the resin yielding prior to crack propagation was able to accurately predict the delamination failure loads of straight laminates in three-point bending. Failure was due to a combination of local interlaminar stresses around the discontinuous block of plies, and overall interlaminar shear stresses caused by the out-of-plane shear load.

In this chapter, we will apply the same approach to a slightly different scenario. Delamination will be predicted in curved laminates under pure bending. In this case failure is due to a combination of local interlaminar stresses around the discontinuous block of plies, and overall through-thickness tensile stresses induced by the curvature and bending moment.

In [88] an account is given of the testing of curved unidirectional laminates in four-point bending, shown schematically in figure 6.1. The laminates consisted of 32 plies of E glass / 913 epoxy and were nominally 10mm wide. Four of the plies near the tension surface were cut across the complete width, as on the straight specimens.

Again, the local stress distribution induced by the cut is very similar to that which would arise at a ply drop. The ratio of the local and overall stress distributions was varied by making two sets of specimens with different through-thickness locations of the cut. The cut plies in one set of specimens were located very close to the tension surface, with only two continuous plies separating them from the surface. The cut plies in the other set of specimens were located closer to the mid-thickness, separated from the tension surface by six continuous plies.

All of the specimens failed catastrophically with no prior stable delamination visible. The locations of the delaminations can be seen in figure 6.2. Delaminations propagated on both sides of the cut along the interface further from the surface, and on either one or both sides of the cut along the interface near the surface. The bending strains of the curved specimens were recorded during the tests from strain gauges attached to both surfaces of the curved section, and hence the bending moments were calculated [88].

These specimens are analysed in this chapter and the failure loads are predicted. A comparison is then made with the experimental results.

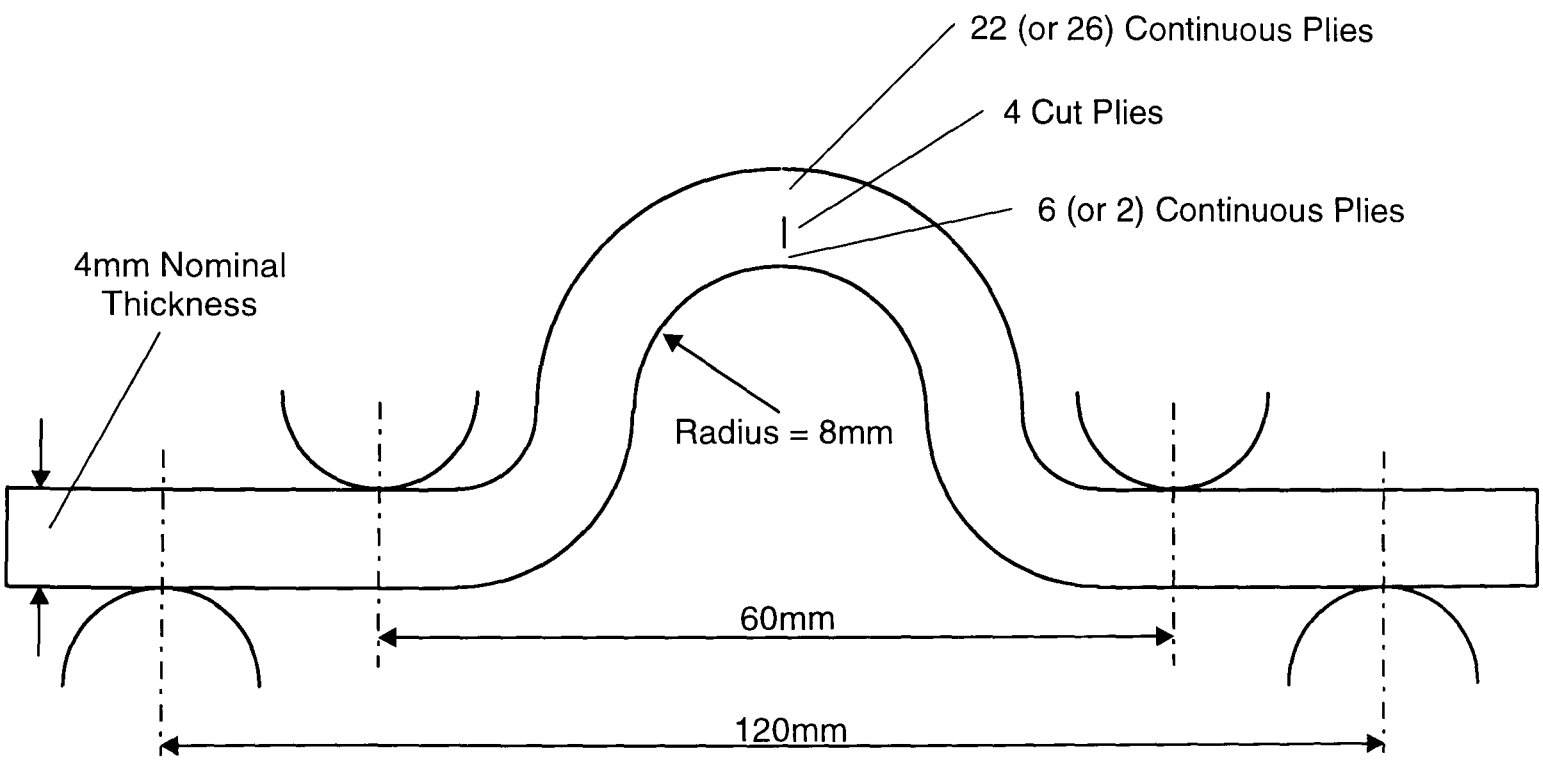


**FIG. 6.1** Schematic diagram of curved specimen in four-point bending

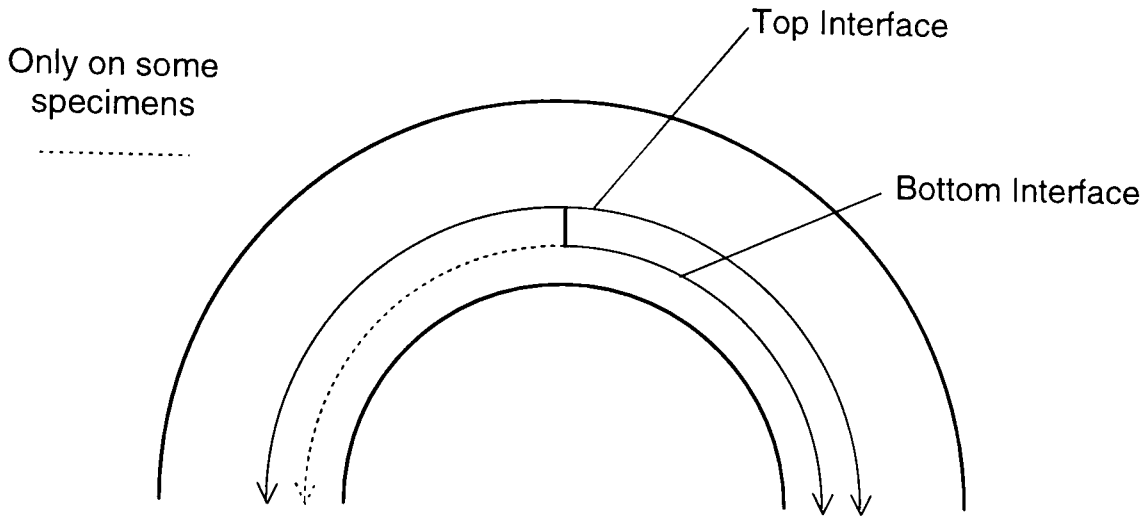


**FIG. 6.2** Locations of delaminations observed in tests

## 6.2 Finite element models

As with the previous specimens, two-dimensional finite element models were created with CPS4 elements in ABAQUS [59]. To reduce the processing time, only ninety degrees of the curved section of the specimens were modelled. There were dual coincident nodes along the crack interfaces and ends of the block of cut plies. Each pair of nodes along the crack interfaces was initially held together by one stiff spring acting in the circumferential direction and another acting in the radial direction. Similarly to the straight specimens, the resin between the ends of the cut plies was seen to crack well before delamination occurred [88], thus the nodes on either side of the cut were not held together.

The mesh of the curved specimen with the cut further from the surface can be seen in figure 6.3, along with the boundary conditions. The mesh corresponds to the model under load with all the spring elements removed so that the cut and crack locations can be seen more clearly. The elements around the cut are roughly 0.06mm square. The mesh of the specimen with the cut closer to the surface is very similar to the one in figure 6.3.

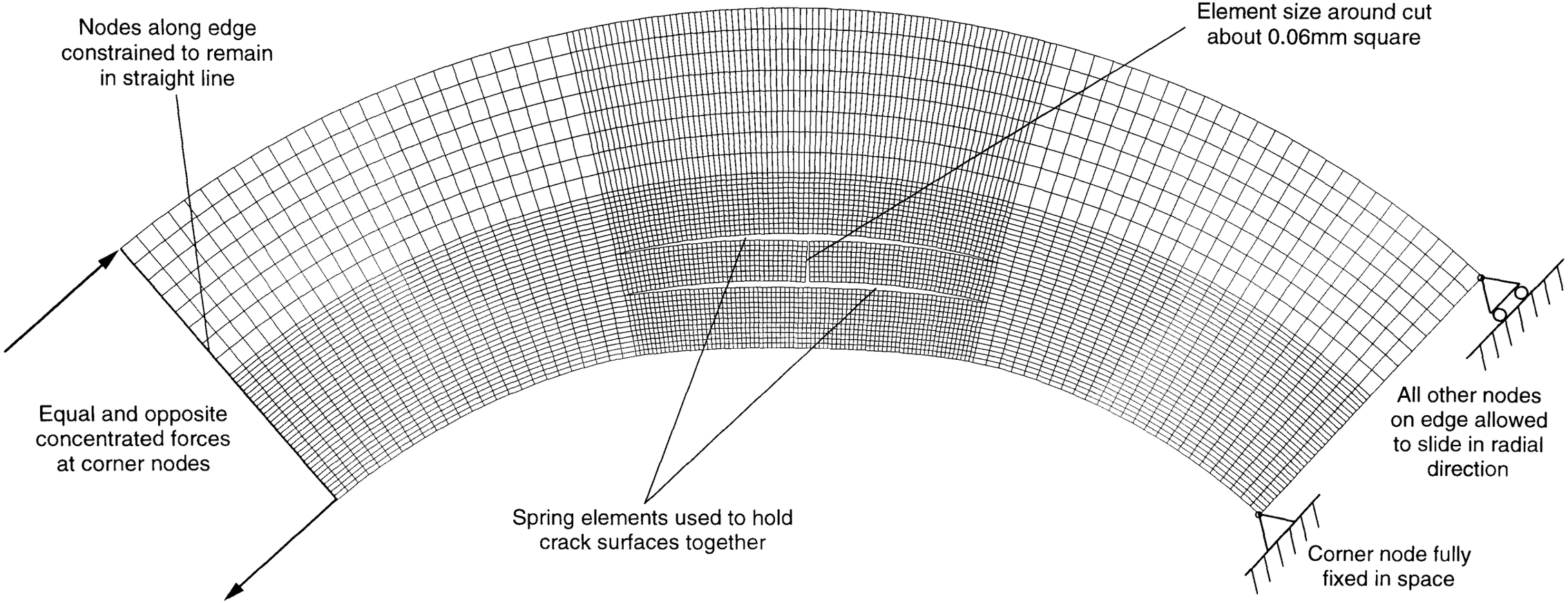


**FIG. 6.3** Deformed finite element model of curved specimen with cut further from surface

The measured thickness of each specimen varied slightly. This was probably due to different amounts of resin bleed during the curing process. The average measured thicknesses of each type of specimen was therefore used for each model. This was 4.06mm for the specimens with the cut nearer the surface, and 4.15mm for the other set of specimens. The nominal material properties given in table 3.3 were used, except that the value of the axial Young's modulus was corrected for fibre volume fraction. This made no difference to the specimens with the cut closer to the surface, but the modulus for the other set of specimens reduced to 42.99 GPa.

The average experimental bending moment per unit width at failure for the specimens with the cut nearer the surface was 1357 Nmm/mm, and for the other set of specimens it was 1802 Nmm/mm [88]. These bending moments were applied to the respective models and the finite element analyses were performed assuming small deformations. The analyses were divided into many steps so that spring elements could be gradually removed in each step to simulate crack propagation.

## 6.3 Estimation of yield zone lengths

The first step in predicting the failure loads of the specimens was to estimate the lengths of the zones of yielding material from the finite element analysis. Only the interlaminar shear stress was considered when predicting yielding in the straight specimens. However, since there are significant through-thickness tensile stresses in the curved specimens, it was decided to use an interactive yield criterion. As mentioned in chapter 2, Raghava's yield criterion (2.6) has been seen to work well for polymers [13,14], and was therefore chosen to predict the size of the yield zones. For plane stress (2.6) reduces to:

$$\sigma_I^2 + \sigma_{II}^2 + (\sigma_I + \sigma_{II})(\sigma_Y^c - \sigma_Y^t) - \sigma_I.\sigma_{II} \geq \sigma_Y^t.\sigma_Y^c \qquad (6.1)$$

where $\sigma_Y^t$ and $\sigma_Y^c$ are the absolute values of the yield stress in tension and compression, respectively, and $\sigma_I$ and $\sigma_{II}$ are the principal stresses. The principal

stresses should correspond to those in the resin rich layers between plies, where the cracks are assumed to propagate. However, the stresses from the finite element analysis are based on models assuming the composite to be a homogeneous material.

The axial stresses in the resin are not the same as the axial stresses in the fibres. On the other hand, the axial strains in the resin are constrained to equal the axial strains in the adjacent fibres. Therefore, the axial strains in the resin rich layers are equal to the axial strains given by the finite element solution. For plane stress conditions in the 1-3 plane, the relationship between stress and strain in an isotropic material is,

$$\sigma_1 = E.\varepsilon_1 + \nu.\sigma_3 \qquad (6.2)$$

Thus, the axial stresses along the resin rich layers could be calculated from the through-thickness tensile stresses and the axial strains obtained directly from the finite element analysis.

The interlaminar shear and tensile stresses in a resin rich layer are equal to the stresses in the adjacent composite material, since all the through-thickness loads have to be transferred across the resin rich layer. Thus, these stresses could be obtained directly from the finite element analysis.

The principal stresses in an isotropic material are related to the stress components in the 1 and 3 directions as follows:

$$\sigma_I = \tfrac{1}{2}(\sigma_1 + \sigma_3) + \tfrac{1}{2}\sqrt{(\sigma_1 - \sigma_3)^2 + 4\tau_{13}^2} \qquad (6.3)$$

$$\sigma_{II} = \tfrac{1}{2}(\sigma_1 + \sigma_3) - \tfrac{1}{2}\sqrt{(\sigma_1 - \sigma_3)^2 + 4\tau_{13}^2} \qquad (6.4)$$

Taking $\tau_{13}$ as the interlaminar shear stress, and $\sigma_1$ and $\sigma_3$ as the normal stresses in the axial and through-thickness directions, respectively, the principal stresses in the resin rich layers were calculated at various distances away from the cut.

The values of $\sigma_Y^t$ and $\sigma_Y^c$, were derived as follows from the shear yield stress, which was assumed to be 70MPa in the previous chapter. In a state of pure interlaminar shear, where $\sigma_1$ and $\sigma_3$ are both zero, the principal stresses can be found from,

$$\sigma_I = -\sigma_{II} = \tau_{13} \tag{6.5}$$

Substituting (6.5) into (6.1) gives,

$$3\tau_{13}^2 \geq \sigma_Y^t.\sigma_Y^c \tag{6.6}$$

The ratio of compressive to tensile yield stresses, $\sigma_Y^c$ / $\sigma_Y^t$, has been found to be close to 1.3 for several types of polymers [14]. If we assume this value for our resin and substitute the value of the shear yield stress in (6.6), we obtain,

$$\sigma_Y^t = 106\text{MPa} \qquad \sigma_Y^c = 138\text{MPa}$$

Assuming the Young's modulus and Poisson's ratio of the resin to be 4GPa and 0.38, respectively, the principal stresses in the resin rich layers where crack propagation occurred were calculated at various distances from the cut. At each distance, the left hand side of (6.1) was then evaluated and normalised by dividing by the product $\sigma_Y^t.\sigma_Y^c$. This normalised Raghava criterion was finally plotted against the distance along the crack interface from the cut to estimate the yield zone lengths.

Refer to figures 6.4 and 6.5 for the graphs corresponding to each type of specimen at their average experimental failure loads. The zone of yielding material was assumed to extend up to the point where the normalised Raghava criterion equalled one. Due to symmetry, the yield zones extended equal distances on both sides of the cut. Therefore, only the stress distributions on one side of the cut are given.. However, the yield zone closer to the surface was not exactly the same length as the yield zone further from the surface. Therefore, for simplicity these two lengths were averaged together before comparison with the strain energy release rate distributions.

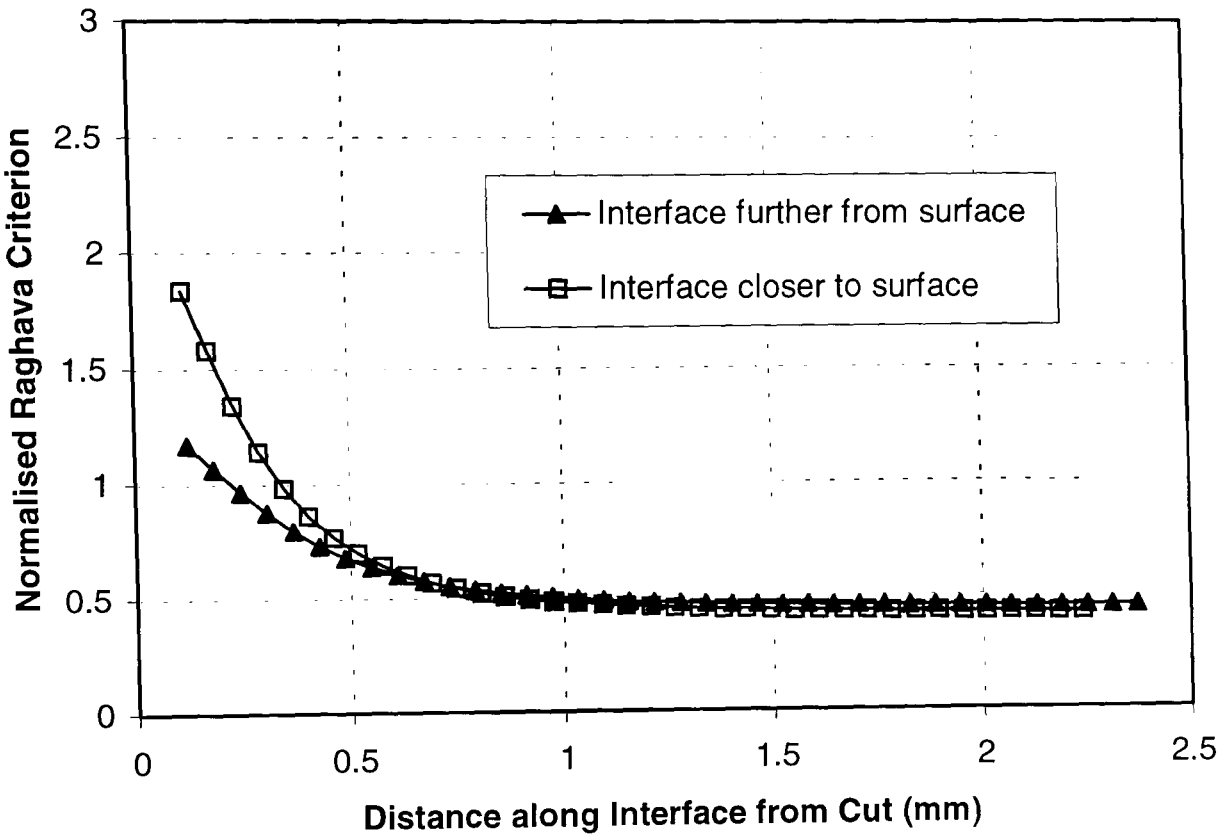


**FIG. 6.4** Stress distributions along crack paths in specimens with cut further from surface

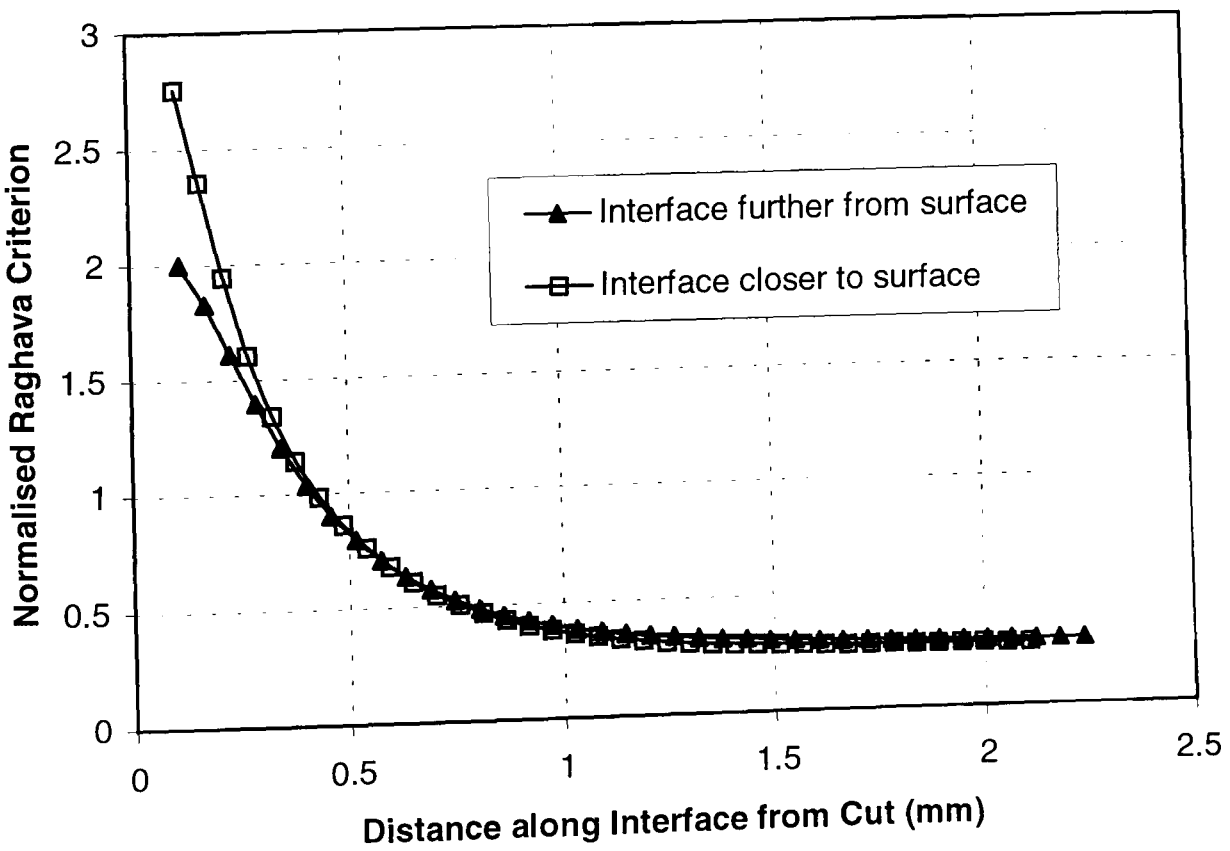


**FIG. 6.5** Stress distributions along crack paths in specimens with cut closer to surface

Note that the specimens were under displacement control during the tests, yet a constant load was applied to the FE model. However, the average yield zone length was 0.30mm for the specimens with the cut further from the surface, and 0.42mm for the specimens with the cut closer to the surface. For crack lengths of this order there is virtually no difference in stiffness from the uncracked specimens, hence, for the purpose of this analysis, the type of loading does not matter.

## 6.4 Failure load predictions

The mode I and mode II strain energy release rates, $G_I$ and $G_{II}$, were calculated using the virtual crack closure technique as described in previous chapters. Cracks were assumed to propagate simultaneously and at equal circumferential increments along the interfaces further and closer to the surface, on both sides of the cut. The previous mixed-mode failure criterion, (5.1), was used along with the same values of $G_{Ic}$ and $G_{IIc}$. Graphs of the normalised strain energy release rate versus the crack length can be seen in figures 6.6 and 6.7. Note that the crack length in this case is the average length of the two cracks on one side of the cut.

It is interesting to notice the high amount of mode I indicated by both graphs at the start of crack growth, which rapidly diminishes. The mesh is not fine enough to show the sharp gradient very clearly, but the trends are similar to those found for the straight specimens with cut plies. Nevertheless, the strain energy release rate in the first 0.2mm of crack growth is not of importance, since the yield zones extend beyond this length. At crack lengths of the order of the size of the yield zone lengths, the normalised strain energy release rate curve has a positive gradient. Therefore, as soon as the strain energy release rate is high enough for cracks to propagate, crack propagation will accelerate and catastrophic failure will occur. Hence, the analysis predicts the unstable crack growth which was observed in the tests [88].

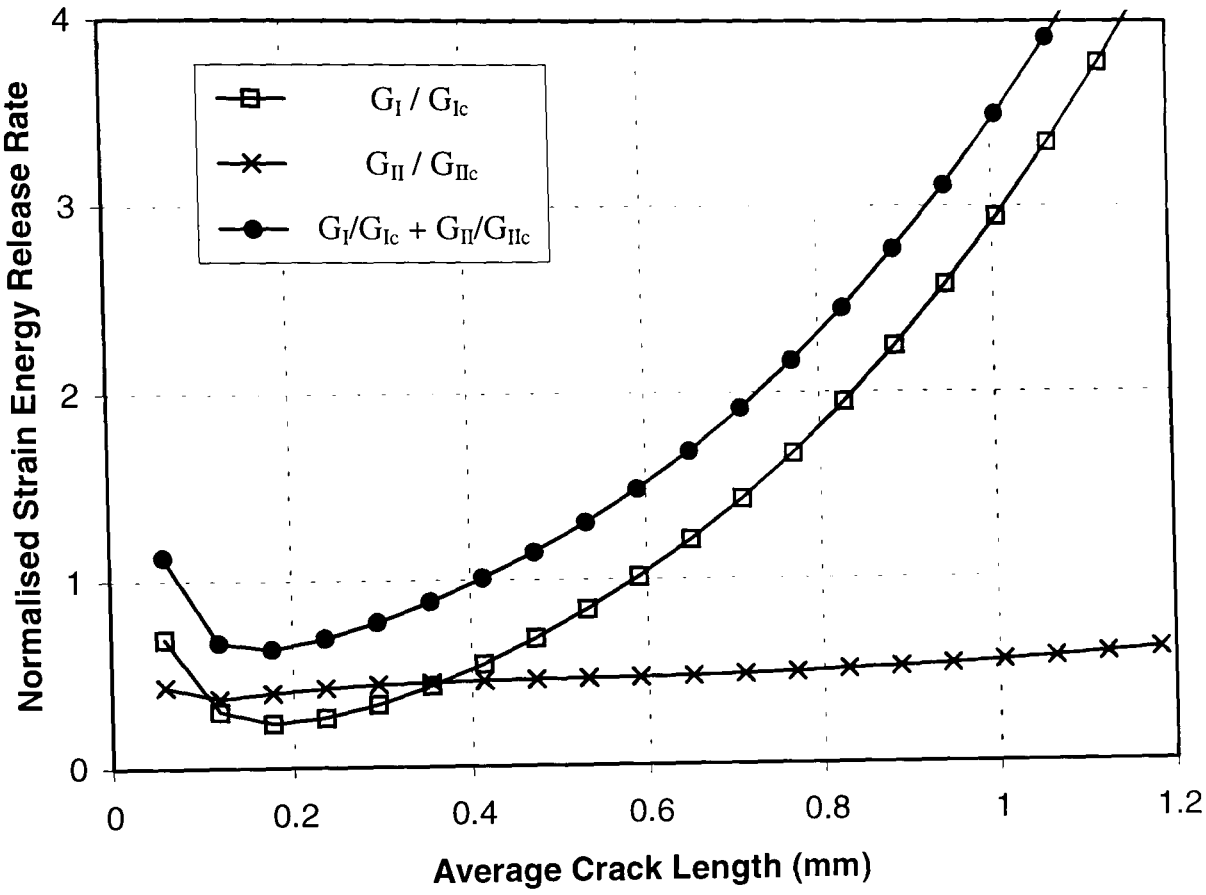


**FIG. 6.6** Normalised strain energy release rate at experimental failure load (specimens with cut further from surface)

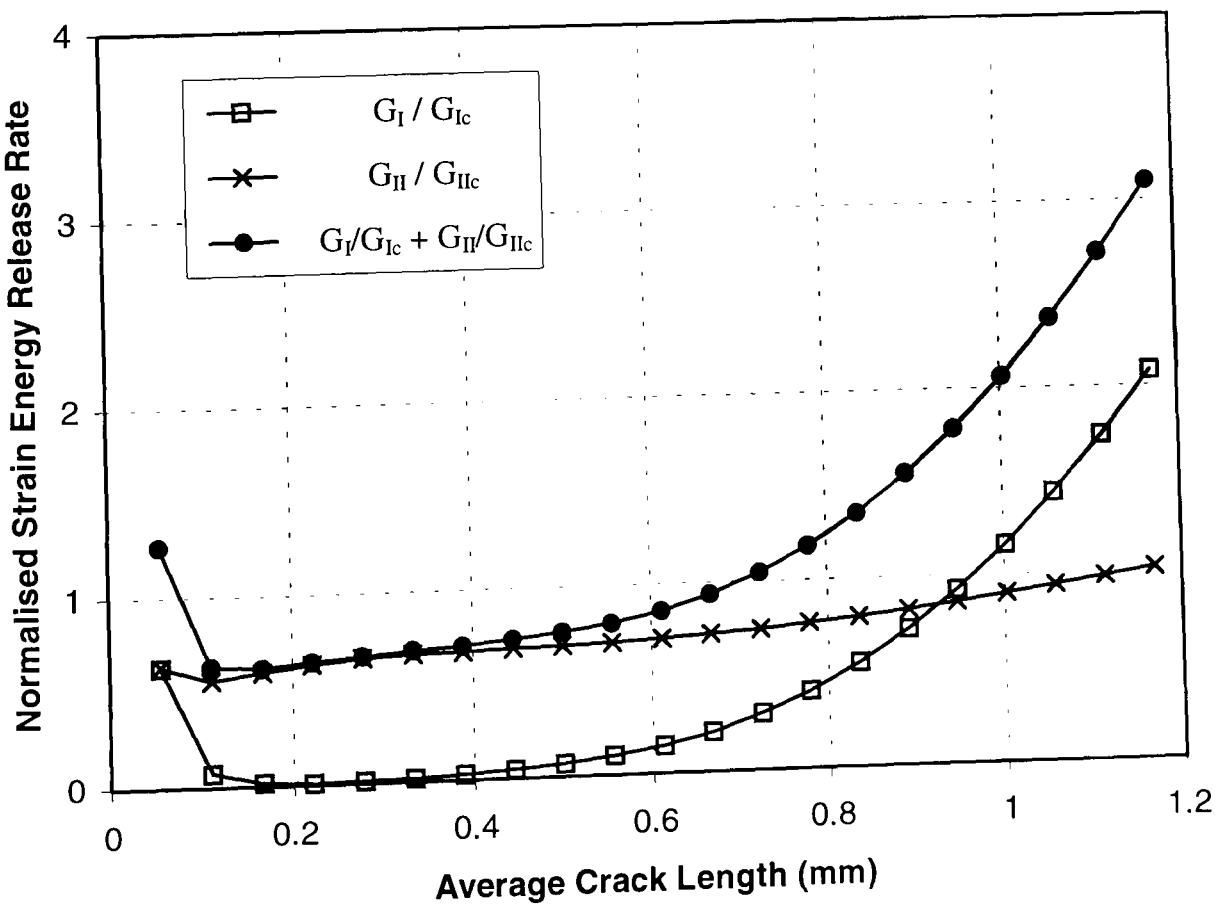


**FIG. 6.7** Normalised strain energy release rate at experimental failure load (specimens with cut closer to surface)

One will also notice the relatively higher mode I component of strain energy release rate in the specimens with the cut further from surface. This is due to the higher overall through-thickness tensile stresses and lower local shear stresses compared to the specimens with the cut closer to surface.

In both cases it can be seen that the average yield zone lengths are smaller than the crack lengths necessary for sufficient strain energy release rate for crack propagation. Therefore the calculations were repeated at higher loads. Since the strain energy release rates were directly proportional to the square of the load, and the stresses were directly proportional to the load, new values of the yield zone length and the necessary crack length could be found without the need for further finite element analysis. The bending moments at which the yield zone lengths were equal to the minimum crack lengths necessary for crack propagation were predicted after a small number of iterations. The predictions for both types of specimen can be seen in table 6.1 alongside the experimental bending moments at failure.

| | **Experimental** | **Prediction** |
|---|---|---|
| **Specimens with cut further from surface** | 1802Nmm/mm | 2054Nmm/mm (+14%) |
| **Specimens with cut closer to surface** | 1357Nmm/mm | 1540Nmm/mm (+13.5%) |

**TABLE 6.1** Bending moments per unit width at failure

## 6.5 Discussion

Table 6.1 shows the predictions are both higher than the average experimental results, but they are still within 14%. A possible source of error could be the presence of width direction stresses. Although the specimens were unidirectional and no loads were applied in the width direction, secondary stresses could arise in the width direction due to the anti-clastic bending constraint in the curved section. Although

not thought to be very significant, these stresses might slightly increase the yield zone lengths, making the predictions less unconservative. The value of the resin Poisson's ratio was also an estimate, but upon investigation it was found that the predicted failure loads were very insensitive to its value.

Another assumption was that the cracks started propagating at the same time and grew at the same rate. To calculate the strain energy release rates for a range of these parameters would require much more computational time. Another approach will therefore be presented in a subsequent chapter which overcomes this problem. Firstly, however, the problem of delamination growth in cyclic fatigue will be studied briefly.

# Chapter 7

# Delamination due to Cyclic Loading

## 7.1 Introduction

Composite structures, such as helicopter rotor blades, are often required to withstand a large number of cyclic loads during their working life. Accurately predicting the growth of delaminations in fatigue could therefore reduce the amount of structural testing during design and structural checks during the working life of a component.

In chapter 5 we saw that a fracture mechanics based approach was able to accurately predict the static failure loads of straight specimens in three-point bending. In this chapter we will attempt to predict delamination growth in these specimens when they are subjected to cyclic three-point bending loads.

Bolotin [89] described a theoretical method for predicting the growth of delaminations due to fatigue, based on the Paris equation for fatigue crack propagation in metals. It involved using the cyclic strain energy release rate, $G_f$, which is the difference between the strain energy release rates at the peak and trough loads. Similar equations have been used by O'Brien [46], Lin and Kao [90], and Wisnom et al [91] to fit the experimental delamination growth rates from fatigue tests on composite laminates. Wisnom et al [91] used an equation of the form,

$$\frac{da}{dN} = g.\left(\frac{G_f}{G_c}\right)^h \tag{7.1}$$

to fit experimental data from several types of E glass / 913 epoxy and XAS carbon / 913 epoxy laminates with discontinuous internal plies. Note that "a" is the crack length, N is the number of loading cycles, $G_c$ is the critical strain energy release rate measured from static tests, and g and h are empirical constants. It was seen that the values of g and h for all the specimens were very close. In other words, the normalised delamination rate was almost independent of the material, lay-up, and specimen geometry. Thus, the delamination rate for a wide range of specimen types could be predicted quite accurately from the values of g and h obtained from the fatigue data of a single type of specimen.

Wisnom and Jones [92] reported fatigue tests on several types of specimens. Among them were tests carried out on the specimen shown in figure 5.1, with the cut at a spanwise distance, d, of 5 mm from the central loading point. The peak load during the fatigue tests was equal to half the average experimental static failure load, and the ratio of trough to peak load, $R_f$, was 0.1. The experiments revealed cracks propagating simultaneously from the top left and bottom right of the cut, as in the static tests. The bending stiffness of the specimens was logged against the number of cycles.

In this chapter, the strain energy release rate versus crack length data determined in chapter 5, and the values of g and h from previous tests on simple coupons, will be used to determine the crack growth rate. The crack length corresponding to a particular number of cycles will then be predicted. Using the finite element model, the degradation in bending stiffness with respect to the crack length will also be found. This will be used to predict the stiffness degradation of the beam with respect to the number of cycles. Finally, the prediction will be given alongside two experimental data sets.

## 7.2 Rate of delamination growth with respect to crack length

The first step in predicting the stiffness degradation in fatigue was to obtain the values of the cyclic strain energy release rate, $G_f$, at each increment of crack length and normalise them with the critical strain energy release rate, $G_c$.

Figure 7.1 shows a graph of the total strain energy release rate against the crack length, obtained from the finite element analysis. The applied load per unit width at the central loading roller is 142 N/mm, which corresponds to the peak load during the fatigue tests.

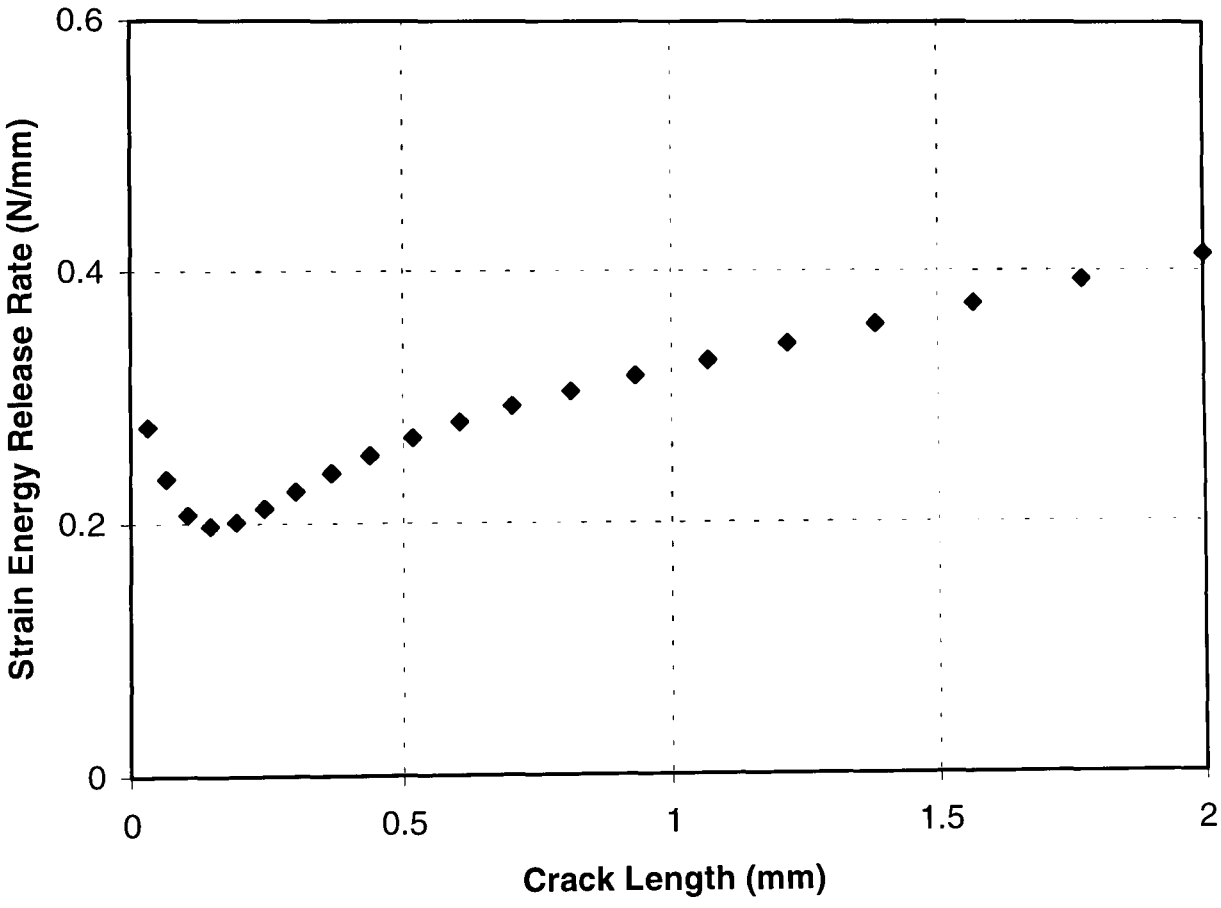


**FIG. 7.1** Strain energy release rate at peak load of fatigue tests

Since the strain energy release rate, G, is proportional to the square of the load, the value of $G_f$ can be found from,

$$G_f = G_{peak}.(1 - R_f^2) \qquad (7.2)$$

where $G_{peak}$ is the value of G corresponding to the peak load.

Figure 5.7 shows that the strain energy release rate is almost entirely mode II, apart from in the first 0.2mm of crack growth where there is a significant mode I portion. A simplistic approach was therefore adopted where $G_f$ was normalised by the value of $G_{Ic}$ up to a crack length of 0.2mm, and was thereafter normalised by the value of $G_{IIc}$.

The next step was to find the rate of delamination growth, da/dN, from the normalised cyclic strain energy release rate, $G_f/G_c$. The delamination growth rate was assumed to follow the relationship in equation (7.1). The values of the empirical constants, h and g, were found to be close to 7.42 and 1.145mm/cycle, respectively [91]. These were substituted into (7.1) along with the values of $G_f/G_c$ at each increment in crack length. This gave the values of da/dN corresponding to crack lengths between 0 and 2mm.

## 7.3 Bending stiffness with respect to number of cycles

From the values of da/dN corresponding to each crack length, it was possible to determine the crack length corresponding to a particular number of cycles, N. Since the increments of crack length, $\Delta a$, were relatively small, the increment in the number of cycles, $\Delta N$, required to increase the crack length by $\Delta a$ could be approximated by,

$$\Delta N \approx \Delta a.\left(\frac{da}{dN}\right)^{-1} \qquad (7.3)$$

where the value of da/dN corresponds to the crack length at the beginning of the increment. Thus, the value of N at a particular crack length was equal to the sum of the values of $\Delta N$ required for all the increments in crack length leading up to that crack length. A graph of a against N can be seen in figure 7.2.

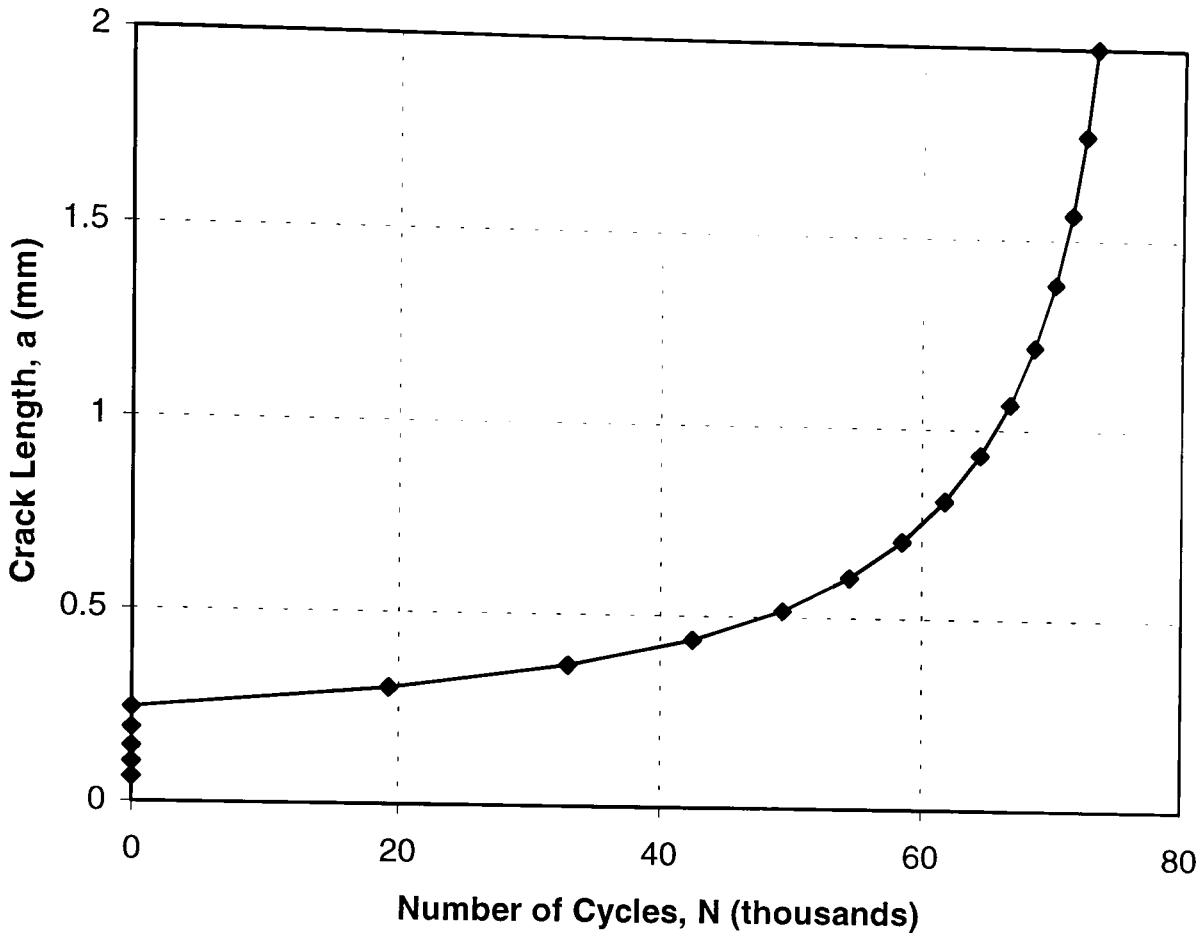


**FIG. 7.2** Predicted crack growth with respect to number of cycles

The above graph has not been plotted on a log scale so that the rapid acceleration of the crack growth can be seen more easily. There is an initial burst in crack propagation due to the significant mode I strain energy release rate, but thereafter the delaminations grow quite slowly until the rapid acceleration occurs.

The bending stiffness of the beam reduced as the crack length increased. At each increment of crack length, the value of the vertical displacement, z, of the point of contact of the central loading roller was obtained from the finite element analysis. For convenience, the value of the applied load, P, divided by the corresponding value of z was used to gauge the stiffness. The values of P / z at each crack length were normalised by the initial value. Finally, a graph of normalised stiffness against N was plotted. During the testing of the specimens, the displacement of the central roller was logged against the number of cycles so it was possible to obtain P / z as a function of N. The degradation in the normalised stiffness from the two tests can be seen alongside the prediction in figure 7.3.

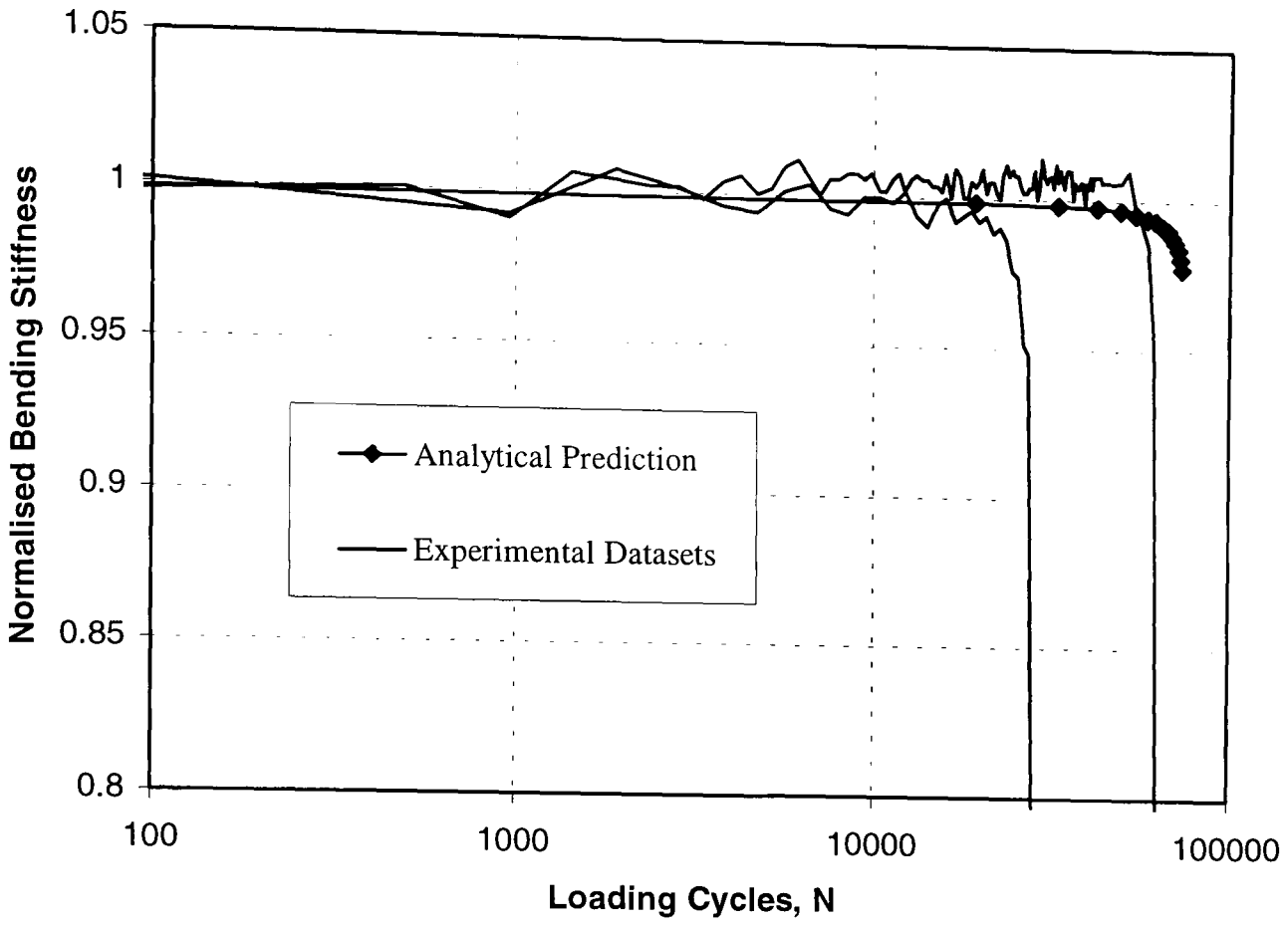


**FIG. 7.3** Degradation in bending stiffness due to delamination in fatigue

## 7.4 Discussion

Figure 7.3 shows that the predicted stiffness remained almost constant up to a certain number of cycles whereupon it suddenly and rapidly reduced. This is exactly what the experimental data show. The number of cycles, N, at which the predicted rapid stiffness drop occurs is close to the two experimental results. The predicted normalised stiffness does not fall below 0.97 because only 2 mm of crack propagation on either side of the cut was modelled. However, one can see from the shape of the curve that the stiffness would continue to fall dramatically if the prediction was continued. Upon further investigation it was found that the value of N at the beginning of the rapid stiffness reduction was quite sensitive to the value of critical strain energy release rate, $G_c$. Since there is always some material variability in composites, such as the fibre volume fraction and voidage, the value of $G_c$ would vary slightly between different specimens. This may be one reason for the relatively high degree of scatter in fatigue tests.

However, the qualitative crack growth behaviour was not sensitive to the value of $G_c$. Therefore, this approach was successful in predicting the manner in which delaminations spread from discontinuous plies in composites under fatigue loading.

In the next chapter we shall return to the problem of delamination failure under static loading.

# Chapter 8

# Predicting Delamination with Interface Elements

## 8.1 Introduction

In chapter 2 we saw that finite element analysis is often employed for predicting failure in tapered laminates. Both stress based methods [12,18] and fracture mechanics methods [72-76,93] have been used to predict static delamination loads in tapered composites. There are drawbacks to both these types of approaches. Due to the stress singularities at the ends of the discontinuous plies the stress based methods are highly dependent on mesh size, or in the case of average or point stress criteria, they involve certain characteristic lengths which do not have a very strong theoretical foundation. Fracture mechanics methods such as the virtual crack closure technique rely on the assumption of an initial defect or crack length. This problem was tackled in chapters 5 and 6. Nevertheless, with the approach adopted there it is still necessary to know beforehand the path of the delamination, and where there is more than one possible delamination site, the propagation rate of each delamination relative to the others. However, the stress based methods are generally good at predicting the initiation of delamination, and fracture mechanics is generally successful at predicting the growth of delamination once an initial crack has been formed.

The approach used in this chapter combines both of the above methods and therefore overcomes their deficiencies. Failure is assumed to occur in the resin rich layers between plies. Special user-defined elements representing the interface between the plies are inserted in the finite element model along any possible delamination path. Local failure initiates when the stress in an element reaches a critical value and then plastic deformation takes place. Although bulk tests of resin often produce brittle failure, plasticity and much higher resin strains have been observed in very localised areas around crack tips [35,94]. It is therefore reasonable to use plasticity theory to model the yielding or damage process in the resin. When a certain amount of plastic work is done, representing the critical strain energy release rate, $G_c$, the element "fails" and is no longer able to bear any load. Thus the initiation and growth of delamination can be simulated in one execution of a finite element code. This approach was first used to simulate delamination in fibre-reinforced composites by Schellekens [95]. The interface element approach was mainly applied to the problem of free edge delamination [96,97] and there was good agreement between the predicted and experimental ultimate failure strains. However, in mixed mode cases the value of $G_c$ was calculated from the ratio between the plastic work in each mode and the uncoupled critical values of the strain energy release rate, $G_{Ic}$ and $G_{IIc}$. This meant it was necessary to know the mode ratio at each integration point before the approach could be applied.

An in depth description of the interface approach was given by Corigliano [98]. He used interface elements to predict the load - displacement response of a double cantilever beam test (pure mode I delamination), however, there was very little experimental verification. The value of $G_c$ was found to be the most important parameter of the interface model.

Hellweg [99] also used interface elements to predict the load - displacement response of a DCB test. There was good agreement with experimental data. Mixed-mode failure was simulated in "overlap" specimens as well, and the failure loads correlated reasonably well with experimental results. The interface element was later used to simulate delamination in a mixed-mode delamination test [100]. Cui and Wisnom [101] applied a simple type of interface element to predict pure mode II delamination

in specimens under three-point bending and specimens with discontinuous central plies. The results compared well with the experimental data. The same type of simple interface element was used by Wisnom [102] to predict mode II failure in specimens under three-point bending which contained initial cracks of various lengths. In contrast to linear-elastic fracture mechanics, the interface element approach predicted failure loads very close to the experimental results at all crack lengths.

All of the interface elements described above have a sudden discontinuous change in stiffness when the stress reaches the critical value. In this chapter, an interface element is designed which has a smooth transition between linear elastic and plastic behaviour. This means fewer iterations are needed during the finite element procedure. The element is also able to handle changes in mode ratio which occur anywhere between initial loading and total failure of the element. These interface elements are then used to predict the static failure loads of the specimens with discontinuous plies which were analysed in chapters 5 to 7. In each case there are several possible delamination sites and both mode I and mode II damage is present. The use of interface elements in solving multiple mixed-mode delaminations has not been seen in the current literature, even though they possess an advantage over traditional fracture mechanics approaches in such situations.

## 8.2 Description of interface element

The stress-strain behaviour of the interface element is modelled using plasticity theory. The main plasticity equations that were used will be explained first of all. Then an account of how the theory was implemented into the finite element method will be given.

Strain can generally be divided into an elastic, or recoverable component, $\varepsilon^e$, and a plastic, or permanent component, $\varepsilon^p$. The total strain, $\varepsilon$, is thus,

$$\varepsilon = \varepsilon^e + \varepsilon^p \tag{8.1}$$

If stress is plotted against total strain, the slope of the curve at a particular point is called the current tangent modulus, T. If stress is plotted against the elastic component of strain, the slope will be the elastic modulus, E. If stress is plotted against the plastic component of strain, the slope is called the plastic modulus, H. The relationship between T, E and H is as follows:

$$1 / T = 1 / E + 1 / H \tag{8.2}$$

The above equation shows that H can be ignored when it is much higher than E, but the tangent modulus approaches the plastic modulus as H goes to zero. This means a smooth transition between the initial high elastic stiffness of a material and perfectly plastic or work softening behaviour can be achieved by gradually reducing the value of H.

The Prandtl-Reuss equations are often used to define the relationship between the increment in plastic strain and the stress. They can be written in the following form:

$$\frac{d\varepsilon_x^p}{s_x} = \frac{d\varepsilon_y^p}{s_y} = \frac{d\varepsilon_z^p}{s_z} = \frac{d\gamma_{xy}^p}{\tau_{xy}} = \frac{d\gamma_{yz}^p}{\tau_{yz}} = \frac{d\gamma_{xz}^p}{\tau_{zx}} = d\lambda \tag{8.3}$$

where $d\lambda$ is a positive scalar, s is the deviatoric normal stress, and $\tau$ and $\gamma$ are the shear stress and shear strain, respectively. If we assume the yield function of the material to be that of von Mises then,

$$d\lambda = \frac{3\overline{d\varepsilon}^p}{2\sigma_{VM}} = \frac{3d\sigma_{VM}}{2H\sigma_{VM}} \tag{8.4}$$

where $\sigma_{VM}$ is the equivalent von Mises stress and $\overline{d\varepsilon}^p$ is the equivalent plastic strain increment. A total stress - strain relationship can be found by combining (8.3) and (8.4) with the elastic stress - strain relationship (Hooke's law). Yamada et al [103] derived this stress - strain relationship and presented it in a useful matrix form. Later,

Chakrabarty [104] gave the relationship for the case of plane stress in the following format:

$$\begin{Bmatrix} d\sigma_x \\ d\sigma_y \\ d\tau_{xy} \end{Bmatrix} = \frac{2G}{C} \begin{bmatrix} (1+\nu)\frac{s_y^2}{\sigma_{VM}^2} + 2B & -(1+\nu)\frac{s_x s_y}{\sigma_{VM}^2} + 2\nu B & -\frac{(s_x + \nu s_y)\tau_{xy}}{\sigma_{VM}^2} \\ -(1+\nu)\frac{s_x s_y}{\sigma_{VM}^2} + 2\nu B & (1+\nu)\frac{s_x^2}{\sigma_{VM}^2} + 2B & -\frac{(s_y + \nu s_x)\tau_{xy}}{\sigma_{VM}^2} \\ -\frac{(s_x + \nu s_y)\tau_{xy}}{\sigma_{VM}^2} & -\frac{(s_y + \nu s_x)\tau_{xy}}{\sigma_{VM}^2} & \frac{C}{2} - (1-\nu)\frac{\tau_{xy}^2}{\sigma_{VM}^2} \end{bmatrix} \begin{Bmatrix} d\varepsilon_x \\ d\varepsilon_y \\ d\gamma_{xy} \end{Bmatrix}$$

..... (8.5)

where G is the shear modulus, ν is the Poisson's ratio and,

$$B = \frac{H}{9G} + \frac{\tau_{xy}^2}{\sigma_{VM}^2} \qquad (8.6)$$

$$C = \tfrac{2}{3}(1-\nu)\left(1 + \frac{H}{3G}\right) - (1-2\nu)\frac{s_z^2}{\sigma_{VM}^2} \qquad (8.7)$$

and for plane stress,

$$\sigma_{VM}^2 = 3(s_x^2 + s_x s_y + s_y^2 + \tau_{xy}^2) \qquad (8.8)$$

For the present analyses, x, y and z can be interpreted as directions tangential to the interface (1), normal to the interface (3), and through the width (2), respectively.

The interface element consists of two coincident nodes, one on either side of the crack interface, which are effectively connected by non-linear springs. Load is transferred between the nodes in directions both tangential and normal to the interface. Similarly to the surrounding elements in the model, the interface element assumes plane stress. It also assumes the normal strain in the tangential direction to be zero. For the specimens analysed in this study, both these simplifications have very little effect on the results. The specimens are unidirectional so the width direction Poisson's ratio is close to the pure resin Poisson's ratio, and once yielding

begins the axial strains in the resin rich layer are negligible compared to the through-thickness normal and shear strains.

The interface element was created by using a user-defined element, available in ABAQUS [59]. A computer programme (see appendix) was written in Fortran 77 to describe its behaviour. The code was inserted into the finite element input file and was executed automatically whenever the solution procedure required information about an interface element. The primary function of the code is firstly to read in the stresses in the element and the tangent stiffness matrix corresponding to the end of the previous load increment, and the increments in the nodal displacements during the current load increment; then to calculate the increments in stresses using (8.5); and finally to send out the stresses and nodal forces corresponding to the end of the current load increment. The tangent stiffness matrix is also given at the end of every load increment to enable the solution procedure to calculate the nodal displacements in the next increment. Moreover, the code reads in and updates the components of plastic work and H. Refer to figure 8.1 for a flowchart of the code.

After the increments in nodal displacement are read in they are translated into components normal and tangential to the local interface. The relative displacements of the nodes on either side of the interface are used to calculate the increments in strain. The thickness of the resin rich layer was assumed to be 0.01mm when calculating the strains. This value was low enough for the relative nodal displacements to be negligible while the interface elements were behaving elastically. The code then checks to see if the plastic work reached its critical value in the previous increment. If it did the element has "failed" and has zero stiffness. Otherwise the code goes on to check if the element is unloading.

For a material which may be work softening, unloading should be checked by referring to the increments in strain rather than the increments in stress. Chakrabarty [104] states the following condition can be used to check for unloading:

$$n_{ij} d\varepsilon_{ij} < 0 \qquad (8.9)$$

where i and j are suffixes which can represent either 1, 2 or 3, and $n_{ij}$ is the outward drawn unit normal to the yield surface at the current stress point. Since we are using the Prandtl-Reuss equations we have,

$$n_{ij} = \sqrt{\frac{3}{2}}\left(\frac{s_{ij}}{\sigma_{VM}}\right) \tag{8.10}$$

where $s_{ij}$ is the deviatoric stress corresponding to directions i and j. So for plane stress and zero strain in the tangential direction there will be unloading when,

$$s_2 d\varepsilon_2 + s_3 d\varepsilon_3 + \tau_{13} d\gamma_{13} < 0 \tag{8.11}$$

Note that even if the through-width stress is zero, the through-width deviatoric stress, $s_2$, is generally not zero. If the element is unloading, the terms in the tangent stiffness matrix are set to those corresponding to Hooke's law. Otherwise the terms in the tangent stiffness matrix are found from (8.5). The same matrix is used during the entire strain history. Simply by changing the value of H, the element is made to behave either elastically or plastically with either work hardening or work softening. Referring to (8.2) one can see that the tangent modulus will be within 1% of the elastic modulus when H is 100 times greater than the elastic modulus, and the tangent modulus will equal zero when H equals zero. Thus, the following function of H was used:

$$H = 100.E.(1 - \tau_{VM} / \tau_Y)^2 \tag{8.12}$$

where E is the Young's modulus, $\tau_Y$ is the shear yield stress, and $\tau_{VM}$ is the equivalent von Mises stress divided by $\sqrt{3}$. Shear stresses were used rather than normal stresses for convenience since the shear yield stress of the material was available. The form of the above equation was not based on any physical phenomena, and was chosen simply to obtain a smooth transition between the initial high stiffness of the element and perfectly plastic behaviour.

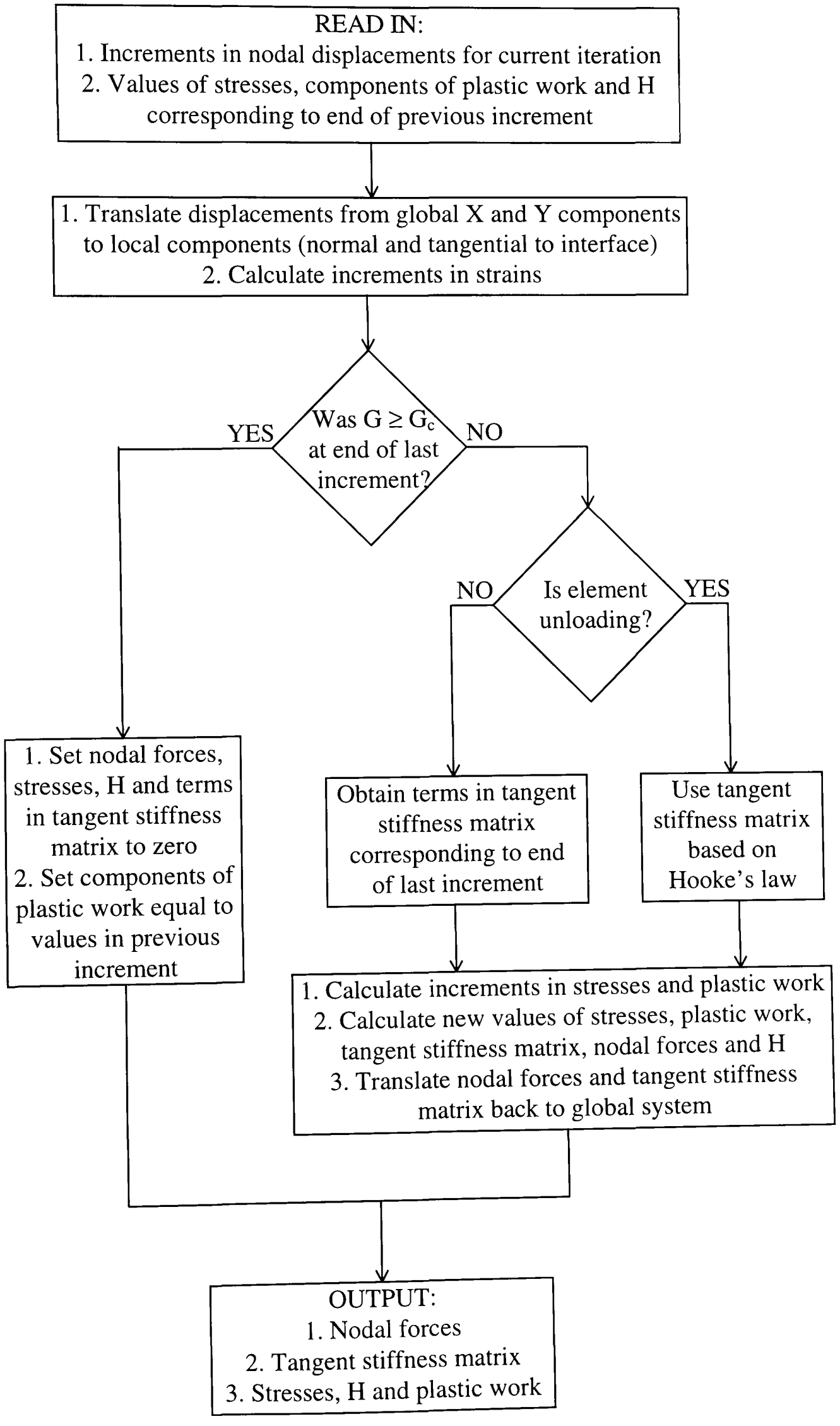


**FIG. 8.1** Flowchart of interface element code

The next step in the code is to calculate the increments in stresses and plastic work. These are used to update the values of the stresses (and hence nodal forces), plastic work, H, and finally the terms in the tangent stiffness matrix. The last step in the code is to translate the nodal forces and tangent stiffness matrix from the local co-ordinate system to the global co-ordinate system which the solution procedure works in.

The plastic work is divided by the area of interface surface which the element represents to make it comparable with the critical strain energy release rate or fracture energy, $G_c$. Furthermore, it is separated into mode I and mode II components. The increments in mode I and mode II plastic work divided by interface surface area, $\Delta G_I$ and $\Delta G_{II}$ respectively, are calculated as follows:

$$\Delta G_I = \left(\sigma_3' + \Delta\sigma_3 / 2\right).\Delta\varepsilon_3^p.t_r \qquad \text{for } \sigma_3 > 0$$

$$\Delta G_I = 0 \qquad \text{for } \sigma_3 < 0 \qquad (8.13)$$

$$\Delta G_{II} = \left(\tau_{13}' + \Delta\tau_{13} / 2\right).\Delta\gamma_{13}^p.t_r \qquad (8.14)$$

Where $\sigma_3'$ and $\tau_{13}'$ are the through-thickness normal and shear stresses at the end of the previous load step, $\Delta\tau_{13}$, $\Delta\sigma_3$, $\Delta\gamma_{13}^p$ and $\Delta\varepsilon_3^p$ are the increments in stress and plastic strain during the current load step, and $t_r$ is the assumed thickness of the resin rich layer. The above equations assume a linear variation of the stress between each load increment. Notice that the increment in mode I plastic work is set to zero when there is through-thickness compression. This prevents the interface elements from failing under pure through-thickness compression. This assumption was also made by Schellekens [95].

The same mixed mode strain energy release rate criterion is used to predict failure:

$$G_{norm} = G_I / G_{Ic} + G_{II} / G_{IIc} = 1 \qquad (8.15)$$

where $G_{Ic}$ and $G_{IIc}$ are the mode I and mode II critical strain energy release rates, respectively. If the value of $G_{norm}$ reaches or exceeds 1, the element will fail and no longer carry any loads. However, since the code only checks to see if the element has failed at the beginning of each routine (see figure 8.1), the element will still support loads at the end of the current increment. This is a necessary evil for the sake of improving solution convergence. Thus, the size of the load increment is made small enough so that the elements always fail with the plastic work within about 1% of the critical value. The value of $G_{norm}$ at the end of the increment is passed on to the next increment, along with the updated stresses, terms in the tangent stiffness matrix and value of H.

The material properties of the interface element correspond to those of the resin, which in this case is 913 epoxy. The elastic properties of the resin can be measured from bulk tests but the stress - strain behaviour beyond the elastic limit is difficult to obtain because of problems of premature failure of the specimens. Therefore, we have made assumptions about how the interface behaves after yielding. Two types of post yield or damage behaviour were modelled in the interface element. The first was perfectly plastic up to total failure, such as in the interface element which Cui and Wisnom [101,102] used. The second type of behaviour was similar to that modelled by Schellekens [96] and Hellweg [99], in that after yielding, the load which the element carried was gradually reduced so that when the plastic work had reached its critical value the stresses were equal to zero. Refer to figure 8.2 for a plot of shear stress against relative nodal displacement for monotonically loaded elements of both types. The strain path for unloading is also given.

The first type was easy to model since it was just necessary to set H equal to zero once $\tau_{VM}$ had stabilised to $\tau_Y$. However, the second "work softening" type of behaviour was more difficult to model. It is important for work softening not to commence too soon, otherwise the value of $\tau_{VM}$ may never reach $\tau_Y$. Thus to be safe, work softening was only started once the value of $G_{norm}$ had reached 0.1, at which point the value of $\tau_{VM}$ had completely stabilised to $\tau_Y$. The amount of work softening required to reduce the stresses to zero by the time $G_{norm} = 1$ varies depending on the mode ratio. Hence the following function of H had to be used:

$$H = H_{II} + H_I.\Delta G_I / (\Delta G_I + \Delta G_{II}) \qquad (8.16)$$

where $H_I$ is the value of H required to cause the stresses to be zero when $G_{norm} = 1$ in pure mode I loading, and $H_{II}$ is the value of H required in pure mode II loading. The values of $H_I$ and $H_{II}$ are constants for a particular type of interface element, and can easily be found before the main analysis. For example, the value of $H_I$ is determined by applying a gradually increasing pure mode I deformation to an interface element until $G_I = G_{Ic}$ and checking the final stress. Iteration is then carried out to obtain the value of H which results in zero stress when $G_I = G_{Ic}$.

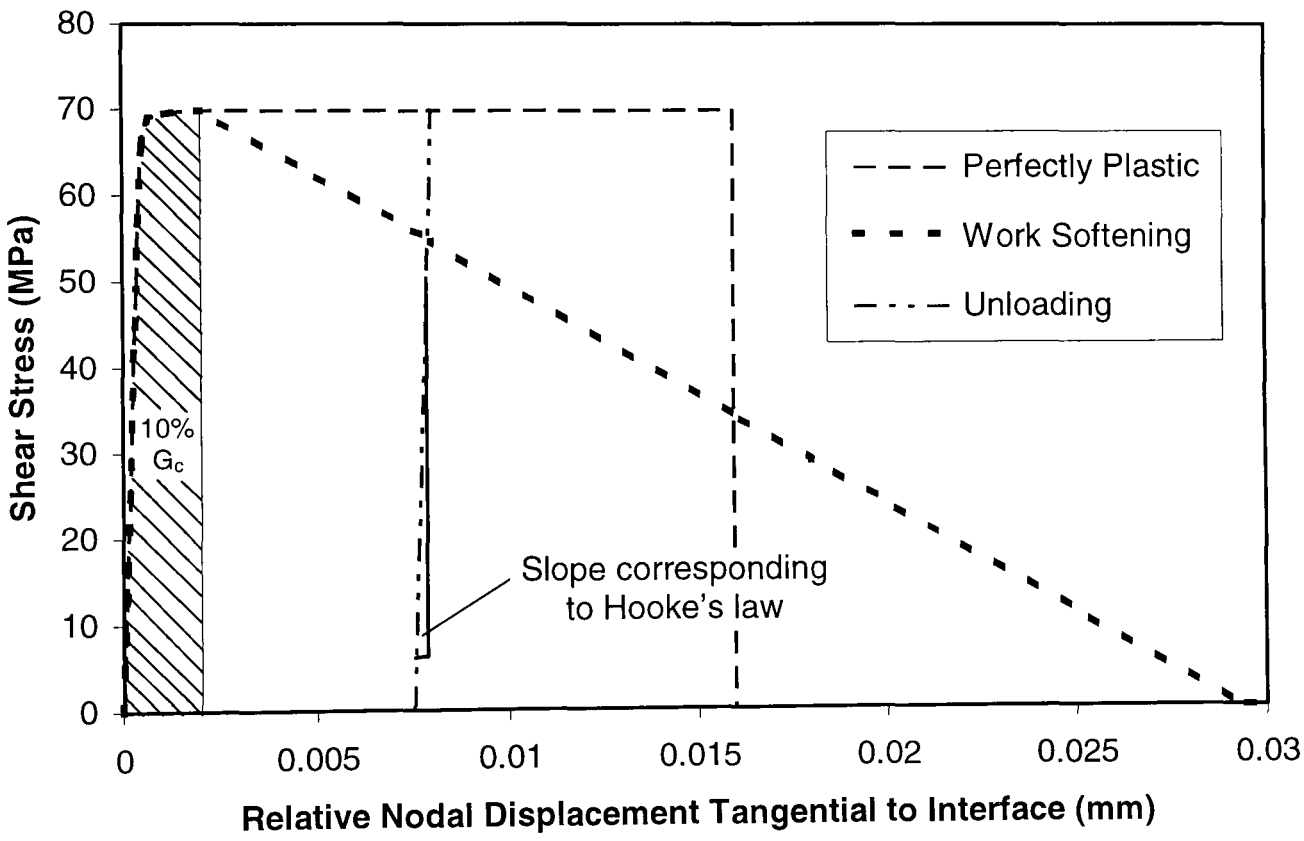


**FIG. 8.2** Stress-strain response of interface element in pure shear

## 8.3 Predictions from finite element analysis

The finite element models created for the analyses in chapters 5 and 6 were used again. However, interface elements were placed between the coincident nodes instead of spring elements. The material properties of the resin and the values of $G_{Ic}$ and $G_{IIc}$ used to define the behaviour of the interface elements were the same as the ones assumed previously in this thesis.

The finite element models were solved in ABAQUS using the standard Newton-Raphson solution technique. The load was divided into about 50 increments to ensure all the interface elements followed the stress-strain curve closely, and to allow for any unloading or changes in mode ratio. Since the specimens did not have significantly large deformations a small displacement analysis was thought to be adequate. Convergence was generally quite good with an overall average of 4 or 5 iterations per increment. However, the increments in load had to be reduced as the failure load was approached and convergence became more difficult. After the ultimate load of the model had been reached convergence was not possible with the standard solution method. This was not a problem since the aim was to predict the failure loads, not the response of the structure after delamination. Separate analyses were done using interface elements with either a perfectly plastic response or a work softening response, as described previously. The predicted failure loads and bending moments per unit width for both types of interface element are given in table 8.1 along with the average experimental values.

Some of the finite element analyses were repeated using displacement control and the Riks solution technique. There was no difference in the predicted failure loads.

| | Straight specimen, d = 5mm | Straight specimen, d = 15mm | Curved specimen, cut plies further from surface | Curved specimen, cut plies closer to surface |
|---|---|---|---|---|
| Experimental averages | 284.0 N/mm | 432.4 N/mm | 1802 Nmm/mm | 1357 Nmm/mm |
| Predictions assuming perfectly plastic response | 277.3 N/mm | 435.3 N/mm | 2535 Nmm/mm | 1675 Nmm/mm |
| Percentage difference | -2.4% | +0.7% | +41% | +24% |
| Predictions assuming work softening response | 244.0 N/mm | 378.0 N/mm | 2092 Nmm/mm | 1490 Nmm/mm |
| Percentage difference | -14% | -13% | +16% | +10% |

**TABLE 8.1** Loads and bending moments at failure (per unit width)

## 8.4 Discussion

By comparing the predicted failure loads with the experimental failure loads in table 8.1 we can see the predictions using "perfectly plastic" interface elements are very good for the straight specimens but unconservative for the curved specimens. On the other hand, the predictions using the "work softening" interface elements are reasonable for all four types of specimens. A possible source of error could be the use of the von Mises yield criterion for modelling the behaviour of the interface elements. This was done for simplicity since the corresponding incremental stress - strain relationship for plane stress in matrix form was already available [103,104]. However, the von Mises yield criterion was developed for use with metals and is not influenced by the hydrostatic stress.

Using Raghava's yield criterion [14] instead of von Mises' would have the effect of lowering the yield stress in situations where there is significant hydrostatic tension, such as in the curved specimens. The analysis was therefore repeated on the curved model with the cut further from the surface, using a value of yield stress 10% lower then the original. The predicted failure load dropped by 5% with the perfectly plastic interface elements and 4% with the work softening interface elements. Thus, using Raghava's criterion instead of von Mises' would make the predictions for the curved specimens less unconservative. Some of the damaged interface elements in the straight specimen models were under through-thickness compression. Raghava's criterion therefore, could be expected to give slightly higher predictions for the straight specimens.

Finally, we must not overlook the possibility of differences in $G_{Ic}$ and $G_{IIc}$ between specimens with different geometries. Indeed, it has been shown that thicker resin rich layers between plies can result in higher values of $G_{Ic}$ and $G_{IIc}$ [105-107]. The average measured thickness of the straight specimens was 4.33mm, compared to 4.06mm for the curved specimens with the cut closer to the surface and 4.15mm for the curved specimens with the cut further from the surface. However, all the specimens had the same number of plies, so the differences in thickness are due to

different amounts of resin flow during curing. Thus, the straight specimens may have thicker resin rich layers between plies compared to the curved specimens, and therefore higher relative fracture toughnesses. This would explain some of the difference between the predictions for the straight and curved specimens, which can also be seen in chapters 5 and 6.

To predict the locations of the delaminations, the extent of damage in each interface element was looked at just prior to catastrophic failure. The value of the normalised strain energy release rate, $G_{norm}$, was plotted against the distance along the interface from the cut for each of the possible delamination sites. An interface element is completely damaged when its value of $G_{norm}$ reaches 1. The graphs corresponding to the interfaces above and below the cut can be seen in figure 8.3 for the straight specimen with d = 5mm, and in figure 8.4 for the curved specimen with the cut further from the surface. The graphs corresponding to the other straight and curved specimens are qualitatively similar to figures 8.3 and 8.4, respectively. Note that each data point on the graphs refers to the value of $G_{norm}$ for a particular interface element.

Referring to figure 8.3 we can see that there are large damage zones along the interfaces at the top left and bottom right of the cut. Thus, delamination would be expected to occur in these two locations. This is what happened during the tests. It is interesting to note that some of the elements along the interfaces at the top right and bottom left of the cut start unloading before catastrophic failure. This shows the importance of having unloading capabilities in the interface element even when the structure is under monotonic loading. There is little difference between the perfectly plastic interface elements and the work softening interface elements, except that some fully formed cracks develop before unstable crack propagation with the perfectly plastic interface elements. These are indicated by the solid square symbols. However, the work softening elements nearest to the crack tips are almost completely damaged prior to catastrophic failure. Delamination in the curved specimens occurred on both sides of the cut but was more dominant along the top interface. This was predicted by the analysis, as can be seen in figure 8.4. As with the straight specimen model, the perfectly plastic elements were more damaged prior to catastrophic failure compared to the work softening elements.

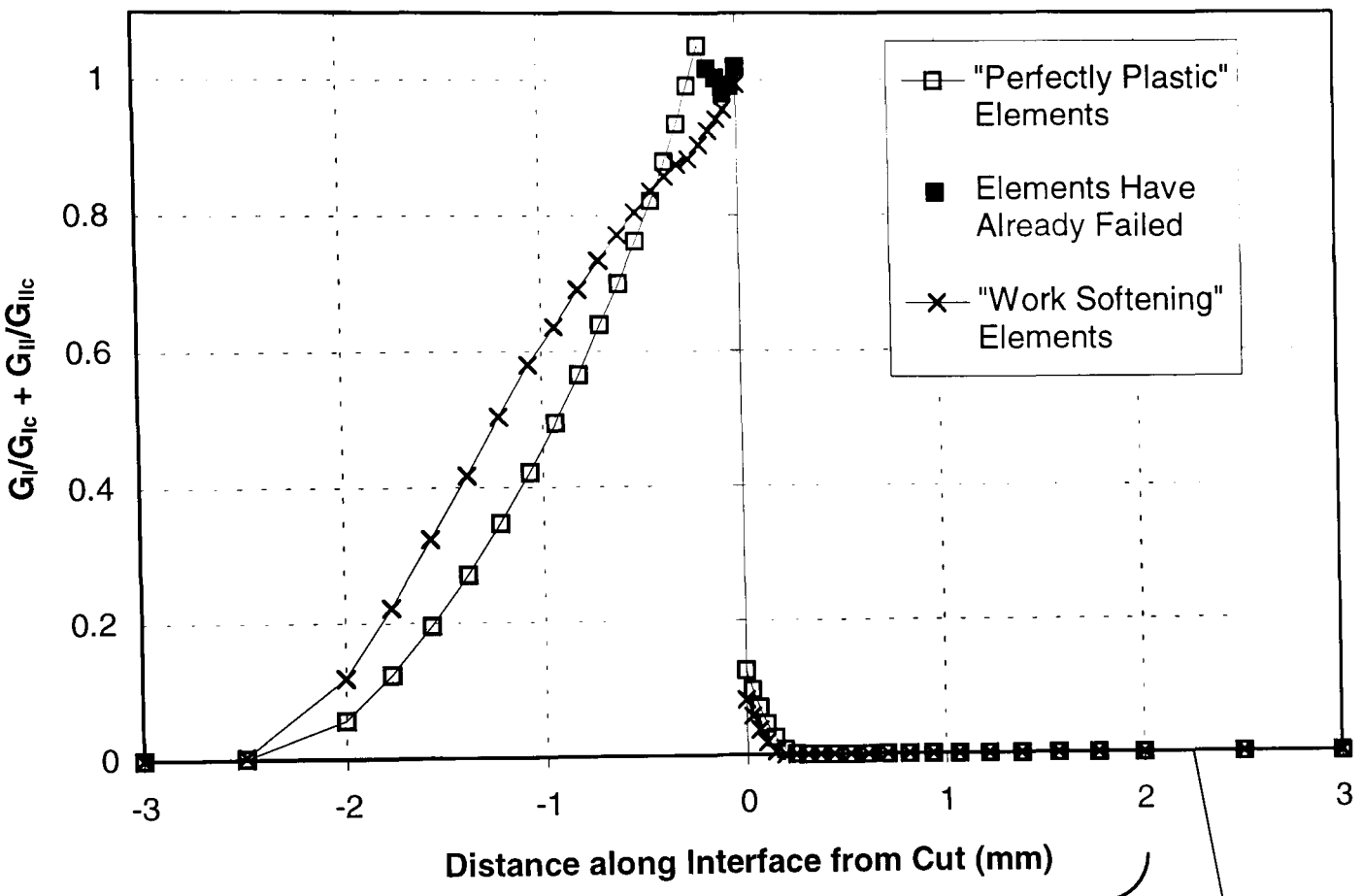


**a).** Top Interface

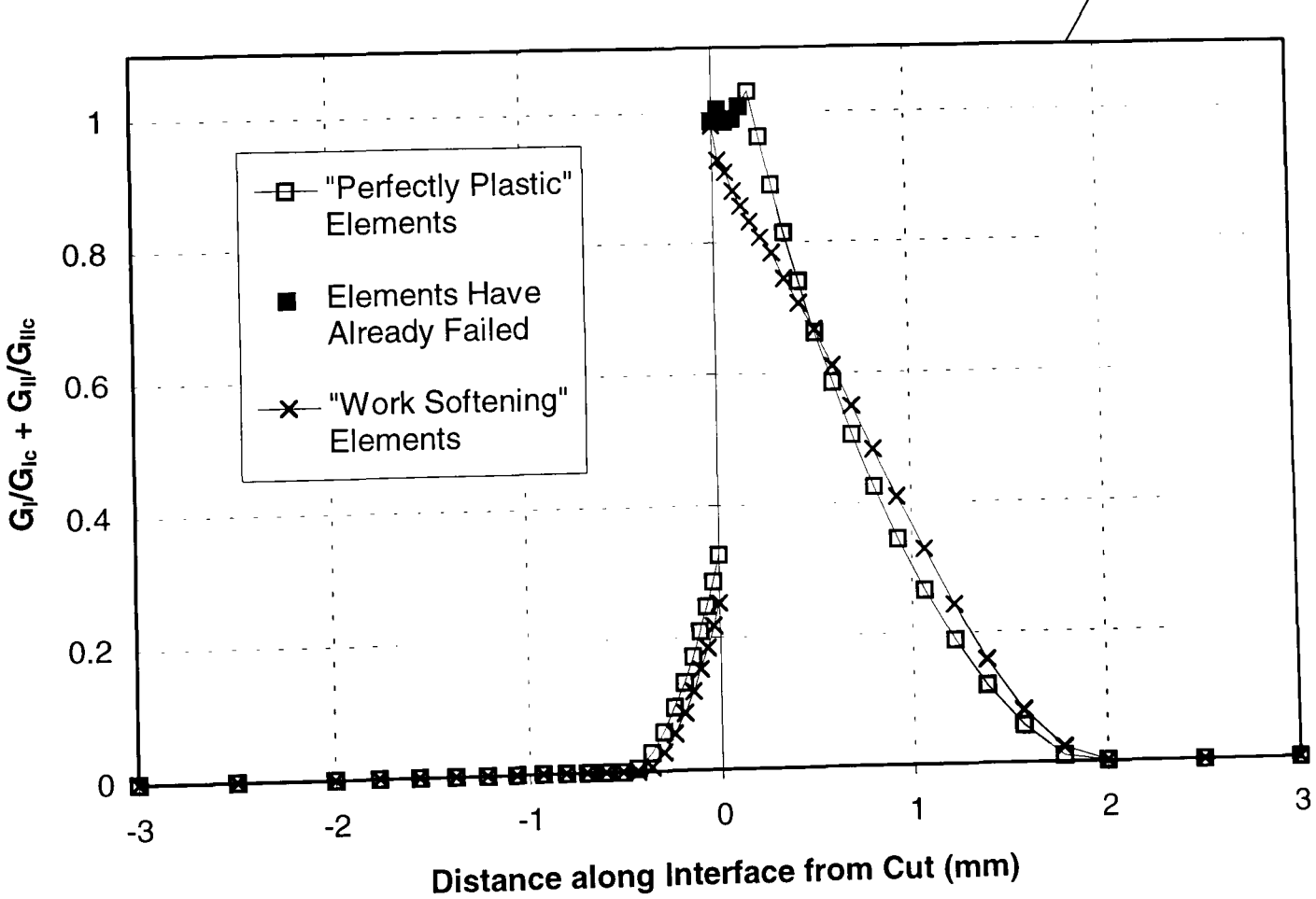


**b).** Bottom Interface

**FIG. 8.3** Distribution of plastic work in straight specimen with d = 5mm, just before unstable crack growth

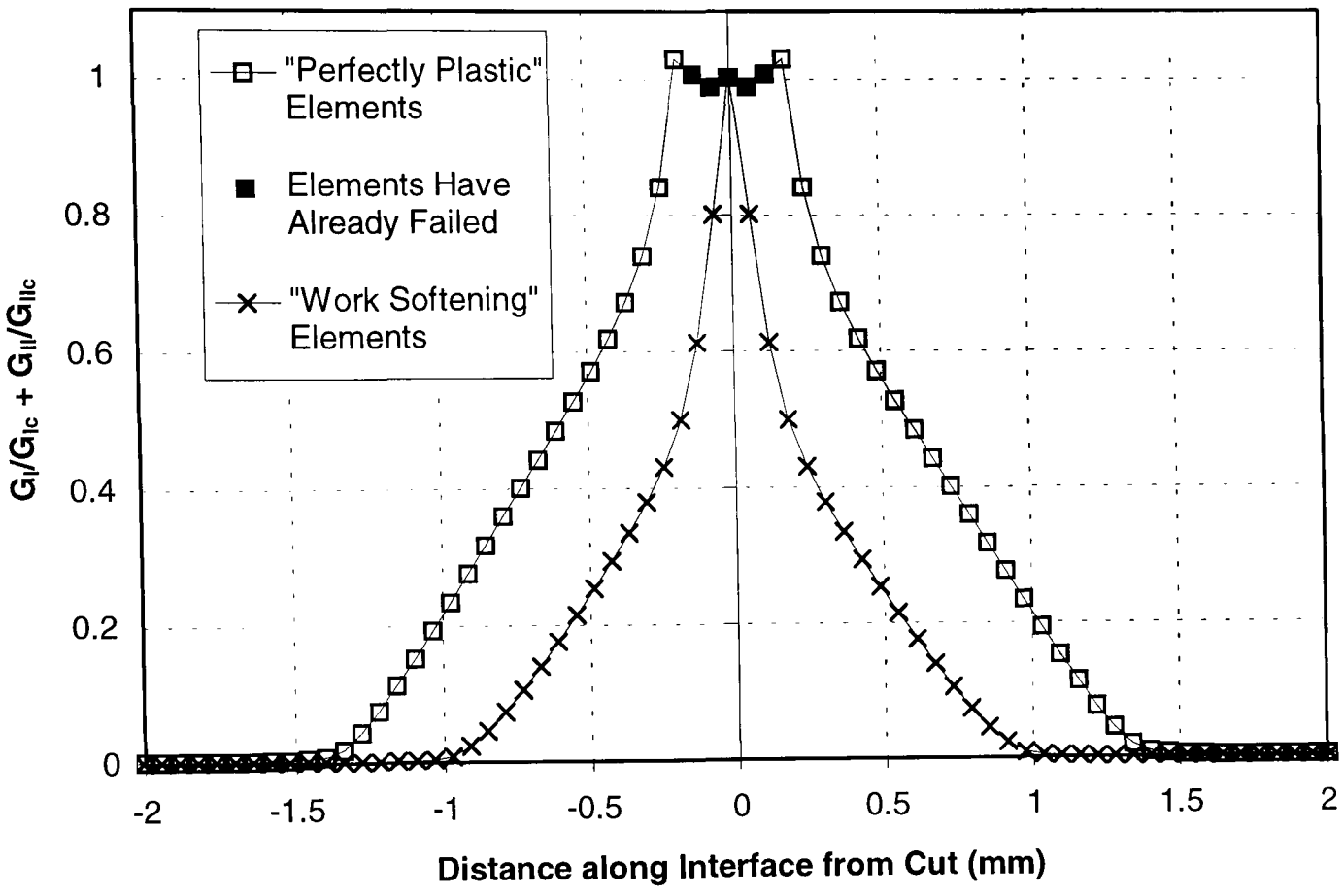


**a).** Top Interface

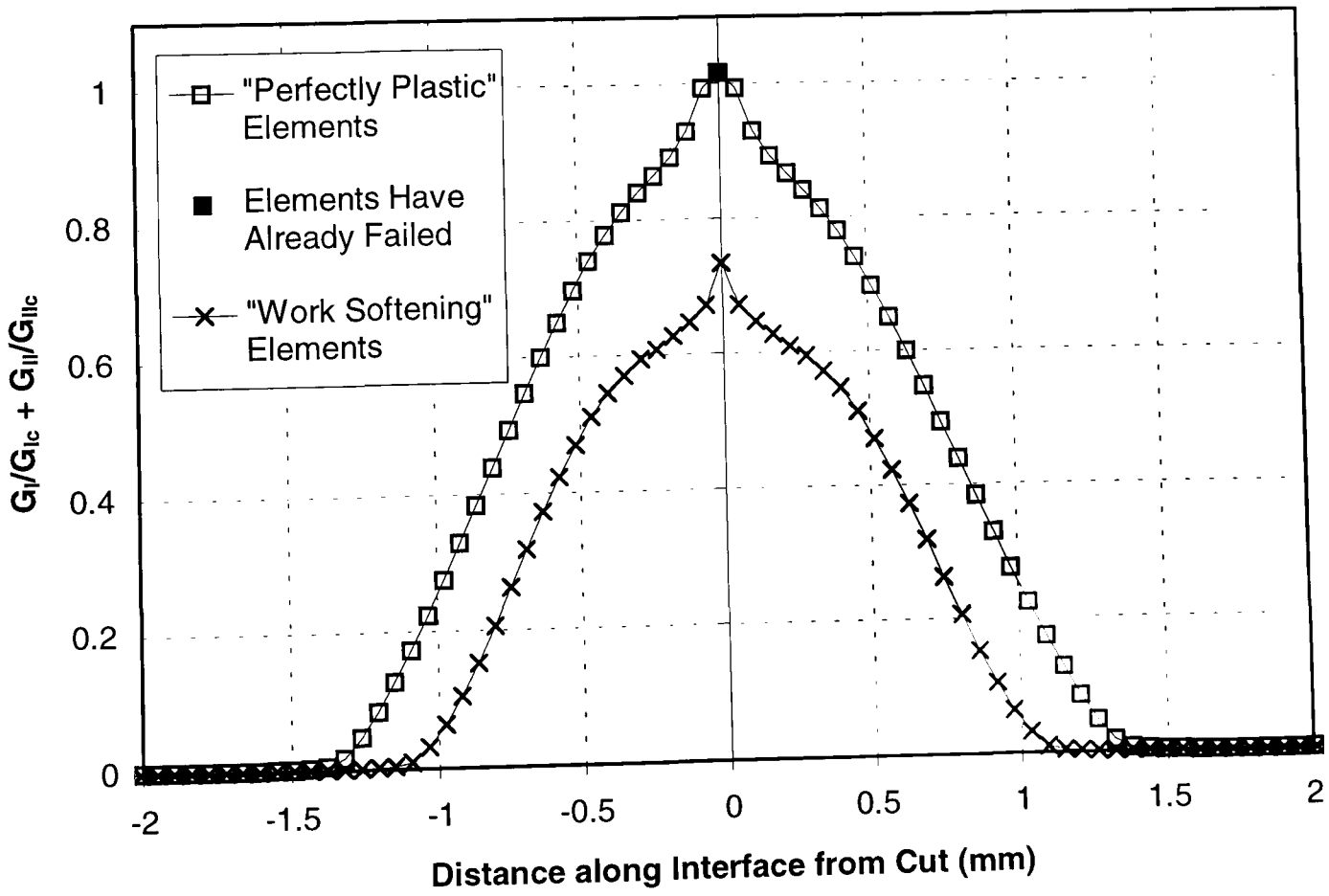


**b).** Bottom Interface

**FIG. 8.4** Distribution of plastic work in curved specimen with cut further from surface, just before unstable crack growth

As explained earlier, if a perfectly plastic element has a value of $G_{norm}$ less than 1 at the end of one increment, then it will still support loads in the next increment even if the value of $G_{norm}$ surpasses 1. Thus, the load increment size was made small enough so that the elements always failed with the plastic work within about 1% of the critical value. However, when crack propagation became unstable this was difficult to maintain since the loads supported by elements which reached failure in the previous increment had to be transferred to the adjacent elements, which were themselves close to failure. This "domino effect" resulted in elements having a value of $G_{norm}$ significantly higher than 1 at the end of an increment, even when the size of the load increment was very small. This can be seen in figures 8.3 and 8.4, where the unfailed perfectly plastic elements adjacent to the completely failed elements have a value of $G_{norm}$ noticeably higher than 1. This is not a problem in the present investigation since it does not affect the predicted failure loads of the specimens.

The above situation does not arise with the work softening elements as they have already lost most of their load carrying capability when complete failure occurs, and thus the adjacent elements do not undergo a sudden increase in strain. If, however, a substantially large increment in strain did occur in a work softening element when it was close to complete failure, there could be another problem. The increment in stress calculated by (8.5) could be large enough to result in a load reversal, i.e., the stress - strain curve would cross the strain axis. A subroutine was therefore inserted into the code which brought the stress to zero if this occurred.

The importance of the interface element being able to handle changes in mode ratio during its plastic deformation or damaging process can be seen in figure 8.5, where the ratio between mode I and mode II plastic work in the elements along the interfaces of one of the specimens is plotted at two points in time. One will notice that the elements very near the cut have a significantly higher proportion of mode I damage just prior to catastrophic failure, compared to when the load is half the ultimate value. The reverse is seen in the elements slightly further away from the cut.

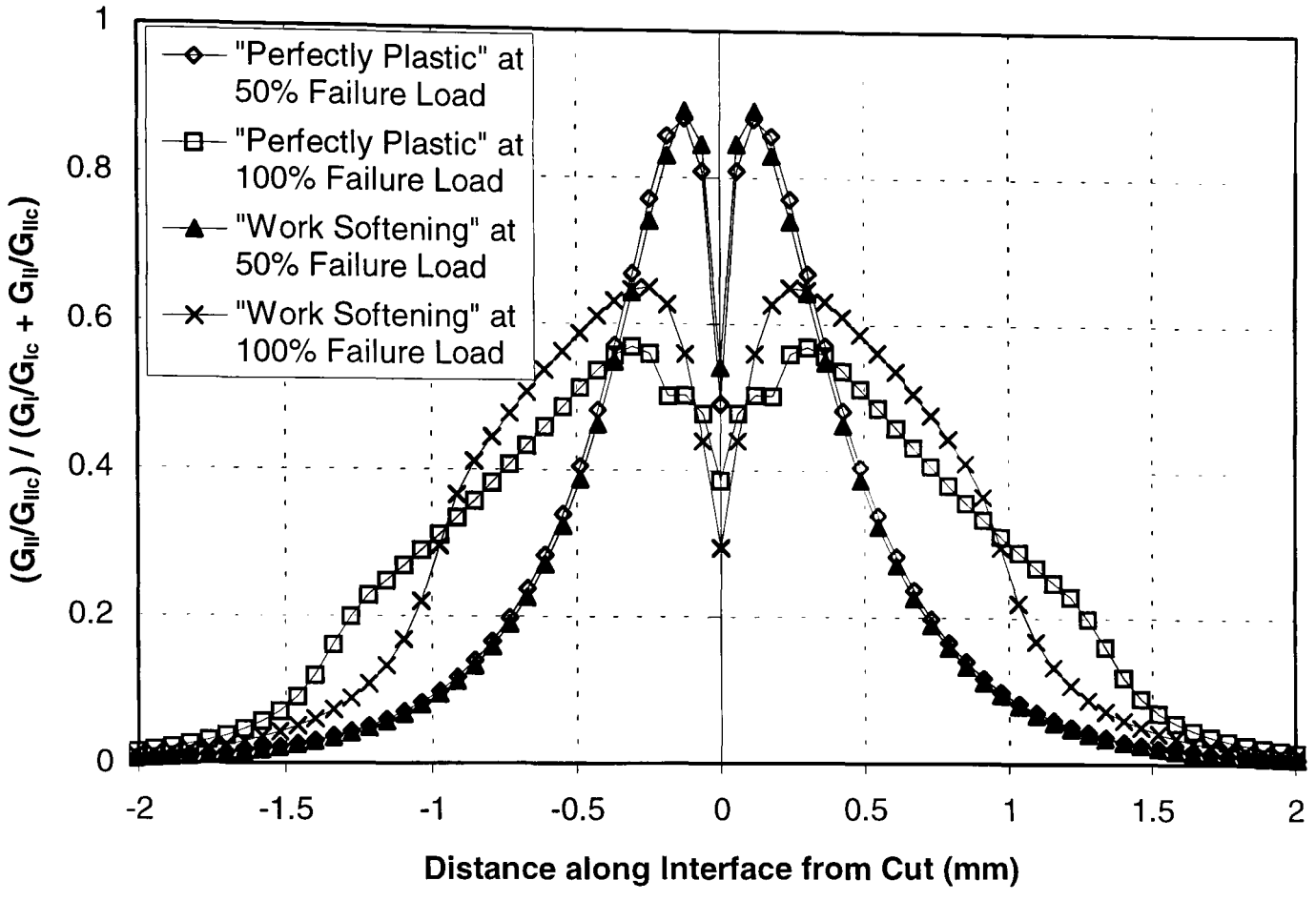


**a).** Top Interface

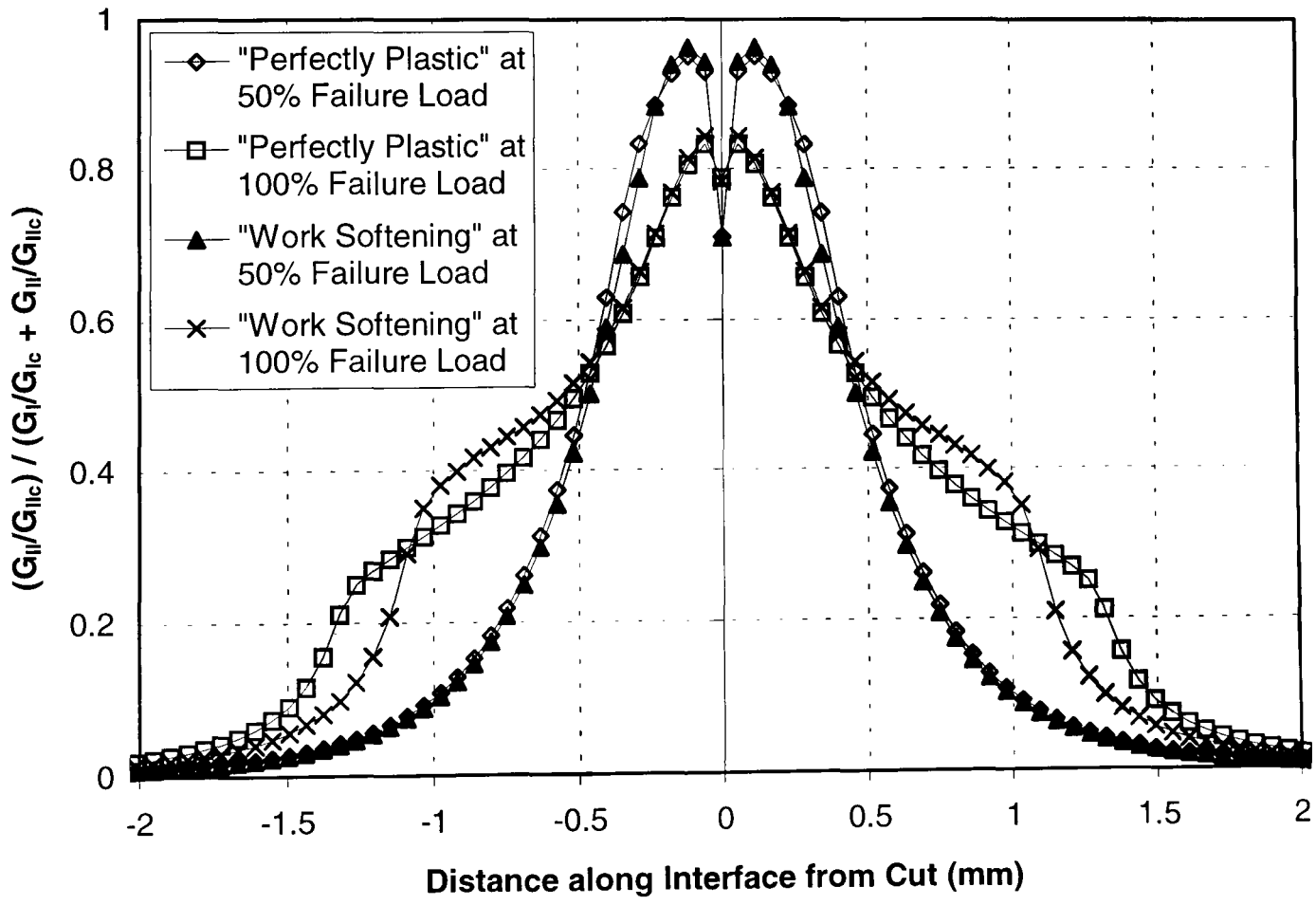


**b).** Bottom Interface

**FIG. 8.5** Variation of mode ratio along delamination sites in curved specimen with cut further from surface

Note that the total components of damage were used to plot the mode ratios, hence the change in mode ratio would be much greater if we considered the incremental components of damage. Thus an element may start yielding in predominantly shear and end up yielding mostly in tension, or vice versa. Figure 8.5 also shows that there is a small difference in the mode ratio between the two types of interface element. The graphs correspond to the curved specimen with the cut further from the surface. The elements near the cut fail by a mixture of mode I and mode II. The mode II component is due to the axial loading at the cut, and the mode I component is due to the overall through-thickness tension caused by the curvature. Hence, the mode II component is higher closer to the cut and nearer the surface of the specimen where the axial loading is higher; and the mode I component is higher along the top interface where the through-thickness tensile stress is higher.

The graphs corresponding to the other type of curved specimen were similar to the ones in figure 8.5 except the ratio of mode II to mode I was generally higher since the cut was closer to the surface. The damage in the interface elements in the straight specimens was almost entirely mode II, except for the elements within 0.05mm from the cut where there was significant mode I damage due to high local through-thickness tension caused by the interaction of the overall shear stress and the cut.

## 8.5 Conclusions

An interface element has been developed to model the resin rich layers between plies, using plasticity theory. The element is able to behave elastically, yield under a changing mode ratio with either a perfectly plastic or work softening type response, and finally fail when a certain amount of plastic work has been done. The element has been inserted into four finite element models of composite specimens which failed by multiple delaminations under various combinations of mode I and mode II.

Assuming a perfectly plastic post yield response, very good predictions have been made of the failure loads of straight specimens, where the delamination is mostly mode II. However, unconservative predictions were made for curved specimens with a significant proportion of mode I. Reasonably good failure load predictions were made for all the specimens when the interface elements had a work softening type response. In all the cases, the predicted locations of the delaminations matched what was observed in the tests. Finally, the interface elements created for this study were able to intrinsically take account of any changes in mode ratio. This enabled us to observe the considerable variation in mode ratio during the damage process of an individual element. This issue has not been studied in the current literature.

When there is more than one possible delamination site, the above approach has a significant advantage over conventional fracture mechanics methods, such as the virtual crack closure technique, since it is not necessary to assume where or at what rates the cracks will propagate. When there is a macroscopic singularity present in the model, such as a ply-drop, the interface approach has an advantage over stress based methods since it is not dependent on a characteristic length which is difficult to measure, and is less sensitive to mesh size as the yielding prevents acute stress gradients.

However, at present it is likely that the user will have to spend time defining the behaviour of the element with a computer code since elements of this type are not widely available in commercial finite element packages. Additional time might also be required for fine tuning the solver so that convergence is achieved.

# Chapter 9

# Conclusions

## 9.1 Main achievements

A structured strategy was conceived for investigating and developing methods for accurately predicting through-thickness failure in composite laminates with curvature and discontinuous plies.

A literature survey was undertaken to gain an overview of the established methods for predicting delamination failure in composite laminates. This knowledge was used as a platform for making improvements in the way delamination is predicted, with the aim of increasing the accuracy without increasing the complexity of the analysis.

Through-thickness failure in curved laminates without discontinuous plies was studied first of all. This was achieved by constructing a finite element model of curved specimens which had been designed and tested to measure the through-thickness strength of composites under combined tension and shear. By inserting the values of the maximum interlaminar stresses into a simple interactive failure criterion, the failure loads of the specimens were predicted. The correlation with the experimental results was far from satisfactory. It was hypothesised that this might have been due to the difference in stressed volume between the specimen under study and the specimens used to derive the two individual interlaminar strengths. Therefore, the method was modified by using Weibull theory to take account of

volumetric size effects. The resulting predictions matched the experimental failure loads reasonably well.

Attention was then turned towards the problem of delamination in laminates originating at discontinuous plies. In the first case, the laminate was assumed to have no curvature and not to be under any out-of-plane forces. An analytical solution was derived for calculating the strain energy release rate due to delamination from the discontinuous plies of a laminate under a combination of bending and axial forces. Thus delamination could be predicted without the need for time consuming finite element analysis. A parametric study using the closed form solution revealed that one of the most important parameters affecting the magnitude of the strain energy release rate was the axial strain at the ply-drop. Therefore, from the values of in-plane strain allowables which are commonly used in industry, it would be easy to work out the orientations and maximum number of plies that can be dropped together in a laminate.

The problem was then progressed by assuming the laminate was also under out-of-plane forces, which give rise to interlaminar shear stresses. Finite element analysis was carried out on straight specimens in three-point bending which had been designed and tested to look at the problem of delamination due to a combination of local stresses arising at discontinuous plies and an overall interlaminar shear stress distribution. The virtual crack closure technique was used to determine the strain energy release rates of different crack combinations. An established failure criterion based on the mode I and mode II strain energy release rates was not able to accurately predict the loads at which delamination occurred in the tests. Therefore, the method was improved by taking account of the matrix yielding which occurs prior to crack formation. This approach was relatively simple, yet the predictions were improved considerably.

Having separately tackled the problem of through-thickness failure in laminates with curvature but without discontinuous plies, and the problem of delamination in laminates with discontinuous plies but without curvature, specimens were analysed which had both these attributes. The same fracture mechanics approach that

accounted for yielding in the matrix was used to predict the failure loads of the specimens. There was reasonably good correlation with the experimental results. but the predictions tended to be unconservative.

The problem of delamination from discontinuous plies due to fatigue cannot be overlooked, and was therefore studied briefly. The static tests done on straight specimens in three-point bending were repeated in cyclic fatigue. Delaminations grew from the discontinuous plies and degraded the bending stiffness of the specimens. The rate of stiffness degradation was closely matched by a method combining the Paris equation and the cyclic strain energy release rate obtained from finite element analysis.

Finally, another approach was carried out to predict the static delamination loads of the specimens with discontinuous plies. It involved using specialised elements to model the resin rich layer between plies along which the delaminations were assumed to propagate. A Fortran code was written to define the behaviour of the elements. In the code, a yield criterion was used to predict the initiation of damage, and a strain energy release rate criterion was used to predict final failure. Therefore, the approach had a similar philosophy to the previous fracture mechanics approach which accounted for yielding, but it was not necessary to assume the locations and relative growth rates of the different delaminations. Thus it had an advantage over the previous approach for cases with multiple delaminations. However, there was no improvement in the accuracy of the predicted failure loads for the specimens with discontinuous plies.

Once more, the predictions for the straight specimens were always more conservative than the predictions for the curved specimens. The reason for this might be related to the fact that the curved specimens had higher fibre volume fractions than the straight specimens due to more resin bleed during the curing process. This would result in thinner resin rich layers between plies and perhaps lower fracture toughnesses.

In conclusion, a number of different approaches for predicting through-thickness failure have been developed. They have beer the failure loads of a

series of relatively simple composite laminates with curvature and/or discontinuous plies. Note that delamination due to free edge stresses or out-of-plane impacts was not covered, although cyclic fatigue loading was briefly studied. There was generally reasonably good correlation with experimental test results and the approaches were kept from becoming more complex than necessary. Thus, the main objective of the thesis has been achieved.

## 9.2 Recommendations

For situations where there are no stress singularities due to for instance, ply-drops, through-thickness failure should be predicted using a stress-based failure criterion, after accounting for volumetric size effects with Weibull theory. However, if the Weibull moduli are not available and a rough estimate is all that is required, engineering judgement should be used to approximate conservative values of the interlaminar strengths by comparing the volume of the test specimens used for obtaining the strengths to the volume of highly stressed material in the structure.

Delamination from discontinuous plies in relatively flat laminates under no significant through-thickness shear loading should be predicted from the strain energy release rate. This can be evaluated quite easily from the closed form solution derived in chapter 4, and compared to the appropriate value of fracture toughness for a reasonably good initial estimate of the failure load.

If there are significant overall interlaminar stress distributions, a fracture mechanics approach by itself does not seem to be adequate. However, when a mixed-mode strain energy release rate criterion is coupled with a stress-based yield criterion to estimate the initial crack size, reasonably good predictions can be attained. Alternatively, if time is more important than accuracy, the above mentioned closed form solution should be used along with a conservative value of the fracture energy, such as the pure mode I value, $G_{Ic}$. Failure due to overall stresses should then be checked as recommended in the first paragraph of this section.

In laminates where there are several ply-drops in close proximity to each other, failure should be predicted with the use of interface elements in a finite element model. This approach is more computer intensive than the previous approach, but is well suited to cases with multiple delaminations. Again, if the engineer is constrained by time and just requires a first order estimate, the procedures recommended in the latter part of the previous paragraph should be taken at each individual ply-drop location.

## 9.3 Future research

In this thesis we have concentrated on unidirectional laminates so that the effects of discontinuous plies and curvature could be clearly separated from the free edge stresses encountered in mixed lay-ups. Future work could involve studying delamination due to the interaction of all these features.

Furthermore, all of the specimens had relatively simple geometries and loading conditions. Before any of the prediction methods are accepted by industry, they must be successful in more practical situations. Thus, these approaches should be used to predict delamination failure in structural elements similar to the roots of helicopter rotor blades and the joints between spars, ribs and skins of composite wings.

The problem of predicting delamination in cyclic fatigue was studied briefly in this thesis but there is scope for much more work in this area. For example, the interface element could be developed to store the plastic work it undergoes during each loading cycle. Hence the damage zone or crack length could be predicted with respect to the number of cycles.

The accuracy of any prediction method relies on the accuracy of the material properties which it assumes. Further work must go into studying the sensitivities of the fracture toughness and the Weibull modulus to the fibre volume fraction. Once

these relationships have been more thoroughly established, it will be possible for future approaches to account for them.

Two types of post-yield behaviour were used to model the interface element in this thesis. It was not conclusive as to which type of response predicted delamination more accurately. It is possible that the true post-yield behaviour is somewhere in between perfectly plastic and linearly work softening, but more work is needed to verify this.

# References

1. Pipes, R. B. and Pagano, N. J., "Interlaminar Stresses in Composite Laminates under Uniform Axial Extension", Delamination in Advanced Composites, ed. G. M. Newaz, Technomic, 1991.

2. Wisnom, M. R., Petrossian, Z. J. and Jones, M. I., "Interlaminar Failure of Unidirectional Glass/Epoxy due to Combined Through Thickness Shear and Tension", Composites Part A, Vol. 27A, 1996, pp. 921 - 929.

3. Petrossian, Z., Wisnom, M. R. and Jones, M. I., "Prediction of Delamination Growth at Discontinuous Plies due to Cyclic Loading", 4th Int. Conf. on Deformation and Fracture of Composites, Manchester, March 1997, pp. 253 - 261.

4. Wisnom, M. R. and Petrossian, Z., "Through-Thickness Failure Prediction for Fibre Reinforced Composites", NAFEMS World Congress, Stuttgart, April 1997, Vol. I, pp. 148 - 159.

5. Petrossian, Z. and Wisnom, M. R., "Improved Fracture Mechanics Predictions for Delamination of Composites Accounting for Yield Zones", 11th Int. Conf. on Composite Materials, Gold Coast, July 1997, Vol. II, pp. 353 - 363.

6. Petrossian, Z. and Wisnom, M. R., "Parametric Study of Delamination in Composites with Discontinuous Plies using an Analytical Solution based on Fracture Mechanics", Composites Part A, Vol. 29A, 1998, pp. 403 - 414.

7. Petrossian, Z. and Wisnom, M. R., "Prediction of Delamination Initiation and Growth from Discontinuous Plies using Interface Elements", Composites Part A, Vol. 29A, 1998, pp. 503 - 515.

8. Chow, W. T. and Atluri, S. N., "Prediction of Post-Buckling Strength of Stiffened Laminated Composite Panels based on the Criterion of Mixed-Mode Stress Intensity Factors", Computational Mechanics, Vol. 18, 1996, pp. 215 - 224.

9. Naganarayana, B. P. and Atluri, S. N., "Strength Reduction and Delamination Growth in Thin and Thick Composite Plates under Compressive Loading", Computational Mechanics, Vol. 16, 1995, pp. 170 - 189.

10. Cui, G. Y. and Ruiz, C., "Through-Thickness Failure of Laminated Carbon/Epoxy Composites under Combined Stress", Composites Science and Technology, Vol. 53, 1995, pp. 253 - 258.

11. Broughton, W. R. and Sims, G. D., "An Overview of Through-Thickness Test Methods for Polymer Matrix Composites", NPL Report DMM(A)148, October 1994.

12. Vizzini, A. J. and Lee, S. W., "Damage Analysis of Composite Tapered Beams", Journal of the American Helicopter Society, Vol. 40, 1995, pp. 43 - 49.

13. Raghava, R., Caddell, R. M. and Yeh, G. S. Y., "The Macroscopic Yield Behaviour of Polymers", Journal of Materials Science, Vol. 8, 1973, pp. 225 - 232.

14. Raghava, R. S. and Caddell, R. M., "A Macroscopic Yield Criterion for Crystalline Polymers", Int. J. Mech. Sci., Vol. 15, 1973, pp. 967 - 974.

15. Hashin, Z., "Failure Criteria for Unidirectional Fiber Composites", Journal of Applied Mechanics, Vol. 47, 1980, pp. 329 - 334.

16. Shokrieh, M. M. and Lessard, L. B., "Effects of Material Nonlinearity on the Three-Dimensional Stress State of Pin-Loaded Composite Laminates", Journal of Composite Materials, Vol. 30, No. 7, 1996, pp. 839 - 861.

17. Altus, E. and Dorogoy, A., "A Three-Dimensional Study of Delamination". Engineering Fracture Mechanics, Vol. 33, No. 1, 1989, pp. 1 - 19.

18. Fish, J. C. and Lee, S. W., "Delamination of Tapered Composite Structures", Engineering Fracture Mechanics, Vol. 34, No. 1, 1989, pp. 43 - 54.

19. Tsai, S. W. and Wu, E. M., "A General Theory of Strength for Anisotropic Materials", Journal of Composite Materials, Vol. 5, 1971, pp. 58 - 80.

20. Whitney, J. M. and Nuismer, R. J., "Stress Fracture Criteria for Laminated Composites Containing Stress Concentrations", Journal of Composite Materials, Vol. 8, 1974, pp. 253 - 265.

21. Griffith, A. A., "The Phenomena of Rupture and Flow in Solids", Philosophical Transactions of the Royal Society of London, Series A, Vol. 221, 1920, pp. 163 - 198.

22. Irwin, G. R., "Onset of Fast Crack Propagation in High Strength Steel and Aluminium Alloys", Sagamore Research Conference Proceedings, Vol. 2, 1956, pp. 289 - 305.

23. Minguet, P. J. and O'Brien, T. K., "Analysis of Composite Skin / Stringer Bond Failure Using a Strain Energy Release Rate Approach", Proceedings of ICCM-10, Whistler, August 1995.

24. Irwin, G. R., "Fracture", Handbuch der Physik, Vol. 6, Springer-Verlag. 1958, p. 551.

25. Robinson, P. and Song, D. Q., "A New Mode III Delamination Test for Composites", Advanced Composite Letters, Vol. 1, No. 5, 1992, pp. 160 - 164.

26. Reeder, J. R., "An Evaluation of Mixed-Mode Delamination Failure Criteria". NASA TM 104210, 1992.

27. Hashemi, S., Kinloch, A. J. and Williams, J. G., "The Analysis of Interlaminar Fracture in Uniaxial Fibre-Polymer Composites", Proceedings of the Royal Society of London, A 427, 1990, pp. 173 - 199.

28. Chatterjee, S. N., "Analysis of Test Specimens for Interlaminar Mode II Fracture Toughness, Part 1. Elastic Laminates", Journal of Composite Materials, Vol. 25, 1991, pp. 470 - 493.

29. Kageyama, K. and Kimpara, I., "Delamination Failures in Polymer Composites", Materials Science and Engineering, A 143, 1991, pp. 167 - 174.

30. Robinson, P., Javidrad, F. and Hitchings, D., "Finite Element Modelling of Delamination Growth in the DCB and Edge Delaminated DCB Specimens", Composite Structures, Vol. 32, 1995, pp. 275 - 285.

31. Garg, A. C., "Delamination - A Damage Mode in Composite Structures", Engineering Fracture Mechanics, Vol. 29, No. 5, 1988, pp. 557 - 584.

32. Rhee, K. Y., "Characterization of Delamination Behaviour of Unidirectional Graphite / PEEK Laminates using Cracked Lap Shear (CLS) Specimens", Composite Structures, Vol. 29, 1994, pp. 379 - 382.

33. Kinloch, A. J., Wang, Y., Williams, J. G. and Yayla, P., "The Mixed-Mode Delamination of Fibre-Composite Materials", Int. Conf. on Deformation and Fracture of Composites, Manchester, March 1993.

34. Hwu, C., Kao, C. J. and Chang, L. E., "Delamination Fracture Criteria for Composite Laminates", Journal of Composite Materials, Vol. 29, No. 15, 1995, pp. 1962 - 1987.

35. Bradley, W. L., "Relationship of Matrix Toughness to Interlaminar Fracture Toughness", Application of Fracture Mechanics to Composite Materials, ed. K. Friedrich, Elsevier Science Publishers, 1989, pp. 159 - 187.

36. Hashemi, S., Kinloch, A. J. and Williams, G., "Mixed-Mode Fracture in Fiber-Polymer Composite Laminates", Composite Materials: Fatigue and Fracture, Vol. 3, ASTM STP 1110, ed. T. K. O'Brien, ASTM, Philadelphia, 1991, pp. 143 - 168.

37. Sen, J. K. and Fish, J. C., "Failure Prediction of Composite Laminates under Torsion", Key Engineering Materials, Vols. 121-122, 1996, pp. 285 - 306.

38. Nuismer, R. J. and Labor, J. D., "Applications of the Average Stress Failure Criterion: Part I - Tension", Journal of Composite Materials, Vol. 12, 1978, pp. 238 - 249.

39. Nuismer, R. J. and Labor, J. D., "Applications of the Average Stress Failure Criterion: Part II - Compression", Journal of Composite Materials, Vol. 13, 1979, pp. 49 - 60.

40. Morris, D. H. and Hahn, H. T., "Mixed-Mode Fracture of Graphite / Epoxy Composites: Fracture Strength", Journal of Composite Materials, Vol. 11, 1977, pp. 124 - 138.

41. Kim, R. Y. and Soni, S. R., "Experimental and Analytical Studies on the Onset of Delamination in Laminated Composites", Journal of Composite Materials, Vol. 18, 1984, pp. 70 - 80.

42. Zhou, S. G. and Sun, C. T., "Failure Analysis of Composite Laminates with Free Edge", Journal of Composite Technology and Research, JCTRER, Vol. 12, No. 2. 1990, pp. 91 - 97.

43. Rybicki, E. F., Schmueser, D. W. and Fox, J., "An Energy Release Rate Approach for Stable Crack Growth in the Free-Edge Delamination Problem", Journal of Composite Materials, Vol. 11, 1977, pp. 470 - 487.

44. Wang, A. S. D. and Crossman, F. W., "Initiation and Growth of Transverse Cracks and Edge Delamination in Composite Laminates. Part 1. An Energy Method", Journal of Composite Materials Supplement, Vol. 14, 1980, pp. 71 - 87.

45. Crossman, F. W., Warren, W. J., Wang, A. S. D. and Law, G. E., "Initiation and Growth of Transverse Cracks and Edge Delamination in Composite Laminates. Part 2. Experimental Correlation", Journal of Composite Materials Supplement, Vol. 14, 1980, pp. 88 - 108.

46. O'Brien, T. K., "Characterization of Delamination Onset and Growth in a Composite Laminate", Damage in Composite Materials, ASTM STP 775, ed. K. L. Reifsnider, ASTM, 1982, pp. 140 - 167.

47. O'Brien, T. K., "Mixed-Mode Strain-Energy-Release Rate Effects on Edge Delamination of Composites", Effects of Defects in Composite Materials, ASTM STP 836, ASTM, 1984, pp. 125 - 142.

48. Wang, A. S. D., "An Overview of the Delamination Problem in Structural Composites", Key Engineering Materials, Vol. 37, 1989, pp. 1 - 20.

49. Finn, S. R. and Springer, G. S., "Delamination in Composite Plates under Transverse Static or Impact Loads - A Model", Composite Structures, Vol. 23, 1993, pp. 177 - 190.

50. Finn, S. R., He, Y-F. and Springer, G. S., "Delamination in Composite Plates under Transverse Static Loads - Experimental Results", Journal of Reinforced Plastics and Composites, Vol. 11, 1992, pp. 1196 - 1238.

51. Takeda, N. and Ogihara, S., "Initiation and Growth of Delamination from the Tips of Transverse Cracks in CFRP Cross-Ply Laminates", Composite Science and Technology, Vol. 52, 1994, pp. 309 - 318.

52. Lammerant, L. and Verpoest, I., "The Interaction between Matrix Cracks and Delaminations during Quasi-Static Impact of Composite", Composite Science and Technology, Vol. 51, 1994, pp. 505 - 516.

53. Brewer, J. C. and Lagace, P. A., "Quadratic Stress Criterion for Initiation of Delamination", Journal of Composite Materials, Vol. 22, 1988, pp. 1141 - 1155.

54. Cui, W. C., Wisnom, M. R. and Jones, M., "A Comparison of Failure Criteria to Predict Delamination of Unidirectional Glass / Epoxy Specimens Waisted through the Thickness", Composites, Vol. 23, No. 3, 1992, pp. 158 - 166.

55. Cui, W. C., Wisnom, M. R. and Jones, M., "A Comparison of Fracture Criteria to Predict Delamination of Unidirectional Glass / Epoxy Specimens with Cut Central Plies", FRC 92, Newcastle, 1992, paper 25.

56. Davies, G. A. O. and Robinson, P., "Predicting Failure by Debonding / Delamination", AGARD 74th Structures and Materials Meeting, Debonding and Delamination of Composites, Patras, Greece, 1992.

57. Davies, G. A. O., Stevens, K. A., Robinson, P., Specht, S., Robson, J. and Andre, S., "Modelling Composite Structural Failure by Finite Elements", NAFEMS Conference, 1995.

58. Davies, G. A. O., Robinson, P., Robson, J. and Eady, D., "Shear Driven Delamination Propagation in Two Dimensions", Composites Part A, Vol. 28A, 1997, pp. 757 - 765.

59. ABAQUS, Hibbitt, Karlsson and Sorensen Inc., 1080 Main Street, Pawtucket, RI 02860, U.S.A.

60. Wisnom, M. R. and Jones, M. I., "Size Effects in Interlaminar Tensile and Shear Strength of Unidirectional Glass Fibre / Epoxy", Journal of Reinforced Plastics and Composites, Vol. 15, 1996, pp. 2 - 15.

61. Weibull, W., "A Statistical Distribution Function of Wide Applicability", Journal of Applied Mechanics, Vol. 18, 1951, pp. 293 - 297.

62. Bullock, R. E., "Strength Ratios of Composite Materials in Flexure and in Tension", Journal of Composite Materials, Vol. 8, 1974, pp. 200 - 206.

63. Hitchon, J. W. and Phillips, D. C., "The Effect of Specimen Size on the Strength of CFRP", Composites, Vol. 9, 1978, pp. 119 - 124.

64. Wisnom, M. R., "Relationship between Strength Variability and Size Effect in Unidirectional Carbon Fibre / Epoxy", Composites, Vol. 22, 1991, pp. 47 - 52.

65. O'Brien, T. K. and Salpekar, S. A., "Scale Effects on the Transverse Tensile Strength of Graphite Epoxy Composites", NASA TM107637, 1992.

66. Yamada, S. E. and Sun, C. T., "Analysis of Laminate Strength and Its Distribution", Journal of Composite Materials, Vol. 12, 1978, pp. 275 - 284.

67. Zweben, C., "Simple Design Oriented Composite Failure Criteria Incorporating Size Effects", Proceedings of ICCM10, Vancouver, August 1995, Vol. I, pp. 675 - 683.

68. Beaumont, P. W. R., "The Failure of Fibre Composites: an Overview", Journal of Strain Analysis, Vol. 24, No. 4, 1989, pp. 189 - 205.

69. Wisnom, M. R. and Jones, M. I., "Delamination of Unidirectional Glass Fibre-Epoxy with Cut Plies Loaded in Four Point Bending", Journal of Reinforced Plastics and Composites, Vol. 14, January, 1995, pp. 45 - 59.

70. Cui, W., Wisnom, M. R. and Jones, M. I., "An Experimental and Analytical Study of Delamination of Unidirectional Specimens with Cut Central Plies", Journal of Reinforced Plastics and Composites, Vol. 13, August, 1994, pp. 722 - 739.

71. Cui, W., Wisnom, M. R. and Jones, M. I., "Effect of Through Thickness Tensile and Compressive Stresses on Delamination Propagation Fracture Energy", Journal of Composites Technology & Research, JCTRER, Vol. 16, No. 4, October, 1994, pp. 329 - 335.

72. Wisnom, M. R., "Delamination in Tapered Unidirectional Glass Fibre-Epoxy under Static Tension Loading", 32nd Structures, Structural Dynamics and Materials Conference, Baltimore, Maryland, April 8-10, 1991, pp. 1162 - 1172.

73. Cui, W., Wisnom, M. R. and Jones, M. I., "New Model to Predict Static Strength of Tapered Laminates", Composites, Vol. 26, No. 2, 1995, pp. 141 - 146.

74. Wisnom, M. R., Jones, M. I. and Cui, W., "Failure of Tapered Composites under Static and Fatigue Loading", AIAA Journal, Vol. 33, No. 5, May, 1995, pp. 911 - 918.

75. Salpekar, S. A., Raju, I. S. and O'Brien, T. K., "Strain Energy Release Rate Analysis of Delamination in a Tapered Laminate Subjected to Tension Load", J. Composite Materials, Vol. 25, 1991, pp. 118 - 141.

76. Kairouz, K. C. and Heath, R. J., "Fracture of Ply Drop-Offs in Composite Structures", Proc. ECCM-7 Conf., London, U.K., May, 1996, pp. 79 - 85.

77. . Shi, Y. B. and Hull, D., "Fracture of Delaminated Unidirectional Composite Beams", Journal of Composite Materials, Vol. 26, No. 15, 1992, pp. 2172 - 2195.

78. Charalambides, P. G., Lund, J., Evans, A. G. and McMeeking, R. M., "A Test Specimen for Determining the Fracture Resistance of Bimaterial Interfaces", Journal of Applied Mechanics, Vol. 56, March, 1989, pp. 77 - 82.

79. O'Brien, T. K., "Analysis of Local Delaminations and Their Influence on Composite Laminate Behaviour", Delamination and Debonding of Materials, ASTM STP 876, W. S. Johnson, Ed., American Society for Testing and Materials, Philadelphia, 1985, pp. 282 - 297.

80. Cui, W., Wisnom, M. R. and Jones, M. I., "Effect of Step Spacing on Delamination of Tapered Laminates", Composites Science and Technology, Vol. 52, 1994, pp. 39 - 46.

81. Curry, J. M., Johnson, E. R. and Starnes, J. H., "Effect of Dropped Plies on the Strength of Graphite-Epoxy Laminates", Proc. of AIAA/ASME/ASCE/AHS 28th Structures, Structural Dynamics, and Materials Conf., AIAA, Washington, 1987, pp. 737 - 747 (AIAA Paper 87 - 0874).

82. Harbert, S. J. and Hogan, H. A., "An Analysis of Curvature and Layup Effects on Delamination in Notched Composite Beams", Journal of Reinforced Plastics and Composites, Vol. 11, 1992, pp. 443 - 457.

83. Amrutharaj, G. S., Lam, K. Y. and Cotterell, B., "Delaminations at the Free Edge of a Composite Laminate", Composites, 27B, 1996, pp. 475 - 483.

84. Wisnom, M. R. and Jones, M. I., "Delamination due to Interaction between Overall Interlaminar Shear and Stresses at Terminating Plies", Composite Structures, Vol. 31, 1995, pp. 39 - 47.

85. Wisnom, M. R., "Shear Fracture of Unidirectional Composites without Initial Cracks", Composites Science and Technology, Vol. 52, 1994, pp. 9 - 17.

86. Partridge, I., Cranfield University. Private communication.

87. Wisnom, M. R., "The Effect of Fibre Rotation in ±45° Tension Tests on Measured Shear Properties", Composites, Vol. 26, No. 1, 1995, pp. 25 - 32.

88. Wisnom, M. R. and Jones, M. I., "Delamination due to Interaction between Curvature Induced Interlaminar Tension and Stresses at Terminating Plies", Composite Structures, Vol. 32, 1995, pp. 615 - 620.

89. Bolotin, V. V., "Delaminations in Composite Structures: its Origin, Buckling, Growth and Stability", Composites Part B, Vol. 27B, 1996, pp. 129 - 145.

90. Lin, C. T. and Kao, P. W., "Fatigue Delamination Growth in Carbon Fibre-Reinforced Aluminium Laminates", Composites Part A, Vol. 27A, 1996, pp. 9 - 15.

91. Wisnom, M. R., Jones, M. I. and Cui, W., "Delamination in Composites with Terminating Internal Plies under Tension Fatigue Loading", Composite Materials: Fatigue and Fracture, Vol. 5, ASTM STP 1230, Ed. R. H. Martin, 1995, pp. 486 - 508.

92. Wisnom, M. R. and Jones, M. I., "Through Thickness Fatigue Failure of Fibre Reinforced Composites", Aeronautical Journal, in press.

93. Thomas, D. M. and Webber, J. P. H., "A Design Study into the Delamination Behaviour of Tapered Composites", Composite Structures, Vol. 27, No. 4, 1994, pp. 379 - 388.

94. Chai, H., "Micromechanics of Shear Deformations in Cracked Bonded Joints". Int. J. Fracture, Vol. 58, No. 3, 1992, pp. 223 - 239.

95. Schellekens, J. C. J., "Computational Strategies for Composite Structures". PhD Thesis, Delft University, The Netherlands, 1992.

96. Schellekens, J. C. J. and de Borst, R., "A Nonlinear Finite-Element Approach for the Analysis of Mode-I Free Edge Delamination in Composites", Int. J. of Sol. and Struc., Vol. 30, No. 9, 1993, pp. 1239 - 1253.

97. Schellekens, J. C. J. and de Borst, R., "On the Numerical Modelling of Edge Delamination in Composites", Key Engineering Materials, Vol. 120, 1996, pp. 131 - 160.

98. Corigliano, A., "Formulation, Identification and Use of Interface Models in the Numerical Analysis of Composite Delamination", Int. J. Solids Structures, Vol. 30, No. 20, 1993, pp.2779 - 2811.

99. Hellweg, H-B., "Nonlinear Failure Simulation of Thick Composite Structures", PhD Thesis, Imperial College of Science, Technology and Medicine, London, 1994.

100. Crisfield, M. A., Mi, Y., Davies, G. A. O. and Hellweg, H-B., "Finite Element Methods and the Progressive Failure-Modelling of Composites Structures", COMPLAS 5, 1997.

101. Cui, W. and Wisnom, M. R., "A Combined Stress-Based and Fracture-Mechanics-Based Model for Predicting Delamination in Composites". Composites, Vol. 24, No. 6, 1993, pp. 467 - 474.

102. Wisnom, M. R., "Modelling the Effect of Cracks on Interlaminar Shear Strength", Composites Part A, Vol. 27A, No. 1, 1996, pp. 17 - 24.

103. Yamada, Y., Yoshimura, N. and Sakurai, T., "Plastic Stress-Strain Matrix and its Application for the Solution of Elastic-Plastic Problems by the Finite Element Method", Int. J. Mech. Sci., Vol. 10, 1968, pp. 343 - 354.

104. Chakrabarty, J., "Theory of Plasticity", McGraw-Hill, 1987.

105. Partridge, I. K. , Jaussaud, J. A. M. and Corberand, P. E. L., "Toughness Transfer from Matrix to Composite under Static and Dynamic Loadings", 1st Int. Conf. on Deformation and Fracture of Composites, Manchester, U.K., March, 1991.

106. Singh, S. and Partridge, I. K., "Mixed-Mode Fracture in an Interleaved Carbon-Fibre / Epoxy Composite", Composites Science and Technology, Vol. 55, 1995, pp. 319 - 327.

107. Bradley, W. L. and Cohen, R. N., "Matrix Deformation and Fracture in Graphite-Reinforced Epoxies", Delamination and Debonding of Materials, ASTM STP 876, W. S. Johnson, Ed., American Society for Testing and Materials, Philadelphia, 1985, pp. 389 - 410.

# Appendix

The following is the Fortran code defining the interface element with a work softening response. It is designed to be executed by the ABAQUS finite element solver whenever information about a user element is required.

Note that PROPS(1) refers to the length of the element, and PROPS(2) refers to the angle in degrees between the global x direction and the local tangent to the interface. SVARS(1), SVARS(2) and SVARS(3) are the shear, through-thickness and axial stresses, respectively. SVARS(4), SVARS(5) and SVARS(6) are the mode I, mode II and normalised total values of plastic work, respectively. SVARS(7) is the value of the plastic modulus, and SVARS(8) is the value of $\tau_{VM}$. U(*) and DU(*,1) are the node displacements and increments in displacements, respectively, which are made available by ABAQUS. RHS(*,1) and AMATRX(*,*) are the forces at the nodes and the terms in the stiffness matrix, respectively. These values are required by ABAQUS at the end of every iteration. Refer to the ABAQUS user manual for further information.

```
      SUBROUTINE UEL(RHS,AMATRX,SVARS,ENERGY,NDOFEL,NRHS,NSVARS,
     1 PROPS,NPROPS,COORDS,MCRD,NNODE,U,DU,V,A,JTYPE,TIME,DTIME,
     2 KSTEP,KINC,JELEM,PARAMS,NDLOAD,JDLTYP,ADLMAG,PREDEF,NPREDF,
     3 LFLAGS,MLVARX,DDLMAG,MDLOAD,PNEWDT,JPROPS,NJPROP,PERIOD)
C
      INCLUDE 'ABA_PARAM.INC'
C
      DIMENSION RHS(MLVARX,*),AMATRX(NDOFEL,NDOFEL),PROPS(*),
     1          SVARS(*),ENERGY(8),COORDS(MCRD,NNODE),U(NDOFEL),
     2          DU(MLVARX,*),V(NDOFEL),A(NDOFEL),TIME(2),PARAMS(*),
     3          JDLTYP(MDLOAD,*),ADLMA                    1AG(MDLOAD,*),
     4          PREDEF(2,NPREDF,NNODE)                    ?S(*)
```

```
C
C************** MATERIAL PROPERTIES, STRAINS, ETC. **************
C
      XLENG=PROPS(1)
      WIDTH=1.0
      G1C=0.25
      G2C=1.08
      THICK=0.01
      AREA=WIDTH*XLENG
      RAT1=THICK/XLENG
      PR=0.38
      YMOD=4000.0
      SHMOD=YMOD/(2*(1+PR))
      YLD=70.0
      ANGLE=PROPS(2)*3.1415927/180.0
      U1=U(1)
      U2=U(2)
      U3=U(3)
      U4=U(4)
      DU1=DU(1,1)
      DU2=DU(2,1)
      DU3=DU(3,1)
      DU4=DU(4,1)
C
C     ROTATE DISPLACEMENTS TO LOCAL AXIS
C
      U(1)=U1*COS(ANGLE)+U2*SIN(ANGLE)
      U(2)=U2*COS(ANGLE)-U1*SIN(ANGLE)
      U(3)=U3*COS(ANGLE)+U4*SIN(ANGLE)
      U(4)=U4*COS(ANGLE)-U3*SIN(ANGLE)
      DU(1,1)=DU1*COS(ANGLE)+DU2*SIN(ANGLE)
      DU(2,1)=DU2*COS(ANGLE)-DU1*SIN(ANGLE)
      DU(3,1)=DU3*COS(ANGLE)+DU4*SIN(ANGLE)
      DU(4,1)=DU4*COS(ANGLE)-DU3*SIN(ANGLE)
C
      RU=U(3)-U(1)
      RV=U(4)-U(2)
      RX=0.0
      RDU=DU(3,1)-DU(1,1)
      RDV=DU(4,1)-DU(2,1)
      RDX=0.0
      SSTN=RU/THICK
      ZSTN=RV/THICK
      XSTN=RX/XLENG
      DSS=RDU/THICK
      DZS=RDV/THICK
      DXS=RDX/XLENG
      SHOLD=SVARS(1)
      ZOLD=SVARS(2)
      XOLD=SVARS(3)
      G1_OLD=SVARS(4)
      G2_OLD=SVARS(5)
      GN_OLD=SVARS(6)
      H_OLD=SVARS(7)
      VM_OLD=SVARS(8)
```

```
C
C      WE WILL ASSUME PLANE STRESS & ZERO AXIAL STRAIN
C      (ONCE ELEMENT IS YIELDING THE AXIAL STRAIN IS
C      NEGLIGIBLE COMPARED TO INTERLAMINAR STRAIN, ANYWAY)
C
C************ INCREMENTS WHERE STRESSES ARE EXACTLY ZERO ********
C*************** SUCH AS BEGINNING OF FIRST INCREMENT ***********
C
C      YOU NEED ENOUGH INCREMENTS IN YOUR LOADING STEP SUCH THAT
C      THE MOST HIGHLY STRESSED INTERFACE ELEMENT IN THE STRUCTURE
C      DOES NOT HAVE A VON MISES STRESS GREATER THAN ABOUT 20% OF
C      THE YIELD STRESS AT THE END OF THE FIRST INCREMENT.
C
C      ABOUT 50 INCREMENTS IS USUALLY ENOUGH
C
       IF (VM_OLD.EQ.0.AND.GN_OLD.LT.0.99) THEN
         rout=1.0
         AMATRX(1,1)=SHMOD*AREA/THICK
         AMATRX(1,2)=0.0
         AMATRX(2,1)=0.0
         AMATRX(2,2)=YMOD*AREA/((1-PR*PR)*THICK)
         RHS(1,1)=AMATRX(1,1)*RDU+AMATRX(1,2)*RDV
         RHS(2,1)=AMATRX(2,1)*RDU+AMATRX(2,2)*RDV
         ZSTRS=RHS(2,1)/AREA
         SHEAR=RHS(1,1)/AREA
         XSTRS=YMOD*(DXS+PR*DZS)/(1-PR*PR)
         VM=SQRT((XSTRS*XSTRS+ZSTRS*ZSTRS-XSTRS*ZSTRS+
     1                                        3*SHEAR*SHEAR)/3)
         G1=G1_OLD
         G2=G2_OLD
         GNORM=GN_OLD
         IF ((VM/YLD).LE.1.0) THEN
           H=YMOD*100.0*(1-VM/YLD)*(1-VM/YLD)
         ELSE
           H=-YMOD*100.0*(1-VM/YLD)*(1-VM/YLD)
         END IF
       END IF
C
C************** ALL OTHER INCREMENTS (WHEN G < Gc) *************
C
       IF (VM_OLD.NE.0.AND.GN_OLD.LT.0.99) THEN
C
C      FIRST CHECK FOR UNLOADING
C      IF (n_kl dSTRAIN_kl) < 0 THEN ELEMENT BEHAVES ELASTICALLY
C      (SEE P.79&83 OF "THEORY OF PLASTICITY", J.CHAKRABARTY, 1987)
C
         SX=XOLD-(XOLD+ZOLD)/3
         SY=-(XOLD+ZOLD)/3
         SZ=ZOLD-(XOLD+ZOLD)/3
         SS=SHOLD
         SBS=3*(SX*SX+SX*SZ+SZ*SZ+SS*SS)
         H=H_OLD
         ALPHA=2*(1+H/(3*SHMOD))/3
         TOP=SY*(1-2*PR)*(SS*DSS+SZ*DZS)-PR*ALPHA*SBS*DZS
         BOTTOM=(1-PR)*ALPHA*SBS-SY*SY*(1-2*PR)
         if (bottom.eq.0) then
           print*,'error error, bott
         end if
```

```
          DYS=TOP/BOTTOM
          FUNK=SX*DXS+SY*DYS+SZ*DZS+SS*DSS
          IF (FUNK.LT.0.0) THEN
            rout=2.0
            AMATRX(1,1)=SHMOD*AREA/THICK
            AMATRX(1,2)=0.0
            AMATRX(2,1)=0.0
            AMATRX(2,2)=YMOD*AREA/((1-PR*PR)*THICK)
            DRHS1=AMATRX(1,1)*RDU+AMATRX(1,2)*RDV
            DRHS2=AMATRX(2,1)*RDU+AMATRX(2,2)*RDV
            RHS(1,1)=SHOLD*AREA+DRHS1
            RHS(2,1)=ZOLD*AREA+DRHS2
            ZSTRS=RHS(2,1)/AREA
            SHEAR=RHS(1,1)/AREA
            DELX=YMOD*(DXS+PR*DZS)/(1-PR*PR)
            XSTRS=XOLD+DELX
            VM=SQRT((XSTRS*XSTRS+ZSTRS*ZSTRS-XSTRS*ZSTRS+
     1                                          3*SHEAR*SHEAR)/3)
            G1=G1_OLD
            G2=G2_OLD
            GNORM=GN_OLD
            H=YMOD*100.0*(1-VM/YLD)*(1-VM/YLD)
C
          ELSE
C
C       IF NOT UNLOADING ELEMENT BEHAVES PLASTICALLY
C
C       ESTIMATE TANGENT MATRIX AND INCREMENTS IN STRESSES BASED
C       ON VALUES OF STRESSES AND H AT END OF LAST INCREMENT
C
C       THE THEORY IS BASED ON THE PRANDTL-REUSS STRESS-STRAIN
C       RELATION FOR WORK HARDENING MATERIAL
C       (SEE P.84 OF "THEORY OF PLASTICITY", J.CHAKRABARTY, 1987)
C
            EM=(H/(9*SHMOD))+(SS*SS/SBS)
            EN=2*(1-PR)*(1+H/(3*SHMOD))/3-(1-2*PR)*SY*SY/SBS
            if (en.eq.0) then
              print*,'error error, en = 0 !'
            end if
            TM11=EN/2-(1-PR)*SS*SS/SBS
            TM12=-(SZ+PR*SX)*SS/SBS
            TM22=2*EM+(1+PR)*SX*SX/SBS
            DELSH=2*SHMOD*(TM11*DSS+TM12*DZS)/EN
            DELZ=2*SHMOD*(TM12*DSS+TM22*DZS)/EN
            C1=-(SX+PR*SZ)*SS/SBS
            C2=-(1+PR)*SX*SZ/SBS+2*PR*EM
            DELX=2*SHMOD*(C1*DSS+C2*DZS)/EN
C
C       MAKE SURE STRESS DOESN'T CROSS OVER TO OTHER SIDE OF AXIS
C       (THIS CAN HAPPEN WHEN THERE IS STRAIN SOFTENING AND THE
C       STRESS IS VERY LOW OR THERE IS A SUDDEN BIG STRAIN INCREMENT)
C
            IF (GN_OLD.GE.0.1.AND.ABS(SHOLD).LE.ABS(DELSH).AND.
     1                                  ABS(ZOLD).LE.ABS(DELZ)) THEN
              rout=3.0
              RHS(1,1)=0.0
              RHS(2,1)=0.0
              AMATRX(1,1)=0.0
```

```
            AMATRX(1,2)=0.0
            AMATRX(2,1)=0.0
            AMATRX(2,2)=0.0
            ZSTRS=0.0
            SHEAR=0.0
            XSTRS=0.0
            VM=0.0
            DZS=DZS*ABS(ZOLD)/ABS(DELZ)
            DSS=DSS*ABS(SHOLD)/ABS(DELSH)
            DEE_Z=-ZOLD/YMOD+PR*XOLD/YMOD
            DEE_SH=-SHOLD/SHMOD
            DEP_Z=DZS-DEE_Z
            DEP_SH=DSS-DEE_SH
            IF (ZSTRS.GT.0) DELG1=ZOLD*0.5*DEP_Z*THICK
            IF (ZSTRS.LE.0) DELG1=0.0
            DELG2=SHOLD*0.5*DEP_SH*THICK
            G1=G1_OLD+ABS(DELG1)
            G2=G2_OLD+ABS(DELG2)
            GNORM=G1/G1C+G2/G2C
          ELSE
            rout=4.0
C
C     ESTIMATES OF STRESSES AT END OF INCREMENT
C
          SHEAR=SHOLD+DELSH
          ZSTRS=ZOLD+DELZ
          XSTRS=XOLD+DELX
          VM=SQRT((XSTRS*XSTRS+ZSTRS*ZSTRS-XSTRS*ZSTRS+
     1                              3*SHEAR*SHEAR)/3)
C
C     CALCULATE THE INCREMENTS IN PLASTIC WORK PER UNIT
C     AREA, I.E, DELTA_G_1 AND DELTA_G_2.
C
C     WORK_plastic = SIGMA x DELTA_EPSILON_plastic x VOLUME
C
C     DELTA_EPSILON_plastic = DELTA_EPSILON - DELTA_EPSILON_elastic
C
C     IF ELEMENT IS UNDER THROUGH THICKNESS COMPRESSION THE
C     INCREMENT IN G1 IS ZERO (SEE SCHELLEKENS' THESIS, P.69)
C
          DEE_Z=DELZ/YMOD-PR*DELX/YMOD
          DEE_SH=DELSH/SHMOD
          DEP_Z=DZS-DEE_Z
          DEP_SH=DSS-DEE_SH
          IF (ZSTRS.GT.0) DELG1=(ZOLD+DELZ*0.5)*DEP_Z*THICK
          IF (ZSTRS.LE.0) DELG1=0.0
          DELG2=(SHOLD+DELSH*0.5)*DEP_SH*THICK
          G1=G1_OLD+ABS(DELG1)
          G2=G2_OLD+ABS(DELG2)
          GNORM=G1/G1C+G2/G2C
C
C     ESTIMATE OF H AT END OF INCREMENT
C
C     WORK SOFTENING WHEN GNORM > 0.1
C
          IF (GNORM.LT.0.1) THEN
            IF ((VM/YLD).LE.1.0) THEI
              H=YMOD*100.0*(1-VM/YLD)
```

```
            ELSE
              H=-YMOD*100.0*(1-VM/YLD)*(1-VM/YLD)
            END IF
          END IF
          IF (GNORM.GE.0.1.AND.GNORM.LT.0.99) THEN
            IF (DELG1.NE.0) H=-74.0-256.6*DELG1/(DELG1+DELG2)
            IF (DELG1.EQ.0) H=-74.0
          ELSE IF (GNORM.GE.0.99) THEN
            H=0.0
          END IF
C
C     FORCES AND TANGENT MODULUS AT END OF THIS INCREMENT
C     (CALCULATED USING VALUES OF STRESSES & H AT END OF INC.)
C
          RHS(1,1)=SHEAR*AREA
          RHS(2,1)=ZSTRS*AREA
          SX=XSTRS-(XSTRS+ZSTRS)/3
          SY=-(XSTRS+ZSTRS)/3
          SZ=ZSTRS-(XSTRS+ZSTRS)/3
          SS=SHEAR
          SBS=3*(SX*SX+SX*SZ+SZ*SZ+SS*SS)
          EM=(H/(9*SHMOD))+(SS*SS/SBS)
          EN=2*(1-PR)*(1+H/(3*SHMOD))/3-(1-2*PR)*SY*SY/SBS
          if (en.eq.0) then
            print*,'error error, en = 0 !'
          end if
          TM11=EN/2-(1-PR)*SS*SS/SBS
          TM12=-(SZ+PR*SX)*SS/SBS
          TM22=2*EM+(1+PR)*SX*SX/SBS
          AMATRX(1,1)=2*SHMOD*TM11*AREA/(EN*THICK)
          AMATRX(1,2)=2*SHMOD*TM12*AREA/(EN*THICK)
          AMATRX(2,1)=2*SHMOD*TM12*AREA/(EN*THICK)
          AMATRX(2,2)=2*SHMOD*TM22*AREA/(EN*THICK)
C
C     THE "END IF" DIRECTLY BELOW CORRESPONDS TO THE IF STATEMENT
C     WHICH CHECKS FOR "STRESS CROSS-OVER":
C
          END IF
        END IF
      END IF
C
C******************** BEHAVIOUR WHEN G > Gc ********************
C
      IF (GN_OLD.GE.0.99) THEN
        rout=5.0
        RHS(1,1)=0.0
        RHS(2,1)=0.0
        AMATRX(1,1)=0.0
        AMATRX(1,2)=0.0
        AMATRX(2,1)=0.0
        AMATRX(2,2)=0.0
        ZSTRS=0.0
        SHEAR=0.0
        XSTRS=0.0
        VM=0.0
        G1=G1_OLD
        G2=G2_OLD
        GNORM=GN_OLD
```

```
        H=0.0
      END IF
C
C******************** OUTPUT RESULTS ****************************
C
C     FIRST ROTATE A-MATRIX AND RHS BACK TO GLOBAL AXIS
C
      C=COS(ANGLE)
      S=SIN(ANGLE)
      RHS1=RHS(1,1)
      RHS2=RHS(2,1)
      RHS(1,1)=RHS1*C-RHS2*S
      RHS(2,1)=RHS2*C+RHS1*S
      RHS(3,1)=-RHS(1,1)
      RHS(4,1)=-RHS(2,1)
C
      AM11=AMATRX(1,1)
      AM12=AMATRX(1,2)
      AM21=AMATRX(2,1)
      AM22=AMATRX(2,2)
      AM13=-AM11
      AM14=-AM12
      AM23=-AM21
      AM24=-AM22
      AM31=-AM11
      AM32=-AM12
      AM33=AM11
      AM34=AM12
      AM41=-AM21
      AM42=-AM22
      AM43=AM21
      AM44=AM22
      AR11=AM11*C-AM12*S
      AR12=AM11*S+AM12*C
      AR13=AM13*C-AM14*S
      AR14=AM13*S+AM14*C
      AR21=AM21*C-AM22*S
      AR22=AM21*S+AM22*C
      AR23=AM23*C-AM24*S
      AR24=AM23*S+AM24*C
      AR31=AM31*C-AM32*S
      AR32=AM31*S+AM32*C
      AR33=AM33*C-AM34*S
      AR34=AM33*S+AM34*C
      AR41=AM41*C-AM42*S
      AR42=AM41*S+AM42*C
      AR43=AM43*C-AM44*S
      AR44=AM43*S+AM44*C
      AMATRX(1,1)=C*AR11-S*AR21
      AMATRX(1,2)=C*AR12-S*AR22
      AMATRX(1,3)=C*AR13-S*AR23
      AMATRX(1,4)=C*AR14-S*AR24
      AMATRX(2,1)=S*AR11+C*AR21
      AMATRX(2,2)=S*AR12+C*AR22
      AMATRX(2,3)=S*AR13+C*AR23
      AMATRX(2,4)=S*AR14+C*AR24
      AMATRX(3,1)=C*AR31-S*AR41
      AMATRX(3,2)=C*AR32-S*AR42
```

```
      AMATRX(3,3)=C*AR33-S*AR43
      AMATRX(3,4)=C*AR34-S*AR44
      AMATRX(4,1)=S*AR31+C*AR41
      AMATRX(4,2)=S*AR32+C*AR42
      AMATRX(4,3)=S*AR33+C*AR43
      AMATRX(4,4)=S*AR34+C*AR44
C
C     STRESSES, ETC. REMAIN IN LOCAL SYSTEM
C
      SVARS(1)=SHEAR
      SVARS(2)=ZSTRS
      SVARS(3)=XSTRS
      SVARS(4)=G1
      SVARS(5)=G2
      SVARS(6)=GNORM
      SVARS(7)=H
      SVARS(8)=VM
      svars(9)=rout
      RETURN
      END
```

The code for the interface element with a perfectly plastic post-yield response is very similar, except that the value of H is kept to zero throughout the damage process.